K. V. Rao R. H. Pletcher J. L. Steger W. R. Van Dalsem

A Three-Dimensional Dual Potential Procedure with Applications to Wind Tunnel Inlets and Interacting Boundary Layers

June 1987

Submitted to:
National Aeronautics and Space Administration
Ames Research Center
Moffett Field, California
Interchange No. NCA2-17

HTL-47, CFD-18
ISU-ERI-Ames-87296

final report

College of Engineering
Iowa State University

HTL-47, CFD-18
Project 1794
ISU-ERI-Ames-87296

K. V. Rao R. H. Pletcher J. L. Steger W. R. Van Dalsem

A Three-Dimensional Dual Potential Procedure with Applications to Wind Tunnel Inlets and Interacting Boundary Layers

Final Report

Funds for the support of this study have been allocated by the NASA-Ames Research Center, Moffett Field, California, under Interchange No. NCA2-17.

Heat Transfer Laboratory
Department of Mechanical Engineering
Computational Fluid Dynamics Center

engineering research institute
iowa state university

TABLE OF CONTENTS

LIST OF FIGURES

Page

Page

ABSTRACT

A dual potential decomposition of the velocity field into a scalar and a vector potential function is extended to three dimensions and used in the finite-difference simulation of steady three-dimensional inviscid rotational flow and viscous flow.

The finite-difference procedure has been used to simulate the flow through the 80- by 120-Foot Wind Tunnel at NASA Ames Research Center. Rotational flow produced by the stagnation pressure drop across vanes and screens which are located at the entrance of the inlet is modeled using actuator disk theory. Results are presented for two different inlet vane and screen configurations. The numerical predictions are in good agreement with experimental data.

The dual potential procedure has also been applied to calculate the viscous flow along two and three-dimensional troughs. Viscous effects are simulated by injecting vorticity which is computed from a boundary-layer algorithm. For attached flow over a three-dimensional trough, the present calculations are in good agreement with other numerical predictions. For separated flow, it is shown from a two-dimensional analysis that the boundary-layer approximation provides an accurate measure of the vorticity in regions close to the wall; whereas further away from the wall, caution has to be exercised in using the boundary-layer equations to supply vorticity to the dual potential formulation.

NOMENCLATURE

Note: All dimensional quantities are nondimensionalized by their free stream values or some reference quantity, as explained in §II.A. Boundary-layer variables are indicated with bars ($\bar{}$) to distinguish them from other variables.

Roman Symbols

$A^{\xi\xi}, A^{\xi\eta}, A^{\xi\zeta}$	metric quantities (2.40)
$A^{\eta\eta}, A^{\eta\zeta}, A^{\zeta\zeta}$	metric quantities (2.40)
$\vec{B}$	vector potential (2.10)
C	loss coefficent (3.10)
C_p	coefficient of pressure
c_p	specific heat at constant pressure (2.8)
c_v	specific heat at constant volume (2.8)
D	drag force (3.6)
$\vec{f}$	heat flux (2.6)
h	enthalpy
h	time step
H	total enthalpy (2.7)
J	Jacobian (2.36)
k	thermal conductivity
K	total loss coefficient (3.3)
K_s	screen loss coefficient (3.4)
$K_{s\infty}$	screen loss coefficient for onset flow (3.7)
K_v	vane loss coefficient (3.4)
L	left hand side operator
L	reference length
$\vec{n}$	unit vector in normal direction to surface
N	number of cycles (2.61)
p	pressure
p_0	total pressure
$\vec{q}$	velocity vector
R	right hand side operator
R	perfect gas constant
R_∞	free stream subtraction term (2.58)
Re	Reynolds number
s	entropy
T	temperature
u	x component of velocity

U	ξ direction contravariant velocity (2.37)
v	y component of velocity
V	η direction contravariant velocity (2.37)
w	z component of velocity
W	ς direction contravariant velocity (2.37)
x	streamwise coordinate direction
y	spanwise coordinate direction
z	normal coordinate direction

Greek Symbols

α	turning angle (3.8)
γ	ratio of specific heats (2.8)
δ	central difference operator (2.52)
$\bar{\delta}$	mid-point central difference operator (2.52)
δ^b	second order accurate backward difference operator (2.52)
δ^f	second order accurate forward difference operator (2.52)
δ_x	integral thickness for u-component of velocity (4.9)
δ_y	integral thickness for v-component of velocity (4.9)
δ^*	displacement thickness (4.10)
δ_{ij}	Kronecker delta function
Δ	forward difference operator (2.52)
ς	transformed coordinate (2.33)
η	transformed coordinate (2.33)
θ	turning angle (3.15)
ϑ	vector potential in x direction (2.10)
$\lambda, \lambda_1, \lambda_2$	relaxation parameters (2.61)
μ	viscosity
ξ	transformed coordinate (2.33)
ρ	density
$\hat{\rho}$	density scaled by Jacobian
$\vec{\tau}$	viscous stress tensor (2.5)
τ_{wx}	dimensionless wall shear stress in x-direction (4.9)
τ_{wy}	dimensionless wall shear stress in y-direction (4.9)
ϕ	scalar potential function (2.10)
χ	vector potential in y direction (2.10)
ψ	vector potential in z direction (2.10)
$\vec{\omega}$	vorticity vector (2.13)
$\vec{\Omega}$	contravariant vorticity vector (2.43)
$\omega_1, \omega_2, \omega_3$	vorticity components (2.13)

$\Omega_1, \Omega_2, \Omega_3$	contravariant vorticity components (2.43)
ω	overrelaxation parameter
ω	two-dimensional vorticity (4.16)

Subscripts

e	edge of boundary layer
j	x or ξ index
k	y or η index
l	z or ζ index
r	reference state
s	screen
so	screen only
t	test section
v	vane
w	wall value
x	derivative in x direction
y	derivative in y direction
z	derivative in z direction
1	location upstream of actuator disk
2	location downstream of actuator disk
∞	free stream conditions
ξ	derivative in ξ direction
ξ	ξ direction operator
η	derivative in η direction
η	η direction operator
ζ	derivative in ζ direction
ζ	ζ direction operator

Superscripts

n	iteration level
B	vector potential component
ϕ	scalar potential component

Other Symbols

∇	gradient operator
∇	backward difference operator (2.52)

I. INTRODUCTION

A. Overview of the Problem

The numerical solution of the partial differential equations governing the conservation of mass, momentum, and energy is an important tool with which to analyze and study fluid motion. Recent advances in computer speed and memory together with improved methodology have resulted in computational fluid dynamics (CFD) playing an increasingly important role in aerodynamic research and development. The governing equations of fluid dynamics are the Navier-Stokes equations and several algorithms have been developed to solve these equations for simple two and three-dimensional configurations. However, even with recent developments in computer speed and memory, one of the pacing problems of today is the efficient and accurate prediction of flow around complex three-dimensional geometries.

Several approaches are commonly employed in order to reduce the overall computational time and cost of obtaining numerical solutions of steady-state flow problems. One strategy is to solve a single set of simplified equations to approximate the entire flowfield. The most commonly used simplification for high Reynolds number flows is to solve the full potential equation, thereby assuming the flow to be inviscid and irrotational. However, even at high Reynolds number, many of the flows in nature possess substantial regions with rotation or vorticity. If one were to solve these problems with the potential equation, then the tedious task of setting up vortex-sheet discontinuities in the field and adjusting them to the surrounding flow has to be encountered. The alternative, which is the next step in the refinement of the approximation, is to solve the Euler equations which permit rotational flow everywhere. Finally, if one is interested in the viscous effects at solid boundaries, then

it is necessary to solve the complete Navier-Stokes equations or an appropriately reduced form of these equations which contains viscous terms.

Another strategy which is often employed is to divide the flow-field into separate zones and treat each zone with a simplified set of equations with matching performed in order to couple the separate solutions. The equation sets, and hence the solution algorithms, used in the different regions may be drastically different as, for example, in the commonly used viscous-inviscid interaction methods in which a boundary-layer algorithm is coupled with an inviscid flow solver.

After having selected a simplified or complete equation set, one is faced with several alternative procedures for solving them. For two-dimensional flows, it is as common to find solution algorithms written to solve for the primitive variables: velocity and pressure, as it is easy to find algorithms to solve for the derived variables: stream function and vorticity. In two dimensions, the advantage of the vorticity/stream-function approach is that continuity is automatically satisfied at the expense of solving a higher-order differential equation. Also, the same vorticity/stream-function approach results in fewer variables due to the elimination of the pressure from the governing equations. For the more general three-dimensional case, this approach in fact leads to more variables than the primitive variable case. However, the method may have advantages in certain applications.

The focus of this study is to develop a procedure for solving the equations of motion with a vorticity/stream-function type of method, and a review of previous work done in this area is given in the next section.

B. Literature Review

1. Vector potential methods

a. Incompressible flow Several efforts have been made to extend the advantages offered by the vorticity/stream-function approach in two dimensions to three-dimensional flow problems by expressing the velocity as the curl of a vector potential so that continuity is automatically satisfied (for incompressible flow) since the divergence of the curl of a vector is identically zero. A review of these efforts is provided by Richardson and Cornish (1977) and by Morino (1985). Because early efforts were, in part, hampered by lack of computational resources, not much work was reported for three-dimensional problems until Hirasaki and Hellums (1967) formulated the equations and the boundary conditions by expressing the velocity as the curl of a vector potential. Aziz and Hellums (1967) applied this formulation to study three-dimensional natural convection in enclosures. The formulation of Hirasaki and Hellums required the solution of a second-order partial differential equation in order to obtain the boundary conditions on the vector potential. Subsequently, they realized (Hirasaki and Hellums, 1970) that the addition of a scalar potential function to the velocity decomposition simplified the boundary conditions on the vector potential at the expense of introducing an additional variable and its corresponding equation. This velocity decomposition, in a slightly different form, has been termed the "dual potential" decomposition by Chaderjian and Steger (1983) and is used in this study to refer to the decomposition of the velocity into a scalar and a vector potential. The vector potential has been found to be particularly useful in the solution of three-dimensional natural convection in enclosures and several results have been reported (*cf.* Mallinson and de Vahl Davis, 1973; Ozoe et al., 1976; 1977; 1982). For these problems, it is not necessary to

include the scalar potential and hence computation time and storage requirements are reduced. Aziz and Hellums (1967) also showed that the vector potential formulation is computationally less expensive than a comparable primitive variable formulation for the problems they considered.

Aregbesola and Burley (1977) applied the dual potential formulation of Hirasaki and Hellums (1970) to study incompressible flow through ducts with internal recesses. Richardson and Cornish (1977) presented a rigorous analysis for the existence and uniqueness of the vector potential for general three-dimensional incompressible flow problems. In order to solve the full Navier-Stokes equations, the dual potential formulation requires the solution and storage of seven variables (four potential functions and three vorticity components) as opposed to four (three velocity components and pressure) in the primitive variable formulation. Hence, there have been several attempts to reduce the number of variables. Wong and Reizes (1984) replaced the scalar potential function with a specified inlet velocity vector, thereby reducing storage and computation time. However, their technique was restricted to flow through constant area ducts with incoming irrotational flow. More recently, Yang and Camarero (1986) reported solutions for three-dimensional duct flow problems using a dual potential type formulation. They used the Hirasaki and Hellums (1970) formulation for the boundary conditions on the vector potential. In particular, their formulation allowed for incoming rotational flow.

In recent years, with the availability of greater computer resources, some of the advantages of using the vector potential formulation has revived interest in this approach. One area of ambiguity in the boundary conditions for the vector potential has been the case of multiply connected regions such as annular passages. Richardson and Cornish (1977) derived the boundary conditions on the vector potential for

general three-dimensional geometries including multiply connected regions. Wong and Reizes (1986) derived slightly different boundary conditions for such regions and presented solutions for flow through cylindrical annular passages.

Related methods have been presented by Davis et al. (1986) who used the decomposition of the velocity field into two stream functions and applied it to compute the incompressible viscous flow over three-dimensional troughs and bumps. An excellent review of the techniques used for solving the Navier-Stokes equations in two dimensions with the vorticity/stream-function method is given by Roache (1972).

b. Compressible flow All of the studies mentioned up to now have dealt with incompressible steady flow problems. In inviscid compressible flow, the potential equation has been the workhorse of the aerospace industry, being widely used to compute the flow around complex configurations for a wide range of flow conditions. In the presence of shock waves, the flow is no longer irrotational, and entropy and vorticity corrections are needed to give better estimates of flow parameters. Emmons (1948) was the first to use the stream function to account for rotational effects and entropy changes following shocks in two-dimensional transonic flow. Hafez and Lovell (1981, 1983) also used the stream function to develop procedures to correct the potential solution. They studied a variety of methods to include rotational effects in the potential solution. Chaderjian and Steger (1983, 1985), working along similar lines, developed the dual potential formulation to simulate the steady transonic inviscid rotational flow around airfoils. Atkins and Hassan (1983) presented a different stream function formulation in which density and stream function were the dependent variables and the governing equations were solved in strong conservative law form. Recently, Hafez et al. (1987) developed a finite-element formulation in

which they used a dual potential type velocity decomposition scheme and applied it to calculate the transonic viscous flow through symmetric nozzles.

In three dimensions, Chaviaropoulos et al. (1986) developed a method for solving compressible inviscid rotational flow in the subsonic regime and used it to simulate flow through a rectangular elbow. Their formulation is similar to the one presented in this work for inviscid flow. Other alternate formulations using the Clebsch velocity decomposition have been presented by Grossman (1983) to compute inviscid supersonic conical flows, and by Chang and Adamczyk (1983) to compute inviscid subsonic rotational flow in turning channels. Sherif and Hafez (1983) presented a scheme for solving irrotational transonic flow using two stream functions and discussed possible extensions to rotational flow. Morino (1985) derived a set of equations for unsteady, compressible viscous flow. No implementation of the formulation has yet been reported.

2. Viscous flow

A number of methods have been used to simulate three-dimensional viscous flows. Some of the recent developments and trends in viscous flow simulation have been reviewed by Steger and Van Dalsem (1985) and by Shang (1985). Viscous flow can be simulated either by solving the complete Navier-Stokes equations (or a reduced form of these equations) or, alternatively, by coupling the boundary-layer equations to an efficient inviscid flow model (e.g., Lock, 1981; Melnik, 1981; McDonald and Briley, 1983). Various approximations to the Navier-Stokes equations such as the "parabolized" Navier-Stokes equations (PNS), the "partially parabolized" Navier-Stokes equations (PPNS), and the "thin-layer" Navier-Stokes equations (TLNS), are discussed by Anderson et al. (1984).

Efforts at solving the Navier-Stokes equations have been aimed at improving the robustness and speed of the various algorithms that are currently popular (Beam and Warming, 1976; Briley and McDonald, 1977; MacCormack, 1982). All of these algorithms solve the governing equations in primitive variables. Other algorithms have been developed for solving the incompressible Navier-Stokes equations (*cf.* Orszag and Israeli, 1974). A survey of the present state of the art in the numerical solution of the Navier-Stokes equations is given by Holst (1987), while details of the various methods are given by Anderson et al. (1984). It is sufficient to mention here that the increased availability of supercomputers has made it possible to perform three-dimensional calculations of complete aircraft configurations (Shang and Scherr, 1986; Flores et al., 1987). However, due to time and storage limitations, it is still necessary to find ways to improve the convergence rate of the Navier-Stokes algorithms. One approach has been the "fortified" Navier-Stokes concept introduced by Van Dalsem and Steger (1985). In this approach, the Navier-Stokes equations are solved in the entire flow field. In addition, the boundary-layer equations are solved near the wall on a fine grid to resolve the viscous gradients near the wall. This boundary-layer solution is then superimposed as a source function by interpolation to the main grid. This approach was found to improve the convergence rate of the Navier-Stokes algorithm by a factor of 20 for the cases considered (Van Dalsem and Steger, 1986b). Along similar lines, Goble and Fung (1987) developed a truncation error scheme in which a local solution was obtained on a fine grid and used to form an approximation to the truncation error. This approximation was then used as a forcing function in the global solver.

On the other hand, the search for alternative faster, but possibly not as general, methods has resulted in various zonal schemes. Here, efforts have been concentrated

on making the schemes more general by improving the approximations made in the various zones. One such approach to improve the accuracy of the inviscid flow approximation was proposed by Steger and Van Dalsem (1985) wherein viscous effects were accounted for by the injection of vorticity into an inviscid rotational solution. The vorticity was obtained from a suitable boundary-layer solution which interacted with the inviscid rotational flow through the pressure field. This approach was implemented in two dimensions to calculate the separated flow through a diffuser. A similar idea, referred to as the "pseudo Navier-Stokes approach", was proposed at about the same time by Whitfield (1985) with the difference that Steger and Van Dalsem used the vorticity/stream-function method to calculate the inviscid flow while Whitfield maintained the primitive variable formulation for both the boundary-layer and the outer flow equations. Halim and Hafez (1984) developed a slightly different scheme in which they used the stream function to calculate the inviscid flow and the "partially parabolized" Navier-Stokes equations to supply the vorticity instead of the boundary-layer equations.

One very useful approach for resolving viscous effects adjacent to solid surfaces and wakes is the viscous-inviscid interaction method. In this method, the viscous shear layer over the wall or the wake, and the inviscid flow external to the shear layer are solved separately, together with a matching process which allows for the interaction of the two flows. In the most common viscous-inviscid interaction schemes, the viscous layer is resolved by solving the boundary-layer equations, and the inviscid flow by solving the full-potential equation. The two solutions are matched by iterating for the displacement thickness. Some like Whitfield et al. (1981) have used the Euler equations to obtain the inviscid flow solution. In two dimensions, various methods have been proposed to improve the speed and accuracy of the viscous

and the inviscid sets of equations (*cf.* Lock, 1981; Melnik, 1981; McDonald and Briley, 1983). Most of these have concentrated on obtaining the quasi-simultaneous or simultaneous solution of the two sets of equations (Lee and Pletcher, 1986), to improve the convergence rate. Initially, viscous-inviscid interaction procedures used the direct method in which the pressure was calculated from the inviscid solution and specified as a forcing function for the boundary-layer equations. However, with the pressure specified, the boundary-layer equations become singular at separation (Goldstein, 1948; Brown and Stewartson, 1969) and the equations must be solved in the inverse mode (Catherall and Mangler, 1966; Klineberg and Steger 1974; Williams, 1975; Carter and Wornum, 1975; Kwon and Pletcher, 1979). In the inverse mode, the direct forcing function (pressure) is replaced by specifying an inverse forcing function such as displacement thickness or skin friction. In three dimensions, it is sufficient to only solve the streamwise momentum equation in the inverse mode to avoid the separation-point singularity, while the cross-flow momentum equation can be solved in the direct mode (Edwards and Carter, 1985; Van Dalsem and Steger, 1986a), though results have been obtained with both momentum equations solved in the inverse mode, that is, both components of skin friction or displacement thickness specified (Cousteix and Houdeville, 1981; Wigton and Yoshihara, 1983; Delery and Formery, 1983; Radwan and Lekoudis, 1984; Edwards and Carter, 1985).

There have been a number of schemes proposed for discretizing the steady three-dimensional boundary-layer equations (Der and Raetz, 1962; Dwyer, 1968; Krause et al., 1976; Kitchens et al., 1975). Most of these studies address the problems associated with the hyperbolic character of the equations in the x-z plane. In addition, for steady flows, another problem is the requirement of initial data along a y-z plane.

An excellent review of the contributions in this area can be found in the book by Anderson et al. (1984). Most of these problems are circumvented by Van Dalsem and Steger (1985) by using a time-dependent approach for obtaining solutions for steady flows. Even though only steady-state solutions are computed, with the use of the unsteady equations, relaxation algorithms can be devised which avoid some of the limitations of standard space-marching schemes. In addition to being able to compute unsteady flows, solving the unsteady equations may provide a simpler and alternative method for computing steady, separating and reattaching flows by enabling the use of flow-dependent difference operators. Additionally, with the use of a relaxation approach, simpler boundary conditions can be specified. This is especially true for boundary-layers in three dimensions, where, in a space marching scheme, all variables must be specified at inflow and at least one side boundary; whereas in a relaxation scheme, simpler zero-gradient boundary conditions can be used at the side boundary and an additional set of reduced equations for a plane of symmetry need not be solved.

C. Scope of the Present Study

This study is a combination of several of the solution strategies outlined above. The goal of providing a more complete solution to the flow-field is achieved by using a zonal method wherein a simplified equation set - namely the potential equation - is employed in regions of irrotational flow which is coupled with the Euler equations in regions of rotational flow. In the present method, a simplified set of equations is derived which have several useful features:

1) For the simplest kind of flow, without any modifications to the numerical algorithm, the method reduces to solving the full-potential equation. Hence, it is

possible to take advantage of the many fast algorithms that have been developed for this widely used equation.

2) For inviscid rotational flow, it is necessary to solve additional linear Poisson equations to account for rotational effects. Again, fast solution schemes can be used.

3) Finally, with the present approach, it is easy to extend the method to more general flow problems by solving additional equations for transport of vorticity or alternatively couple the inviscid set in a novel manner with a suitable boundary-layer algorithm, thereby retaining the advantages of the individual solution algorithms for the simplified sets of equations.

In this study, the dual potential formulation of Chaderjian and Steger (1985) is extended to three dimensions and used to simulate the steady, inviscid rotational flow through indraft wind tunnels. Screens and vanes which are located at the inlet entrance are modeled using actuator disk theory. The numerical results are compared with experimental data. A new interaction scheme is developed for coupling the inviscid dual potential formulation with the three-dimensional boundary layer procedure developed by Van Dalsem and Steger (1985). This interaction procedure is applied to compute the steady, attached flow over a three-dimensional trough. The procedure is also used to compute the steady, separated flow over a two-dimensional trough using a prescribed vorticity boundary condition.

The conservation laws for steady, three-dimensional flow are presented in Chapter II. Also in Chapter II, the dual potential velocity decomposition scheme is presented together with the numerical algorithms for solving the various equations. In Chapter III, the solution procedure for inviscid rotational flows is presented, along with results for flow through an indraft wind tunnel. This chapter also includes a

description of the actuator disk theory used to model the screens and vanes which are located at the entrance of the wind tunnel. Chapter IV presents the solution method for viscous flows along with results for flow over various trough configurations. This is followed by the conclusions in Chapter V. Appendix A includes an analysis of the geometric errors created by using nonuniform grids in transformed coordinates, while Appendix B gives the numerical algorithms for solving the incompressible two-dimensional dual potential and boundary-layer equations.

II. DUAL POTENTIAL FORMULATION

The objective of the portion of the study described in this chapter is to develop a formulation for simulating steady, three-dimensional rotational flow using the dual potential velocity decomposition. With the dual potential decomposition, the dependent variables are derived variables, vorticity and entropy. In order to derive the necessary equations for both inviscid and viscous rotational flow, the governing equations of mass, momentum and energy will first be presented in the more conventional primitive variables where velocity components and pressure are the dependent variables. Then the dual potential form of the equations will be derived. Finally, the numerical algorithms for the various equations will be given.

A. Conservation Laws

1. Governing equations in primitive variables

The governing conservation equations of mass, momentum and energy for the steady, three-dimensional flow of a perfect gas are derived in many textbooks in fluid mechanics. Using the form given by Anderson et al. (1984), the equations are presented below in Cartesian coordinates.

Continuity:

$$\nabla \cdot \rho \vec{q} = 0 \tag{2.1}$$

Momentum:

$$\rho(\vec{q} \cdot \nabla)\vec{q} = -\nabla p + \nabla \cdot \vec{\tau} \tag{2.2}$$

Energy:

$$\rho(\vec{q} \cdot \nabla)H = \nabla \cdot (\vec{\tau} \cdot \vec{q} - \vec{f}) \tag{2.3}$$

Equation of State:

$$p = \rho RT \tag{2.4}$$

In these equations, ρ is the fluid density, $\vec{q} = (u, v, w)^T$ is the velocity vector, p is the pressure, T is temperature, H is the total enthalpy, R is the perfect gas constant, ∇ is the gradient operator, and $\vec{\tau}$ is the viscous stress tensor given by

$$\tau_{ij} = \mu \left[\left(\frac{\partial u_i}{\partial x_j} + \frac{\partial u_j}{\partial x_i} \right) - \frac{2}{3} \delta_{ij} \frac{\partial u_k}{\partial x_k} \right] \tag{2.5}$$

where δ_{ij} is the Kronecker delta ($\delta_{ij} = 1$ if $i = j$ and $\delta_{ij} = 0$ if $i \neq j$), and μ is the viscosity. Using Fourier's law for heat transfer by conduction, the heat flux vector, $\vec{f}$ can be expressed as

$$\vec{f} = -k \nabla T \tag{2.6}$$

where k is thermal conductivity. The total enthalpy H is defined in terms of the enthalpy h as

$$H = h + \frac{1}{2} \vec{q} \cdot \vec{q} \tag{2.7}$$

Also, for a perfect gas, the following relationships hold:

$$h = c_p T; \quad \gamma = \frac{c_p}{c_v}; \quad c_p - c_v = R \tag{2.8}$$

where c_p is the specific heat at constant pressure, c_v is the specific heat at constant volume and γ is the ratio of specific heats.

2. Nondimensionalization

Variables in the governing equations are first nondimensionalized by their free stream values. The nondimensionalization is shown below with the nondimension-

alized variables indicated by the carets ($\hat{}$).

$$\begin{aligned} \hat{x} &= \frac{x}{L} & \hat{y} &= \frac{y}{L} & \hat{z} &= \frac{z}{L} \\ \hat{u} &= \frac{u}{u_\infty} & \hat{v} &= \frac{v}{u_\infty} & \hat{w} &= \frac{w}{u_\infty} & \hat{\mu} &= \frac{\mu}{\mu_\infty} \\ \hat{p} &= \frac{p - p_\infty}{\rho u_\infty^2} & \hat{\rho} &= \frac{\rho}{\rho_\infty} & \hat{H} &= \frac{H}{u_\infty^2} \end{aligned} \tag{2.9}$$

In these equations, L is a reference length. In all subsequent material, unless otherwise noted, variables will be assumed to be nondimensionalized although the carets will be omitted for ease of reading.

B. Velocity Decomposition Scheme

It is well known that any velocity field can be expressed as the gradient of a scalar potential and the curl of a vector potential (*cf.* Aris, 1962; Panton, 1984):

$$\vec{q} = \nabla\phi + \nabla \times \vec{B}; \quad \vec{B} = \begin{pmatrix} \vartheta \\ \chi \\ \psi \end{pmatrix} \tag{2.10}$$

so that

$$\vec{q} = \begin{pmatrix} u \\ v \\ w \end{pmatrix} = \begin{pmatrix} \phi_x + \psi_y - \chi_z \\ \phi_y + \vartheta_z - \psi_x \\ \phi_z + \chi_x - \vartheta_y \end{pmatrix} \tag{2.11}$$

With this decomposition, the divergence of $\vec{q}$ is given by

$$\nabla \cdot \vec{q} = \nabla^2\phi \tag{2.12}$$

where ∇^2 is the Laplacian operator $\nabla \cdot \nabla$, and the curl of the velocity (or vorticity) is given by

$$\vec{\omega} = \begin{pmatrix} w_y - v_z \\ u_z - w_x \\ v_x - u_y \end{pmatrix} = \begin{pmatrix} -(\vartheta_{yy} + \vartheta_{zz}) + (\chi_{xy} + \psi_{xz}) \\ -(\chi_{xx} + \chi_{zz}) + (\vartheta_{yx} + \psi_{yz}) \\ -(\psi_{xx} + \psi_{yy}) + (\vartheta_{xz} + \chi_{zy}) \end{pmatrix} \tag{2.13}$$

A rigorous mathematical analysis for the existence and uniqueness of the vector potential functions was presented by Hirasaki and Hellums (1967), and by Richardson and Cornish (1977), and proofs will not be given here. The three-dimensional

velocity field is represented by four potential functions, so there is one degree of redundancy in this decomposition. Hence, a constraint needs to be imposed on these functions in order to uniquely specify the velocity field. Following Chaderjian (1984), and Chaderjian and Steger (1985), the scalar potential is retained in order to obtain an equation for ϕ that is similar to the transonic full potential equation and a constraint is therefore imposed on the vector potential functions. A standard vector potential constraint that has often been employed (*cf.* Panton, 1984) is the condition that the vector potential be divergence free, that is,

$$\nabla \cdot \vec{B} = \vartheta_x + \chi_y + \psi_z = 0 \tag{2.14}$$

This consistency expression relates the vector potential functions to one another and removes the redundancy. It is used both to simplify the vorticity relations and to obtain an extra boundary condition (see also Hirasaki and Hellums, 1970; Wong and Reizes, 1984; Chaviaropoulos et al., 1986).

Subject to the consistency condition of equation (2.14), the vorticity assumes the compact symmetric form:

$$\begin{aligned} \nabla^2 \vartheta &= -\omega_1 \\ \nabla^2 \chi &= -\omega_2 \\ \nabla^2 \psi &= -\omega_3 \end{aligned} \tag{2.15}$$

or simply

$$\nabla^2 \vec{B} = -\vec{\omega} \tag{2.16}$$

An additional consistency equation relating the vorticities is obtained from the vector identity

$$\nabla \cdot \vec{\omega} = \nabla \cdot \nabla \times \vec{q} = 0 \tag{2.17}$$

or

$$(\omega_1)_x + (\omega_2)_y + (\omega_3)_z = 0 \tag{2.18}$$

which is also the Laplacian operating on equation (2.14).

1. Boundary conditions

On any boundary surface two linear combinations of the vector potential functions can be kept constant, and the vector potential consistency relation, equation (2.14), can be used to solve for a third linear combination. Tangency is then imposed on a body boundary surface from

$$\vec{n} \cdot \nabla\phi = -\vec{n} \cdot \nabla \times \vec{B} \tag{2.19}$$

In Cartesian coordinates, two components of $\vec{B}$ can be chosen to be constant on an x, y, or z boundary plane so that $\vec{n} \cdot \nabla \times \vec{B} = 0$ and $\nabla \cdot \vec{B} = 0$ supplies a Neumann boundary condition for the third component. For example, on a z = constant plane, ϑ and χ are taken as constants. Then ϑ_x and $\chi_y = 0$ and consistency gives $\psi_z = 0$, from which ψ can be determined on the z = constant surface. Likewise, χ_x and $\vartheta_y = 0$ and tangency, $w = 0$, is satisfied by setting $\phi_z = 0$.

2. The continuity equation

For the velocity decomposition given by equation (2.10), the continuity equation (2.1) takes the form

$$\begin{aligned}(\rho\phi_x)_x + (\rho\phi_y)_y + (\rho\phi_z)_z = \\ -[(\psi_y - \chi_z)\rho_x + (\vartheta_z - \psi_x)\rho_y + (\chi_x - \vartheta_y)\rho_z]\end{aligned} \tag{2.20}$$

It may be noted that this differs from the usual form of the transonic full-potential equation by the presence of the nonzero right-hand-side terms describing the rotational component of the velocity. For constant density, equation (2.20) reduces

simply to

$$\nabla^2\phi = 0 \tag{2.21}$$

It is useful to note that for a given vorticity distribution, the dual potential set of equations given by equations (2.16) and (2.20), subject to the appropriate boundary conditions, can be solved to obtain the complete velocity field. In particular, for the vector potential functions, these equations are simple linear Poisson equations, which are weakly coupled and hence can be individually solved efficiently using existing well developed methods. The dual potential set of equations outlined above are obtained from the continuity equation and from mathematical simplifications developed from the velocity decomposition. For irrotational inviscid flow, vorticity is zero and only the full potential equation needs to be solved, as the momentum equations are, in effect, satisfied. For rotational flow, however, the momentum equations which prescribe the vorticity need to be considered in order to obtain a complete description of the flowfield. These equations are developed in the next section for both inviscid and viscous flow.

C. The Momentum Equations

1. Momentum equations for inviscid flow

Inviscid flow is governed by the Euler equations which are obtained from the governing equations (2.1) - (2.8) by neglecting viscous and heat conduction terms. After omitting the viscous terms, the momentum equation (2.2) can be rewritten as

$$\rho(\vec{q}\cdot\nabla)\vec{q} = -\nabla p \tag{2.22}$$

Making use of the identity

$$(\vec{q}\cdot\nabla)\vec{q} = \nabla\left(\frac{q^2}{2}\right) - \vec{q}\times\omega \tag{2.23}$$

equation (2.22) can be rewritten as

$$\nabla\left(\frac{q^2}{2}\right) - \vec{q}\times\vec{\omega} = -\frac{\nabla p}{\rho} \tag{2.24}$$

Crocco's equation is obtained from the momentum equation by replacing the pressure gradient with an entropy gradient by using Gibb's equation which is obtained from the First and Second Laws of Thermodynamics and can be written as

$$T\nabla s = \nabla h - \frac{\nabla p}{\rho} \tag{2.25}$$

Crocco's equation for a steady, adiabatic flow ($h + \frac{1}{2}q^2 =$ constant) can then be written as

$$\vec{q}\times\vec{\omega} = -T\nabla s \tag{2.26}$$

An equation for the convection of entropy is formed by taking the dot product of the velocity vector with Crocco' equation:

$$\vec{q}\cdot\nabla s = 0 \tag{2.27}$$

Note that equation (2.27) is formed from a linear combination of the Crocco equations, and thus replaces one of the three equations given by equation (2.26).

Also for a steady inviscid adiabatic flow of a perfect gas, Crocco's relations, together with the perfect gas relation, can be used to derive the compressible Bernoulli equation (*cf.* Anderson et al., 1984):

$$\frac{\rho}{\rho_r} = \left[1 - \frac{1}{2}\left(\frac{q^2}{h_r}\right)\right]^{\frac{1}{\gamma-1}} e^{-(s-s_r)/R} \tag{2.28}$$

where the subscript r refers to a reference state.

These equations are modified for incompressible flow. For incompressible flow, density is taken to be constant and Bernoulli's equation is no longer used. In addition, the total pressure, $p_0 = p + \frac{1}{2}\rho q^2$, is used in place of entropy, and Lamb's equation replaces Crocco's equation. Making use of equations (2.24) - (2.26), the momentum equation for inviscid incompressible flow is written as Lamb's equation:

$$\vec{q} \times \vec{\omega} = \frac{\nabla p_0}{\rho} \tag{2.29}$$

and the entropy convection equation is replaced with a total pressure convection equation:

$$\vec{q} \cdot \nabla p_0 = 0 \tag{2.30}$$

Note again that the total pressure convection equation was formed by taking the dot product of the velocity vector with Lamb's equation and therefore replaces one of the three equations given by Lamb's equation.

Boundary conditions for the vorticity and entropy/total pressure are dependent on the geometry and flow conditions and will be given in the Chapter III, where results will be presented for a particular application of the procedure developed here.

2. Momentum equations for viscous flow

For viscous flow, the more complete momentum equations need to be solved. Assuming constant viscosity and density, equation (2.2) can be rewritten as

$$\rho(\vec{q} \cdot \nabla)\vec{q} = -\nabla p + \frac{1}{Re}\nabla^2 \vec{q} \tag{2.31}$$

where Re is the reference Reynolds number defined as $Re = \rho_\infty u_\infty L/\mu_\infty$. Taking the curl of equation (2.31) and simplifying gives

$$\rho(\vec{q}\cdot\nabla)\vec{\omega} = (\vec{\omega}\cdot\nabla)\vec{q} + \frac{1}{Re}\nabla^2\vec{\omega} \tag{2.32}$$

The momentum equation in this form, together with the dual potential equations can be solved to obtain the complete flowfield. However, in most cases, it is known that viscous effects are confined to a thin layer adjacent to the wall and most of the outer flow is inviscid. This is the basis for boundary-layer theory. The effect of the boundary-layer on the outer inviscid flow is usually accounted for through the use of a displacement effect (Lighthill, 1958). With the present formulation, it is possible to develop an alternate representation for the influence of viscous effects on the inviscid flow - that is, by obtaining the vorticity in the viscous region from the boundary-layer equations instead of solving the vorticity transport equations given by equation (2.32). That is, it may be possible to take advantage of the speed and efficiency of boundary-layer algorithms to calculate vorticity. With the vorticity specified, the dual potential set of equations could be solved to obtain the complete flow field. This concept is not new and has been proposed and implemented in two dimensions by Steger and Van Dalsem (1985). Various schemes for using the boundary-layer equations to supply the vorticity to the dual potential equations will be described in Chapter IV.

D. Generalized Curvilinear Coordinates

In order to simplify the treatment of arbitrary body boundaries in the numerical simulation, body-fitted curvilinear coordinates are employed, and the flow domain

is mapped to a uniformly spaced rectangular coordinate region. The general coordinate transformation is defined by

$$\xi = \xi(x,y,z), \quad \eta = \eta(x,y,z), \quad \varsigma = \varsigma(x,y,z) \tag{2.33}$$

In terms of the independent variables ξ, η, ς, the Cartesian velocity components can be evaluated from the potential functions using the chain rule of partial differentiation on equation (2.11) as

$$\begin{aligned}
u &= (\xi_x\phi_\xi + \eta_x\phi_\eta + \varsigma_x\phi_\varsigma) + (\xi_y\psi_\xi + \eta_y\psi_\eta + \varsigma_y\psi_\varsigma) \\
&\quad - (\xi_z\chi_\xi + \eta_z\chi_\eta + \varsigma_z\chi_\varsigma) \\
v &= (\xi_y\phi_\xi + \eta_y\phi_\eta + \varsigma_y\phi_\varsigma) + (\xi_z\vartheta_\xi + \eta_z\vartheta_\eta + \eta_z\vartheta_\varsigma) \\
&\quad - (\xi_x\psi_\xi + \eta_x\psi_\eta + \varsigma_x\psi_\varsigma) \\
w &= (\xi_z\phi_\xi + \eta_z\phi_\eta + \varsigma_z\phi_\varsigma) + (\xi_x\chi_\xi + \eta_x\chi_\eta + \varsigma_x\chi_\varsigma) \\
&\quad - (\xi_y\vartheta_\xi + \eta_y\vartheta_\eta - \varsigma_y\vartheta_\varsigma)
\end{aligned} \tag{2.34}$$

The metric quantities used in the above transformations are defined as

$$\begin{aligned}
\xi_x &= J(y_\eta z_\varsigma - y_\varsigma z_\eta), \quad \eta_x = J(y_\varsigma z_\xi - y_\xi z_\varsigma) \\
\xi_y &= J(x_\varsigma z_\eta - x_\eta z_\varsigma), \quad \eta_y = J(x_\xi z_\varsigma - x_\varsigma z_\xi) \\
\xi_z &= J(x_\eta y_\varsigma - x_\varsigma y_\eta), \quad \eta_z = J(x_\varsigma y_\xi - x_\xi y_\varsigma) \\
\varsigma_x &= J(y_\xi z_\eta - y_\eta z_\xi), \quad \varsigma_y = J(x_\eta z_\xi - x_\xi z_\eta) \\
\varsigma_z &= J(x_\xi y_\eta - x_\eta y_\xi)
\end{aligned} \tag{2.35}$$

where J is the Jacobian of the transformation given by

$$J = \xi_x(\eta_y\varsigma_z - \eta_z\varsigma_y) + \eta_x(\xi_z\varsigma_y - \xi_y\varsigma_z) + \varsigma_x(\xi_y\eta_z - \xi_z\eta_y) \tag{2.36}$$

Unscaled contravariant velocity components of the velocity vector $\vec{q}$ can be defined as

$$\begin{aligned}
U &= \xi_x u + \xi_y v + \xi_z w \\
V &= \eta_x u + \eta_y v + \eta_z w \\
W &= \varsigma_x u + \varsigma_y v + \varsigma_z w
\end{aligned} \tag{2.37}$$

The contravariant velocity components are conveniently split between the scalar potential contribution and the vector potential contribution as

$$\begin{aligned} U &= U^{\phi} + U^{B} \\ V &= V^{\phi} + V^{B} \\ W &= W^{\phi} + W^{B} \end{aligned} \tag{2.38}$$

where

$$\begin{aligned} U^{\phi} &= A^{\xi\xi}\phi_{\xi} + A^{\xi\eta}\phi_{\eta} + A^{\xi\zeta}\phi_{\zeta} \\ V^{\phi} &= A^{\xi\eta}\phi_{\xi} + A^{\eta\eta}\phi_{\eta} + A^{\eta\zeta}\phi_{\zeta} \\ W^{\phi} &= A^{\xi\zeta}\phi_{\xi} + A^{\eta\zeta}\phi_{\eta} + A^{\zeta\zeta}\phi_{\zeta} \\ U^{B} &= (\nabla\xi \times \nabla\eta)\cdot\vec{B}_{\eta} + (\nabla\xi \times \nabla\zeta)\cdot\vec{B}_{\zeta} \\ V^{B} &= (\nabla\eta \times \nabla\xi)\cdot\vec{B}_{\xi} + (\nabla\eta \times \nabla\zeta)\cdot\vec{B}_{\zeta} \\ W^{B} &= (\nabla\zeta \times \nabla\xi)\cdot\vec{B}_{\xi} + (\nabla\zeta \times \nabla\eta)\cdot\vec{B}_{\eta} \end{aligned} \tag{2.39}$$

and

$$\begin{aligned} A^{\xi\xi} &= \nabla\xi\cdot\nabla\xi = \xi_x^2 + \xi_y^2 + \xi_z^2 \\ A^{\eta\eta} &= \nabla\eta\cdot\nabla\eta = \eta_x^2 + \eta_y^2 + \eta_z^2 \\ A^{\zeta\zeta} &= \nabla\zeta\cdot\nabla\zeta = \zeta_x^2 + \zeta_y^2 + \zeta_z^2 \\ A^{\xi\eta} &= \nabla\xi\cdot\nabla\eta = \xi_x\eta_x + \xi_y\eta_y + \xi_z\eta_z \\ A^{\xi\zeta} &= \nabla\xi\cdot\nabla\zeta = \xi_x\zeta_x + \xi_y\zeta_y + \xi_z\zeta_z \\ A^{\eta\zeta} &= \nabla\eta\cdot\nabla\zeta = \eta_x\zeta_x + \eta_y\zeta_y + \eta_z\zeta_z \end{aligned} \tag{2.40}$$

It can also be shown that the operator $\vec{q}\cdot\nabla$ applied to any variable f can be expressed in the computational domain as

$$\begin{aligned} (\vec{q}\cdot\nabla)f &= uf_x + vf_y + wf_z \\ &= Uf_{\xi} + Vf_{\eta} + Wf_{\zeta} \end{aligned} \tag{2.41}$$

Similarly, the operator $\vec{\omega}\cdot\nabla$ which appears in the vorticity transport equation can

be transformed as

$$\begin{aligned}(\vec{\omega}\cdot\nabla)f &= \omega_1 f_x + \omega_2 f_y + \omega_3 f_z \\ &= \Omega_1 f_\xi + \Omega_2 f_\eta + \Omega_3 f_\zeta \\ &= (\vec{\Omega}\cdot\nabla)f\end{aligned} \tag{2.42}$$

where $\vec{\Omega}$ is the unscaled contravariant vorticity vector defined as

$$\vec{\Omega} = \begin{pmatrix}\Omega_1\\ \Omega_2\\ \Omega_3\end{pmatrix} = \begin{pmatrix}\xi_x\omega_1 + \xi_y\omega_2 + \xi_z\omega_3\\ \eta_x\omega_1 + \eta_y\omega_2 + \eta_z\omega_3\\ \zeta_x\omega_1 + \zeta_y\omega_2 + \zeta_z\omega_3\end{pmatrix} \tag{2.43}$$

1. Governing equations in transformed coordinates

The continuity equation can now be written in transformed coordinates as

$$\begin{aligned}&\left[\frac{\rho(A^{\xi\xi}\phi_\xi + A^{\xi\eta}\phi_\eta + A^{\xi\zeta}\phi_\zeta)}{J}\right]_\xi + \\ &\left[\frac{\rho(A^{\xi\eta}\phi_\xi + A^{\eta\eta}\phi_\eta + A^{\eta\zeta}\phi_\zeta)}{J}\right]_\eta + \\ &\left[\frac{\rho(A^{\xi\zeta}\phi_\xi + A^{\eta\zeta}\phi_\eta + A^{\zeta\zeta}\phi_\zeta)}{J}\right]_\zeta = \\ -&\left[\left(\frac{U^B}{J}\right)\rho_\xi + \left(\frac{V^B}{J}\right)\rho_\eta + \left(\frac{W^B}{J}\right)\rho_\zeta\right]\end{aligned} \tag{2.44}$$

The Poisson equations for the vector potential functions can be transformed similarly employing the same metric groupings and can be written in a compact vector form as

$$\begin{aligned}&\left(\frac{A^{\xi\xi}\vec{B}_\xi + A^{\xi\eta}\vec{B}_\eta + A^{\xi\zeta}\vec{B}_\zeta}{J}\right)_\xi + \\ &\left(\frac{A^{\xi\eta}\vec{B}_\xi + A^{\eta\eta}\vec{B}_\eta + A^{\eta\zeta}\vec{B}_\zeta}{J}\right)_\eta + \\ &\left(\frac{A^{\xi\zeta}\vec{B}_\xi + A^{\eta\zeta}\vec{B}_\eta + A^{\zeta\zeta}\vec{B}_\zeta}{J}\right)_\zeta = -\frac{\vec{\omega}}{J}\end{aligned} \tag{2.45}$$

In the same transformed coordinates the Crocco relations are given as

$$\begin{aligned} v\omega_3 - w\omega_2 &= -T(\xi_x s_\xi + \eta_x s_\eta + \zeta_x s_\zeta) \\ w\omega_1 - u\omega_3 &= -T(\xi_y s_\xi + \eta_y s_\eta + \zeta_y s_\zeta) \\ u\omega_2 - v\omega_1 &= -T(\xi_z s_\xi + \eta_z s_\eta + \zeta_z s_\zeta) \end{aligned} \tag{2.46}$$

while the vorticity transport equation (2.32) is written as

$$\rho(U\vec{\omega}_\xi + V\vec{\omega}_\eta + W\vec{\omega}_\zeta) = \frac{J}{Re}\left[\left(\frac{A^{\xi\xi}\vec{\omega}_\xi + A^{\xi\eta}\vec{\omega}_\eta + A^{\xi\zeta}\vec{\omega}_\zeta}{J}\right)_\xi + \left(\frac{A^{\xi\eta}\vec{\omega}_\xi + A^{\eta\eta}\vec{\omega}_\eta + A^{\eta\zeta}\vec{\omega}_\zeta}{J}\right)_\eta + \left(\frac{A^{\xi\zeta}\vec{\omega}_\xi + A^{\eta\zeta}\vec{\omega}_\eta + A^{\zeta\zeta}\vec{\omega}_\zeta}{J}\right)_\zeta\right] + (\vec{\Omega}\cdot\nabla)\vec{q} \tag{2.47}$$

and the entropy convection equation is given as

$$Us_\xi + Vs_\eta + Ws_\zeta = 0 \tag{2.48}$$

The consistency equation for the vector potential functions takes the form

$$\nabla\cdot\vec{B} = \nabla\xi\cdot\vec{B}_\xi + \nabla\eta\cdot\vec{B}_\eta + \nabla\zeta\cdot\vec{B}_\zeta = 0 \tag{2.49}$$

or simply

$$\begin{aligned} &(\xi_x\vartheta_\xi + \eta_x\vartheta_\eta + \zeta_x\vartheta_\zeta) + \\ &(\xi_y\chi_\xi + \eta_y\chi_\eta + \zeta_y\chi_\zeta) + \\ &(\xi_z\psi_\xi + \eta_z\psi_\eta + \zeta_z\psi_\zeta) = 0 \end{aligned} \tag{2.50}$$

Similarly, the vorticity consistency equation (2.18) can be expressed as

$$\begin{aligned} &\left[\xi_x(\omega_1)_\xi + \eta_x(\omega_1)_\eta + \zeta_x(\omega_1)_\zeta\right] + \\ &\left[\xi_y(\omega_2)_\xi + \eta_y(\omega_2)_\eta + \zeta_y(\omega_2)_\zeta\right] + \\ &\left[\xi_z(\omega_3)_\xi + \eta_z(\omega_3)_\eta + \zeta_z(\omega_3)_\zeta\right] = 0 \end{aligned} \tag{2.51}$$

E. Numerical Algorithms

The dual potential formulation outlined in the previous sections has several advantages. In an iterative solution scheme the governing equations (2.44) - (2.51)

are weakly coupled and hence can be solved separately. Because of the uncoupling, efficient solution schemes can be used for solving each individual equation. The actual iterative solution strategy for inviscid and viscous flow will be presented in Chapters III and IV. The numerical algorithms for the individual equations are described below.

The Poisson equations and the continuity (full potential) equations are conventionally differenced (i.e., central) and are solved with ADI-like procedures that use a sequence of relaxation parameters. The convection equations are differenced using upwind differencing in x or ξ and central differencing in the other directions. An implicit 2-factor approximate factorization (AF) method is being used as the relaxation scheme. Tangency and boundary consistency relations are enforced using one-sided differencing in the direction normal to the boundary surface and central differencing in the other two directions on the boundary surface. An ADI procedure is also used to relax the consistency and tangency boundary values. The following notation is used in describing the numerical algorithms. In the uniform computational domain, $\Delta\xi = \Delta\eta = \Delta\zeta = 1$. The indices j,k,l refer to grid points in the ξ-, η-, and ζ-directions, respectively. Generally a subscript is not shown unless it varies; for example, $u_{k+1} = u_{j,k+1,l}$. The difference operators are defined in terms of the shift operator $E_\xi^{\pm 1} u_j = u_{j\pm 1}$ as

$$\begin{aligned} \nabla_\xi &= (1 - E_\xi^{-1})/(\Delta\xi) \\ \Delta_\xi &= (E_\xi^{+1} - 1)/(\Delta\xi) \\ \delta_\xi &= (E_\xi^{+1} - E_\xi^{-1})/(2\Delta\xi) \\ \bar{\delta}_\xi &= (E_\xi^{+\frac{1}{2}} - E_\xi^{-\frac{1}{2}})/(\Delta\xi) \end{aligned} \tag{2.52}$$

Second-order accurate one-sided difference operators are defined as

$$\delta_\xi^b = \nabla_\xi \left(\frac{3 - E_\xi^{-1}}{2} \right)$$
$$\delta_\xi^f = \Delta_\xi \left(\frac{3 - E_\xi^{+1}}{2} \right) \tag{2.53}$$

1. ADI algorithm for the continuity and Poisson equations

The continuity equation for ϕ, equation (2.44), is updated using an approximate factorization (ADI-type) algorithm in delta-form. The steady-state form of the one described in Bridgeman et al. (1982) is used and details can be found there. The differencing scheme, in AF form, is given by

$$\begin{aligned}[I - h\bar{\delta}_\xi(\hat{\rho}A^{\xi\xi})^n\bar{\delta}_\xi][I - h\bar{\delta}_\eta(\hat{\rho}A^{\eta\eta})^n\bar{\delta}_\eta][I - h\bar{\delta}_\zeta(\hat{\rho}A^{\zeta\zeta})^n\bar{\delta}_\zeta] \\ \times(\phi^{n+1} - \phi^n) = h\omega\Big[\bar{\delta}_\xi(\hat{\rho}U^\phi)^n + \bar{\delta}_\eta(\hat{\rho}V^\phi)^n + \bar{\delta}_\zeta(\hat{\rho}W^\phi)^n \\ + \frac{U^B}{J}\delta_\xi\rho + \frac{V^B}{J}\delta_\eta\rho + \frac{W^B}{J}\delta_\zeta\rho - R_\infty\Big]\end{aligned} \tag{2.54}$$

where $\hat{\rho} = \rho/J$, and the superscript n refers to the iteration level. The differencing of the contravariant velocity component terms that appear on the right-hand side of equation (2.54) is illustrated by considering U^ϕ and U^B. Central differencing in space is used throughout, except for ϕ terms which are associated with a second derivative in ξ. Thus,

$$\begin{aligned}U^\phi_{j+\frac{1}{2}} = A^{\xi\xi}_{j+\frac{1}{2}}\Delta_\xi\phi_j + \frac{1}{2}\left(A^{\xi\eta}_{j+1}\delta_\eta\phi_{j+1} + A^{\xi\eta}_j\delta_\eta\phi_j\right) \\ + \frac{1}{2}\left(A^{\xi\zeta}_{j+1}\delta_\zeta\phi_{j+1} + A^{\xi\zeta}_j\delta_\zeta\phi_j\right)\end{aligned} \tag{2.55}$$

and

$$U^B = \xi_x u^B + \xi_y v^B + \xi_z w^B \tag{2.56}$$

where

$$u^B = (\xi_y \delta_\xi \psi + \eta_y \delta_\eta \psi + \zeta_y \delta_\zeta \psi) - (\xi_z \delta_\xi \chi + \eta_z \delta_\eta \chi + \zeta_z \delta_\zeta \chi)$$
$$v^B = (\xi_z \delta_\xi \vartheta + \eta_z \delta_\eta \vartheta + \zeta_z \delta_\zeta \vartheta) - (\xi_x \delta_\xi \psi + \eta_x \delta_\eta \psi + \zeta_x \delta_\zeta \psi) \qquad (2.57)$$
$$w^B = (\xi_x \delta_\xi \chi + \eta_x \delta_\eta \chi + \zeta_x \delta_\zeta \chi) - (\xi_y \delta_\xi \vartheta + \eta_y \delta_\eta \vartheta + \zeta_y \delta_\zeta \vartheta)$$

The V and W terms are also treated with central differencing except for ϕ terms associated with second derivatives in η alone and ζ alone, respectively.

The free-stream subtraction term, R_∞, appearing in the right-hand side of equation (2.54), accounts for incomplete metric cancellation (Bridgeman et al., 1982) and is given by

$$R_\infty = \bar{\delta}_\xi \left(\frac{\rho_\infty U_\infty}{J} \right) + \bar{\delta}_\eta \left(\frac{\rho_\infty V_\infty}{J} \right) + \bar{\delta}_\zeta \left(\frac{\rho_\infty W_\infty}{J} \right) \qquad (2.58)$$

An ADI algorithm is used to solve equation (2.54). Rewriting equation (2.54) in the form

$$L_\xi L_\eta L_\zeta (\phi^{n+1} - \phi^n) = R \qquad (2.59)$$

the ADI algorithm is implemented in three steps as

$$\begin{aligned} L_\xi \Delta\phi^* &= R \\ L_\eta \Delta\phi^{**} &= \Delta\phi^* \\ L_\zeta \Delta\phi^{n+1} &= \Delta\phi^{**} \\ \phi^{n+1} &= \phi^n + \Delta\phi^n \end{aligned} \qquad (2.60)$$

The algorithm given by equation (2.59) requires only a series of scalar, tridiagonal inversions and is, therefore, solved efficiently. It may also be noted that the rotational terms only appear explicitly in the residual. The relaxation parameter h, which appears in equation (2.54), is determined from the geometric sequence (Ballhaus et al., 1978):

$$\lambda = \lambda_1 \left(\frac{\lambda_2}{\lambda_1} \right)^{\frac{i-1}{N-1}}, \quad i = 1, 2, 3 \ldots N \qquad (2.61)$$

where $\lambda = 1/h$. A second overrelaxation parameter ω is used to scale the residual.

Each of the Poisson equations for the vector potential functions is updated in a similar manner, which results in the AF form,

$$\left[I - h\bar{\delta}_\xi \left(\frac{A^{\xi\xi}}{J}\right)^n \bar{\delta}_\xi\right]\left[I - h\bar{\delta}_\eta \left(\frac{A^{\eta\eta}}{J}\right)^n \bar{\delta}_\eta\right]\left[I - h\bar{\delta}_\zeta \left(\frac{A^{\zeta\zeta}}{J}\right)^n \bar{\delta}_\zeta\right]$$
$$\times(\vec{B}^{n+1} - \vec{B}^n) = h\omega\left[\bar{\delta}_\xi\left(\frac{\vec{B}^U}{J}\right)^n + \bar{\delta}_\eta\left(\frac{\vec{B}^V}{J}\right)^n + \bar{\delta}_\zeta\left(\frac{\vec{B}^W}{J}\right)^n + \frac{\vec{\omega}}{J}\right] \tag{2.62}$$

where

$$\vec{B}^U_{j+\frac{1}{2}} = A^{\xi\xi}_{j+\frac{1}{2}}\Delta_\xi\vec{B}_j + \frac{1}{2}\left(A^{\xi\eta}_{j+1}\delta_\eta\vec{B}_{j+1} + A^{\xi\eta}_j\delta_\eta\vec{B}_j\right) + \frac{1}{2}\left(A^{\xi\zeta}_{j+1}\delta_\zeta\vec{B}_{j+1} + A^{\xi\zeta}_j\delta_\zeta\vec{B}_j\right) \tag{2.63a}$$

and

$$\vec{B}^V_{k+\frac{1}{2}} = A^{\eta\eta}_{k+\frac{1}{2}}\Delta_\eta\vec{B}_k + \frac{1}{2}\left(A^{\xi\eta}_{k+1}\delta_\xi\vec{B}_{k+1} + A^{\xi\eta}_k\delta_\xi\vec{B}_k\right) + \frac{1}{2}\left(A^{\eta\zeta}_{k+1}\delta_\zeta\vec{B}_{k+1} + A^{\eta\zeta}_k\delta_\zeta\vec{B}_k\right)$$
$$\vec{B}^W_{l+\frac{1}{2}} = A^{\zeta\zeta}_{l+\frac{1}{2}}\Delta_\zeta\vec{B}_l + \frac{1}{2}\left(A^{\xi\zeta}_{l+1}\delta_\xi\vec{B}_{l+1} + A^{\xi\zeta}_l\delta_\xi\vec{B}_l\right) + \frac{1}{2}\left(A^{\eta\zeta}_{l+1}\delta_\eta\vec{B}_{l+1} + A^{\eta\zeta}_l\delta_\eta\vec{B}_l\right) \tag{2.63b}$$

The scheme given by equation (2.62) is implemented by the same three-step ADI algorithm given by equation (2.59).

2. Convection differencing and relaxation

The differencing used with the convection equation is illustrated by considering the entropy convection equation in general coordinates:

$$Us_\xi + Vs_\eta + Ws_\zeta = 0 \tag{2.64}$$

Assuming U is generally larger than V and W, this first order wave equation is discretized by using three-point, second-order-accurate central differencing in the

η- and ζ-directions, and three-point, second-order-accurate upwind differencing in the ξ-direction. Upwind differencing of Us_ξ is automatically achieved using

$$Us_\xi = U^+\delta_\xi^b s + U^-\delta_\xi^f s \tag{2.65}$$

where

$$U^+ = \frac{U + |U|}{2} \quad \text{and} \quad U^- = \frac{U - |U|}{2} \tag{2.66}$$

The convection equation is then solved using the AF relaxation algorithm

$$\begin{aligned}\left(I + hU^+\delta_\xi^b + hW\delta_\zeta\right)\left(I + hU^-\delta_\xi^f + hV\delta_\eta\right)\left(s^{n+1} - s^n\right) \\ = -h\left(U^+\delta_\xi^b + U^-\delta_\xi^f + V\delta_\eta + W\delta_\zeta\right)s^n\end{aligned} \tag{2.67}$$

where h is another relaxation parameter ($h > 0$). Because central differencing is used in the η- and ζ-directions, it is necessary to add fourth-order numerical dissipation terms to the differencing scheme to control the odd - even uncoupling of grid points and to control any nonlinear effects such as shocks (Pulliam, 1985). This is done explicitly in the numerical algorithm in order to be able to invert only tridiagonal matrices in the η- and ζ-directions. Second-order implicit dissipation is added to stabilize the explicit fourth-order dissipation for large values of the relaxation parameter h. Adding the numerical dissipation terms to the differencing scheme given by equation (2.67) results in the following scheme for the convection equation.

$$\begin{aligned}(I + hU^+\delta_\xi^b + hW\delta_\zeta - 3h|W|\Delta\nabla|_\zeta)(I + hU^-\delta_\xi^f + hV\delta_\eta - 3h|V|\Delta\nabla|_\eta) \\ \times(s^{n+1} - s^n) = -h\left[U^+\delta_\xi^b + U^-\delta_\xi^f + V\delta_\eta + W\delta_\zeta + |V|(\Delta\nabla)^2|_\eta + |W|(\Delta\nabla)^2|_\zeta\right]s^n\end{aligned} \tag{2.68}$$

Since the second-order dissipation terms are added implicitly, they do not change the steady-state solution of the convection equation. The algorithm given by equation

(2.68) is implemented in two steps as

$$\begin{aligned}(I + hU^+\delta_\xi^b + hW\delta_\varsigma - 3h|W|\Delta\nabla|_\varsigma)\Delta s^* = \\ -h\left[U^+\delta_\xi^b + U^-\delta_\xi^f + V\delta_\eta + W\delta_\varsigma + |V|(\Delta\nabla)^2|_\eta + |W|(\Delta\nabla)^2|_\varsigma\right]s^n\end{aligned} \tag{2.69}$$

$$(I + hU^-\delta_\xi^f + hV\delta_\eta - 3h|V|\Delta\nabla|_\eta)(s^{n+1} - s^n) = \Delta s^* \tag{2.70}$$

In the first step, a forward sweep in ξ is achieved by requiring a series of tridiagonal inversions in ς. In the second step, a backward sweep in ξ is achieved by requiring a series of tridiagonal inversions in η.

A similar algorithm can be used for solving the vorticity transport equations (2.47) by replacing the numerical dissipation terms with the viscous diffusion terms. The details of the algorithm used for solving the vorticity transport equation will be presented in Chapter IV.

3. Integration algorithm for vorticity

The consistency relation for vorticity, equation (2.51), is used to integrate ω_1 in the ξ-direction from an upstream boundary to the outflow boundary. Equation (2.51) can be represented in the form

$$a_1 f_\xi + a_2 f_\eta + a_3 f_\varsigma = a_4 \tag{2.71}$$

where $f = \omega_1$, $a_1 = \xi_x$, $a_2 = \eta_x$, $a_3 = \varsigma_x$, and a_4 contains the remaining terms of equation (2.51).

Consider differencing this equation on a j-plane using first-order one-sided differencing in ξ and central differencing in η and ς. That is, at the jth plane

$$\begin{aligned}a_1(f_j - f_{j-1}) + a_2\frac{(f_{k+1} - f_{k-1})}{2}\Big|_j \\ + a_3\frac{(f_{l+1} - f_{l-1})}{2}\Big|_j = a_4\end{aligned} \tag{2.72}$$

Putting into the delta form, $f_j - f_{j-1}$, dividing by a_1, and approximately factoring, this difference equation is written as

$$(I + \frac{a_2}{a_1}\delta_\eta)(I + \frac{a_3}{a_1}\delta_\zeta)(f_j - f_{j-1}) = \frac{a_4}{a_1} - (\frac{a_2}{a_1}\delta_\eta + \frac{a_3}{a_1}\delta_\zeta)f_{j-1} \tag{2.73}$$

If three-point, second-order forward differencing is used for f_ξ, this becomes

$$(I + \frac{2a_2}{3a_1}\delta_\eta)(I + \frac{2a_3}{3a_1}\delta_\zeta)(f_j - f_{j-1}) = \frac{2}{3}\frac{a_4}{a_1} + \frac{1}{3}(f_{j-1} - f_{j-2}) - \frac{2}{3}(\frac{a_2}{a_1}\delta_\eta + \frac{a_3}{a_1}\delta_\zeta)f_{j-1} \tag{2.74}$$

Note that this approximate factorization is using a space delta, not an iteration delta. First-order backward differencing is used at the first ξ = constant plane, and second-order differencing is used at all successive planes to integrate the consistency relation for ω_1. At each ξ-plane, the algorithm requires a series of simple tridiagonal inversions in η and ζ.

4. Consistency boundary condition

The consistency relation for the vector potential functions is implemented at boundary surfaces by a procedure similar to the one described above for integrating the vorticity consistency relation. Consistency boundary conditions are illustrated below for the case in which the body boundary-surface coincides with a ζ = constant plane. Other boundary surfaces receive similar treatment.

Differencing equation (2.50) on the ζ = constant surface, $l = 1$, using first-order one-sided differencing in ζ, and central differencing in ξ and η, gives

$$\xi_z \frac{(\psi_{j+1} - \psi_{j-1})}{2}\Big|_{l=1} + \eta_z \frac{(\psi_{k+1} - \psi_{k-1})}{2}\Big|_{l=1} + \zeta_z(\psi_2 - \psi_1) = a_4|_{l=1} \tag{2.75}$$

where

$$a_4 = -[(\xi_x \delta_\xi \vartheta + \eta_x \delta_\eta \vartheta + \varsigma_x \Delta_\varsigma \vartheta) + (\xi_y \delta_\xi \chi + \eta_y \delta_\eta \chi + \varsigma_y \Delta_\varsigma \chi)] \tag{2.76}$$

Putting this into the delta form, $\psi_1 - \psi_2$, dividing by $-\varsigma_z$, and approximately factoring, the difference equation

$$(I - \frac{\xi_z}{\varsigma_z}\delta_\xi)(I - \frac{\eta_z}{\varsigma_z}\delta_\eta)(\psi_1 - \psi_2) = (\frac{\xi_z}{\varsigma_z}\delta_\xi + \frac{\eta_z}{\varsigma_z}\delta_\eta)\psi_2 - \frac{a_4}{\varsigma_z} \tag{2.77}$$

is solved on the surface for $(\psi_1 - \psi_2)$ by inverting tridiagonal matrices in ξ and then in η. If three-point second-order forward differencing is used for ς-derivatives, equation (2.77) is modified in the same way that equation (2.73) is changed to equation (2.74).

5. Tangency boundary condition

Tangency or no-flow-through is imposed on a boundary surface by setting the appropriate contravariant velocity component to zero. On a ς = constant plane, W is set to zero. Tangency is enforced through implicit boundary conditions on ϕ, which are obtained by solving the continuity equation at the half-cells neighboring a solid boundary. The procedure is illustrated by considering a finite-difference cell (Figure 1). The center of the cell is located at $(j, k, l + \frac{1}{4})$. The finite-difference form of equation (2.44) can be written as

$$\left[\frac{(\hat{\rho}U)_{j+\frac{1}{2},k,l+\frac{1}{4}} - (\hat{\rho}U)_{j-\frac{1}{2},k,l+\frac{1}{4}}}{\Delta\xi}\right] + \left[\frac{(\hat{\rho}V)_{j,k+\frac{1}{2},l+\frac{1}{4}} - (\hat{\rho}V)_{j,k-\frac{1}{2},l+\frac{1}{4}}}{\Delta\eta}\right] + \left[\frac{(\hat{\rho}W)_{j,k,l+\frac{1}{2}} - \cancel{(\hat{\rho}W)_{j,k,l}}^{0}}{\Delta\varsigma/2}\right] = 0 \tag{2.78}$$

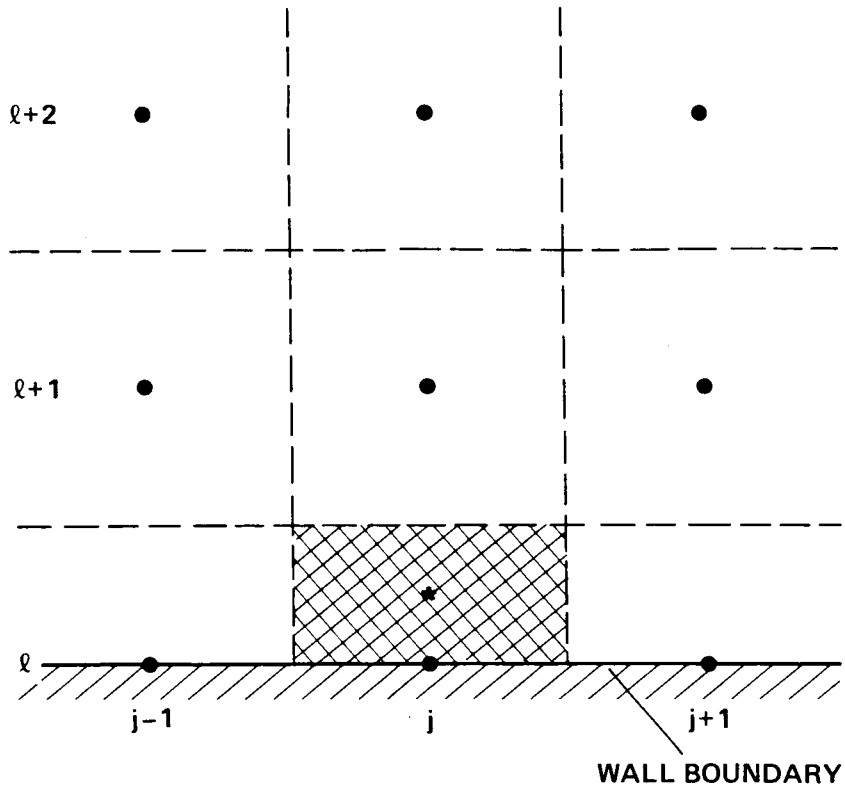

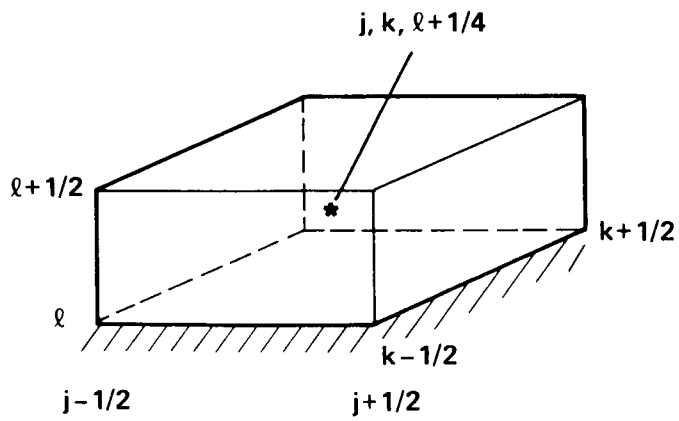

Figure 1. Finite-difference cell near a wall boundary

Evaluating variables at $l + \frac{1}{4}$ by weighted averaging between l and $l + 1$ as, for example,

$$\begin{aligned} U_{j+\frac{1}{2},k,l+\frac{1}{4}} &= \frac{3}{4}U_{j+\frac{1}{2},k,l} + \frac{1}{4}U_{j+\frac{1}{2},k,l+1} \\ &= (I + \frac{1}{4}\Delta_\zeta)U_{j+\frac{1}{2},k,l} \end{aligned} \tag{2.79}$$

where

$$\begin{aligned} U_{j+\frac{1}{2},k,l} = A^{\xi\xi}_{j+\frac{1}{2}}\Delta_\xi\phi_j + \frac{1}{2}(A^{\xi\eta}_{j+1}\delta_\eta\phi_{j+1} + A^{\xi\eta}_{j}\delta_\eta\phi_j) \\ + \frac{1}{2}(A^{\xi\zeta}_{j+1}\Delta_\zeta\phi_{j+1} + A^{\xi\zeta}_{j}\Delta_\zeta\phi_j) + \text{vector potential terms} \end{aligned} \tag{2.80}$$

equation (2.78) can be written as

$$\begin{aligned} &(I + \frac{1}{4}\Delta_\zeta)(\hat{\rho}U)_{j+\frac{1}{2}} - (I + \frac{1}{4}\Delta_\zeta)(\hat{\rho}U)_{j-\frac{1}{2}} + \\ &(I + \frac{1}{4}\Delta_\zeta)(\hat{\rho}V)_{k+\frac{1}{2}} - (I + \frac{1}{4}\Delta_\zeta)(\hat{\rho}V)_{k-\frac{1}{2}} + 2(\hat{\rho}W)_{l+\frac{1}{2}} = 0 \end{aligned} \tag{2.81}$$

To facilitate the application of approximate factorization, the cross-derivative and vector potential terms are lagged in time in the usual way to obtain the relaxation algorithm

$$\begin{aligned} &[I - h\bar{\delta}_\xi(\hat{\rho}A^{\xi\xi})^n\bar{\delta}_\xi][I - h\delta_\eta(\hat{\rho}A^{\eta\eta})^n\delta_\eta][I - 2h(\hat{\rho}A^{\zeta\zeta})^n_{l+\frac{1}{2}}\Delta_\zeta] \\ &\times (\phi^{n+1} - \phi^n) = h\omega\{\bar{\delta}_\xi(\hat{\rho}U)^n + \bar{\delta}_\eta(\hat{\rho}V)^n + 2(\hat{\rho}W)^n_{l+\frac{1}{2}} \\ &+ \frac{1}{4}\Delta_\zeta[\bar{\delta}_\xi(\hat{\rho}U^n) + \bar{\delta}_\eta(\hat{\rho}V^n)]\} \end{aligned} \tag{2.82}$$

Equation (2.82) is of the same form as equation (2.54) and hence tangency can be enforced implicitly in the ADI algorithm given by equation (2.59) with the tridiagonal and right-hand-side terms modified appropriately.

III. INVISCID ROTATIONAL FLOW

For many practical flow situations, the inviscid approximation gives a very useful and accurate estimate of the flowfield. This is especially true when viscous effects are small and confined to a thin shear layer adjacent to the wall and when the flow remains attached and does not separate, thereby diffusing and convecting vorticity into the outer flow. In this chapter, the solution scheme for the Euler equations is presented together with applications to inviscid three-dimensional rotational flow. The approach taken is to increase the complexity of the approximations regarding the flow. First, the solution to an irrotational inviscid flow is obtained. Then, an inviscid solution of the secondary flow produced by a nonuniform stagnation pressure is obtained. In particular, the three-dimensional dual potential procedure outlined in Chapter II has been used to simulate the flow through the inlet of an indraft wind tunnel and numerical results for this case are presented in this chapter along with some experimental data for comparison.

A. Solution Strategy

The dual potential formulation outlined in the previous chapter has several advantages. In an iterative solution scheme, the governing equations (2.44) - (2.46), (2.48) - (2.51) are weakly coupled and hence can be solved separately as described below. The rotational and irrotational components of velocity are also decoupled. As a result, the vector potential functions need be determined in only the rotational part of the flow domain.

Because the equations are weakly coupled, an efficient iterative solution procedure can be used with each equation updated sequentially using the numerical algorithms described in Chapter II. At each grid point an initial guess is made for

values of ϕ, ϑ, χ, ψ, s, ρ, and for ω_1, ω_2, and ω_3. The following iteration scheme is then implemented:

1) Vector potential functions, ϑ, χ, ψ. Individually update ϑ, χ, and ψ from the Poisson equations given by equation (2.45) for assumed values of ω_1, ω_2, and ω_3. Boundary conditions for these equations are kept compatible with the consistency relation, equation (2.50).

2) Scalar potential function, ϕ. Update ϕ from the continuity equation (2.44) using the ADI-like algorithm for the transonic full potential function and previously updated values of ϑ, χ, and ψ.

3) Entropy, s. Using updated values of ϑ, χ, ψ, and ϕ, evaluate U, V, and W and update s from the convection equation (2.48).

4) Density, ρ. Update density from the Bernoulli equation (2.28), using previously updated values of u, v, w, and s.

5) Vorticities, ω_1, ω_2, and ω_3. Vorticity components are evaluated from Crocco's equations and the consistency relation for vorticity. Assuming $u > |v|$ and $|w|$ and $u \neq 0$, ω_2 and ω_3 are evaluated from equation (2.46) as

$$\begin{aligned} \omega_2 &= \left[v\omega_1 - T(\xi_z s_\xi + \eta_z s_\eta + \zeta_z s_\zeta)\right]/u \\ \omega_3 &= \left[w\omega_1 + T(\xi_y s_\xi + \eta_y s_\eta + \zeta_y s_\zeta)\right]/u \end{aligned} \tag{3.1}$$

and ω_1 is determined from the vorticity consistency relation, equation (2.51).

6) Test for convergence and, if necessary, return to (1).

For incompressible flow, density is taken to be constant, and Crocco's equations and the entropy convection equation are replaced by Lamb's equations and the total pressure convection equation, respectively. In this case, ω_2 and ω_3 are evaluated as

$$\begin{aligned} \omega_2 &= \left[v\omega_1 + (\xi_z p_{0_\xi} + \eta_z p_{0_\eta} + \zeta_z p_{0_\zeta})/\rho\right]/u \\ \omega_3 &= \left[w\omega_1 - (\xi_y p_{0_\xi} + \eta_y p_{0_\eta} + \zeta_y p_{0_\zeta})/\rho\right]/u \end{aligned} \tag{3.2}$$

and ω_1 is again determined from the vorticity consistency relation.

B. Geometry and Grid

As a first application, the three-dimensional dual potential procedure outlined above was used to compute the flow through the 80- by 120-ft leg of the National Full Scale Aerodynamics Complex (NFAC) at the NASA Ames Research Center. A view of the complex is shown in Figure 2. Screens and vanes are placed at the entrance of the inlet in order to isolate the test section from outside winds. Also, the screens prevent birds and other objects from entering the tunnel. The presence of these screens and vanes is accounted for in the numerical simulation as a jump condition based on actuator disk theory. The contraction ratio for the tunnel is 5:1 and the Mach number in the test section does not exceed 0.2. The fluid is, therefore, assumed to be incompressible in the numerical procedure.

A three-dimensional grid to model the 80- by 120-ft leg of the NFAC was generated using simple algebraic shearing. Figure 3 shows a view of the tunnel walls and floor. A comparison of Figures 2 and 3 shows that the grid represents the NFAC accurately except for the rounded lip at the entrance of the inlet. To avoid a complex grid generation task, the rounded lip was not modeled. Since the 80- by 120-ft wind tunnel rests on the ground, the grid and the boundary conditions must model the ground plane in order to obtain the correct inflow conditions. The computational domain includes the wind tunnel and its surrounding region to facilitate the application of boundary conditions in the far-field. All calculations were performed on a $39 \times 41 \times 34$ grid of which $26 \times 17 \times 21$ grid points are interior to the wind tunnel. The tunnel walls are modeled to have a thickness equal to a single grid increment. The actuator disk modeling the screens and/or vanes is located at

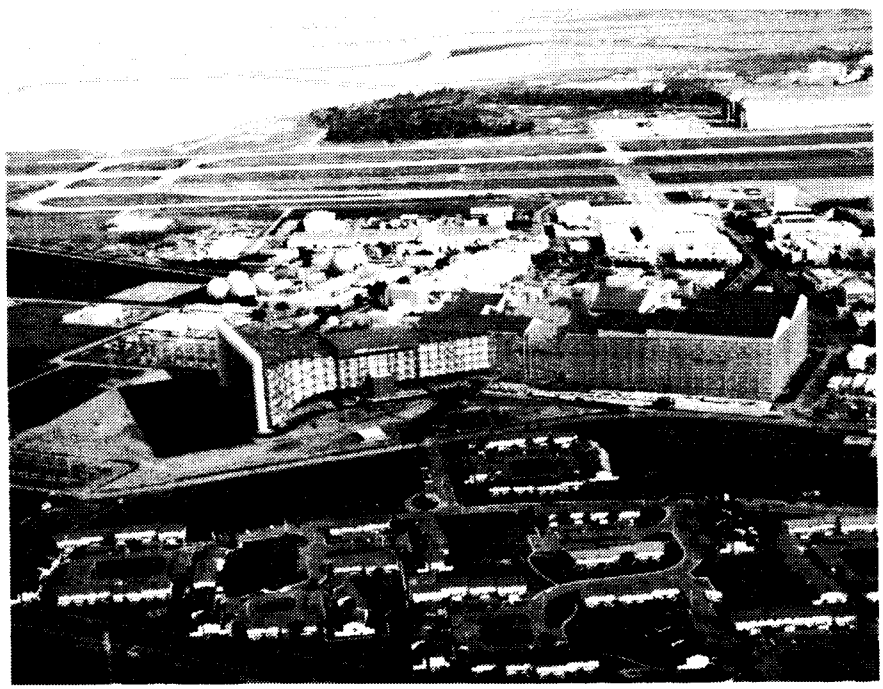

Figure 2. The National Full Scale Aerodynamics Complex

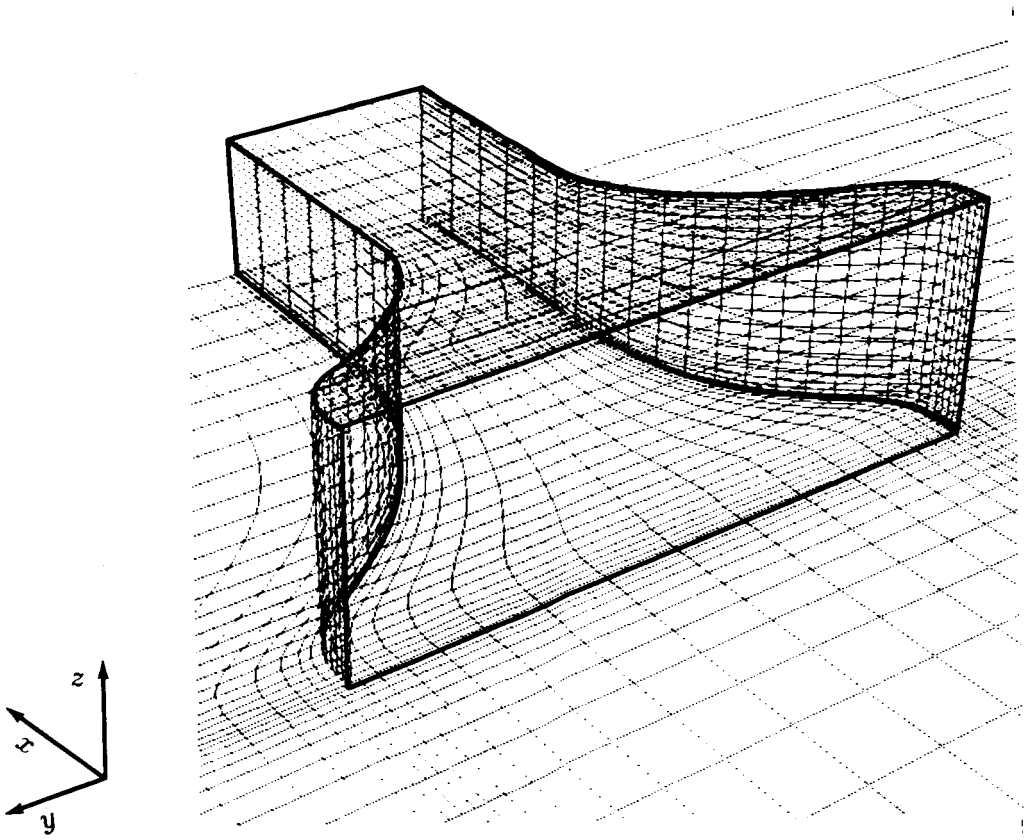

Figure 3. Perspective view of the grid for the NFAC inlet model showing the ground plane and tunnel walls

a ξ = constant plane corresponding to the location of the trailing edge of the vanes in the actual configuration. Figures 4 and 5 show views of three different planes of the grid. A detail of the grid is given in Figure 5 to illustrate the modeling of the tunnel walls. The average width of the test section, 100 feet, was chosen as the reference length in the calculations, and all results are presented accordingly.

The flow is assumed to be irrotational outside of the tunnel, and only the potential function, ϕ, needs to be computed there. Upstream and in the farfield, the value of the potential is kept constant at its free-stream value. At outflow, outside the tunnel, the streamwise component of velocity is allowed to vary by using a zero-gradient boundary condition on U. Tangency is enforced at the ground plane and at all the tunnel walls (interior and exterior) through the implicit boundary conditions on ϕ described earlier. The flow rate through the tunnel is determined by specifying the axial velocity ϕ_x at the outflow boundary within the tunnel. On each tunnel wall, the vector potential corresponding to the near-normal direction to the surface is obtained from its consistency relation, and the other two vector potential functions are kept constant. For example, on the ground plane ς = constant, ϑ and χ are set to zero, while ψ is obtained from equation (2.50). At the outflow boundary ξ = constant, χ and ψ are obtained using a second-order extrapolation technique, whereas ϑ is computed from the vector potential consistency relation.

In the absence of any screens and/or vanes, the entire flow is assumed irrotational and hence only ϕ needs to computed, with the other variables being constant. With screens and vanes, a total pressure loss across these devices sets up a rotational flow field inside the tunnel which is accounted for by solving for the total pressure (incompressible formulation), vorticity, and the vector potential functions. It is necessary to solve for these variables only within the tunnel since the flow

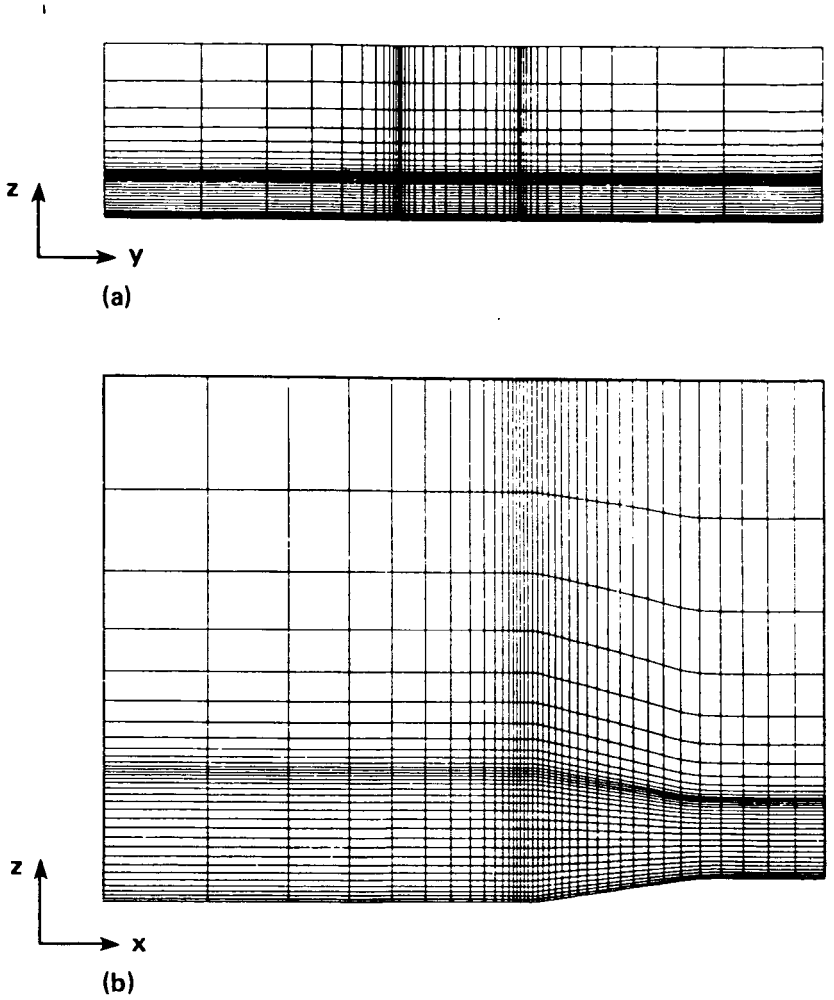

Figure 4. Cross-sectional views of the sheared grid for the 80- by 120-ft leg of the NFAC. a) Grid in the y-z plane at inlet entrance; b) Grid in the x-z plane at mid-span

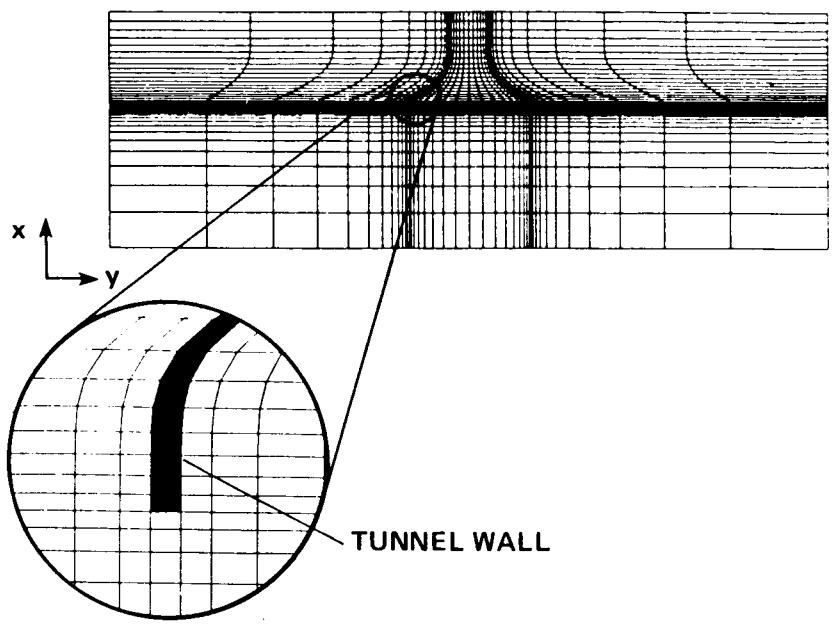

Figure 5. Cross-sectional view of the sheared grid for the 80- by 120-ft leg of the NFAC in the x-y plane at mid-height

upstream of the vanes and screens is taken to be irrotational. Inflow boundary conditions for total pressure and the vector potential functions are obtained from the actuator disk model for the vanes and screens.

C. Actuator Disk Model

The presence of vanes and screens at the entrance of the wind-tunnel inlet is modeled using actuator disk theory (Horlock, 1978; Ross et al., 1986) in which these devices are idealized to a jump condition. Vanes and screens constrain the flow in some specified direction and produce a drag force opposing the motion of the fluid. The drag or resistance produced by vanes and screens can be expressed in terms of the total pressure loss across the actuator disk model. For a given screen or vane, the total pressure drop can be determined empirically as a function of the local dynamic head as

$$p_{0_2} = p_{0_1} - K\frac{1}{2}\rho q_1^2 \tag{3.3}$$

Here, the subscripts 1 and 2 refer to locations immediately upstream and downstream of the actuator disk as indicated in Figure 6. The loss coefficient K is empirically determined as a function of the local Reynolds number, onset flow angle, and the geometrical characteristics of the screens and vanes. The contribution to the loss coefficient from the vanes and the screens may be separated into two components as

$$K = K_v + K_s \tag{3.4}$$

where K_v denotes the vane-loss coefficient and K_s the screen-loss coefficient.

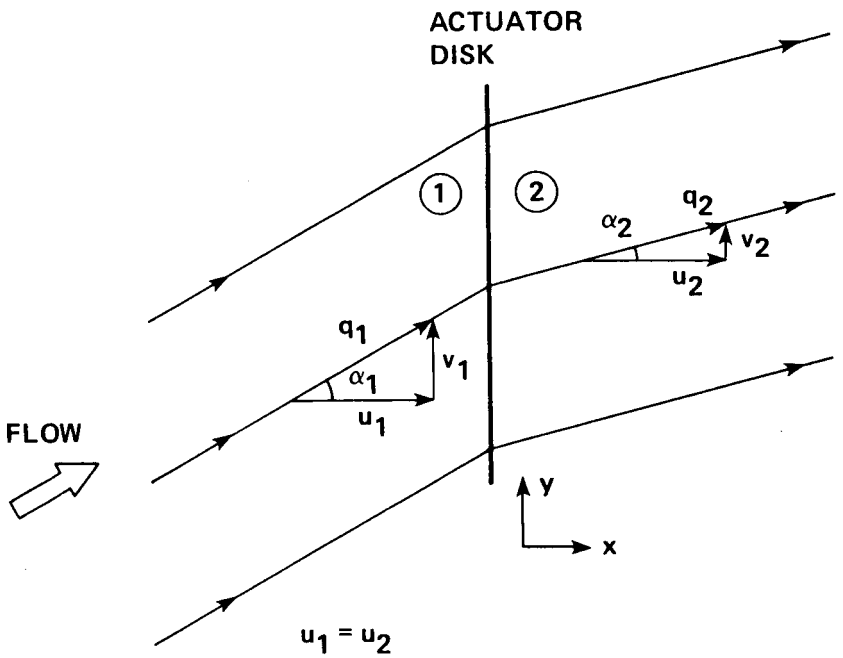

$u_1 = u_2$

JUMP RELATIONS:

$$p_{0_2} = p_{0_1} - K_s \frac{1}{2} \rho (u_1^2 + v_1^2)$$

$$v_2 = (1 - C) v_1$$

K_s & C = func(Re, α_1)

Figure 6. Deflection of flow through an actuator disk model for a screen

1. Flow through a screen

The screen is modeled as an actuator disk located in the flow field as indicated schematically in Figure 6. Variables at the locations upstream and downstream of the disk are denoted with the subscripts 1 and 2, respectively. The following equations describe incompressible flow through the disk.

Continuity:

$$u_1 = u_2 \tag{3.5}$$

Momentum in x-direction:

$$p_1 - p_2 - D_x = \rho u_2^2 - \rho u_1^2 \tag{3.6}$$

where D_x is the drag force in the x-direction and is obtained from the characteristics of the screen and the upstream flow conditions. The loss coefficient, based on the static pressure drop and expressed as a function of the dynamic head is found to be a function of the local Reynolds number, (Re), for onset angles, α, up to 40°. That is,

$$K_{so} = \frac{D_x}{\frac{1}{2}\rho q^2} = \frac{p_1 - p_2}{\frac{1}{2}\rho q^2} = f(Re) \tag{3.7}$$

In addition to creating a pressure drop, the screens have the effect of straightening the flow through them. It is found (Horlock, 1978) that at a given Reynolds number, the change in the tangent of the flow angle is a function of the upstream flow angle, that is,

$$\tan\alpha_1 - \tan\alpha_2 = f(\tan\alpha_1) \tag{3.8}$$

or

$$u_1 \tan\alpha_1 - u_2 \tan\alpha_2 = F(u_1 \tan\alpha_1) \tag{3.9}$$

For onset flow angles up to 40°, the change in the tangent of the flow angle is found to be proportional to the upstream flow angle, that is

$$c_1 - c_2 = Cc_1 \tag{3.10}$$

where $c = u \tan \alpha = (v^2 + w^2)^{1/2}$ is the lateral component of velocity.

The empirical parameters, K_{so} and C are determined from the upstream conditions and the physical screen characteristics (porosity, wire diameter). An additional simplification is achieved by assuming that equation (3.10) is valid for both tangential components of velocity, that is,

$$v_1 - v_2 = Cv_1 \tag{3.11}$$

$$w_1 - w_2 = Cw_1 \tag{3.12}$$

The total pressure drop across the screen is given by

$$\frac{p_{0_1} - p_{0_2}}{\frac{1}{2}\rho q^2} = \frac{p_1 - p_2}{\frac{1}{2}\rho q^2} + (c_1^2/q^2 - c_2^2/q^2) \tag{3.13}$$

which reduces to

$$K_s = K_{so} + (2C - C^2)\sin^2 \alpha_1 \tag{3.14}$$

The two constants, K_{so} and C needed to determine the total pressure loss for the NFAC have been determined experimentally and reported by Ross et al. (1986) and van Aken (1986).

2. Flow through vanes

In addition to screens, many wind tunnels employ a a cascade of vanes at the entrance in order to assist in providing a uniform test-section flow. The distribution of the splay angle of the cascade is an important factor in minimizing the variation

in test-section total pressure (Ross et al., 1986). The loss coefficient for the cascade is a function of the individual drag coefficient of the vanes including its geometric characteristics such as the pitch, chord and solidity. For the 80- by 120-ft leg of the NFAC, the loss coefficient for the cascade is obtained from van Aken (1986) and is found to be 0.4. Another important effect of the cascade is to direct the flow at the inlet entrance at a specified angle thereby determining the lateral component of velocity as

$$v_2 = u_2 \tan\theta \tag{3.15}$$

where θ is the splay or turning angle. Various splay angle distributions were tried for the NFAC and have been reported by Ross et al. (1986). Finally, it may also be useful and even necessary, as in the case of the NFAC to control the vertical component of velocity, w. This is done by the construction of splitter plates, running laterally between the two side walls of the tunnel, which are located at different heights of the vanes to form something like a honeycomb screen at the inlet entrance. For the NFAC the splitter plates have been constructed horizontally along the width of the tunnel, so that the fluid leaves the plates without any vertical component of velocity, that is,

$$w_2 = 0 \tag{3.16}$$

The coefficients K_v, K_s, and C used in this study are based on the experimental data of Ross et al. (1986) and van Aken (1986). Except for one case (Figure 9), values of $K_s = 1.8, K_v = 0.4$, and $C = 0.2$ were used in the numerical simulations.

3. Implementation of actuator disk model

This actuator disk model is implemented in the numerical simulation by adopting the following procedure at each iteration level. Letting j be the grid point at

which the actuator disk is located, and using the subscripts 1 and 2 for values just upstream and downstream of the disk,

- u_1, v_1, w_1 at j are calculated from equation (2.34) using backward differences for the x- or ξ-derivatives, that is, making use of values at j and $j-1$.
- p_{0_2} at j is calculated from equation (3.3) using appropriate values of K. It may be noted that p_{0_1} is a constant for the irrotational flow upstream and hence known from free-stream conditions.
- v_2 and w_2 at j are calculated using equations (3.11) and (3.12) for screens alone or equations (3.15) and (3.16) for screens and vanes.
- ω_1 at j is calculated from its definition using values of v_2 and w_2 as

$$\omega_1 = w_y - v_z \tag{3.17}$$

- ϑ is set to zero at j.
- χ and ψ at j are calculated so that v_2 and w_2 are prescribed using forward differences in x as

$$\begin{aligned} \psi_j &= \psi_{j+1} - (\phi_y - v_2)\Delta x \\ \chi_j &= \chi_{j+1} - (w_2 - \phi_z)\Delta x \end{aligned} \tag{3.18}$$

- Finally, the continuity equation through the actuator disk, equation (3.5), is enforced by evaluating ϕ at j using appropriate differencing in x. That is, equation (3.5) is differenced as

$$u_1 = (\phi_j - \phi_{j-1})/\Delta x = u_2 = (\phi_{j+1} - \phi_j)/\Delta x + (\psi_y - \chi_z) \tag{3.19}$$

Collecting terms involving ϕ on one side, the above equation can be rewritten as

$$(-\phi_{j+1} + 2\phi_j - \phi_{j-1}) = (\psi_y - \chi_z)\Delta x \tag{3.20}$$

This constraint on ϕ_j is enforced implicitly in the ADI algorithm for ϕ to accelerate convergence and improve stability.

D. Results and Discussion

1. Irrotational flow

As a simple verification of the numerical procedure, Figures 7 and 8 show solutions obtained for potential flow alone ($K = 0$) compared with other numerical computations and experimental data as taken from Kaul et al. (1985). The experimental results presented throughout were obtained from a 1/15-scale model of the NFAC. Figure 7 shows the variation of the pressure coefficient, $Cp = (p - p_t)/\frac{1}{2}\rho u_t^2$, on the side wall versus length at mid-height of the tunnel. Here, the subscript t refers to the test section, which is at the outflow boundary in the present simulation. Experimental data are also plotted in Figure 7 and the agreement between the present results and the experimentally measured values is quite good. The spike in the present results is likely a result of the simple lip treatment. Figure 8 is a comparison of the pressure coefficient along the center of the tunnel floor, with Euler and panel methods. The panel method results agree very well with the present results, whereas the Euler method differs in the entrance region of the inlet. These calculations required about 5 μsec per iteration per grid point on a CRAY XMP vector processor and fully converged results were obtained in 900 iterations which correspond to about 240 sec of CPU time.

2. Rotational flow

In the design of wind tunnels, it is, of course, essential to maintain uniform flow in the test section, and screens and vanes (located upstream of the test sec-

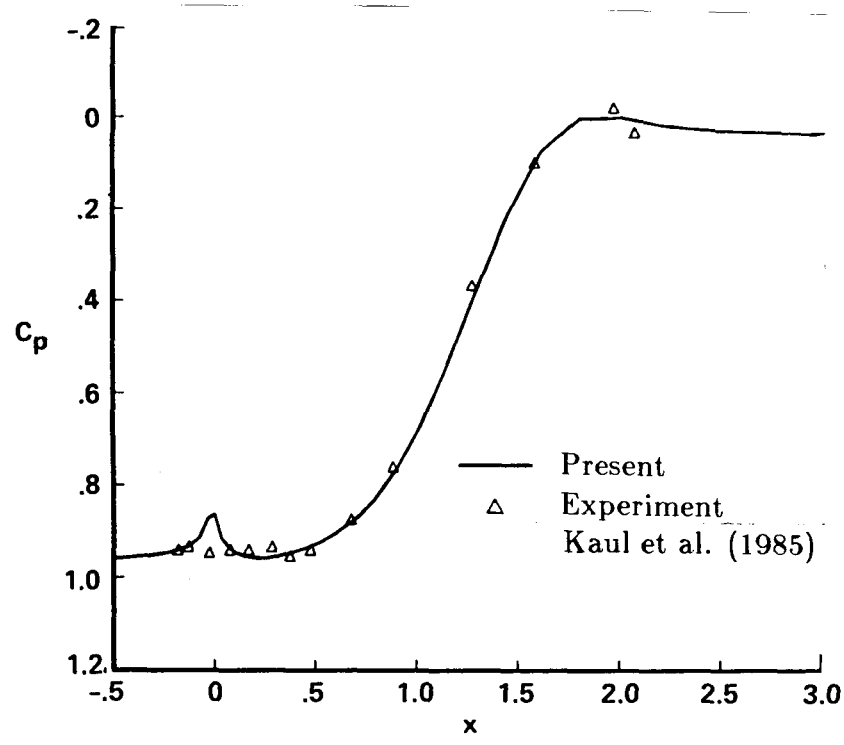

Figure 7. Variation of pressure coefficient with length along a side wall at mid-height of the tunnel

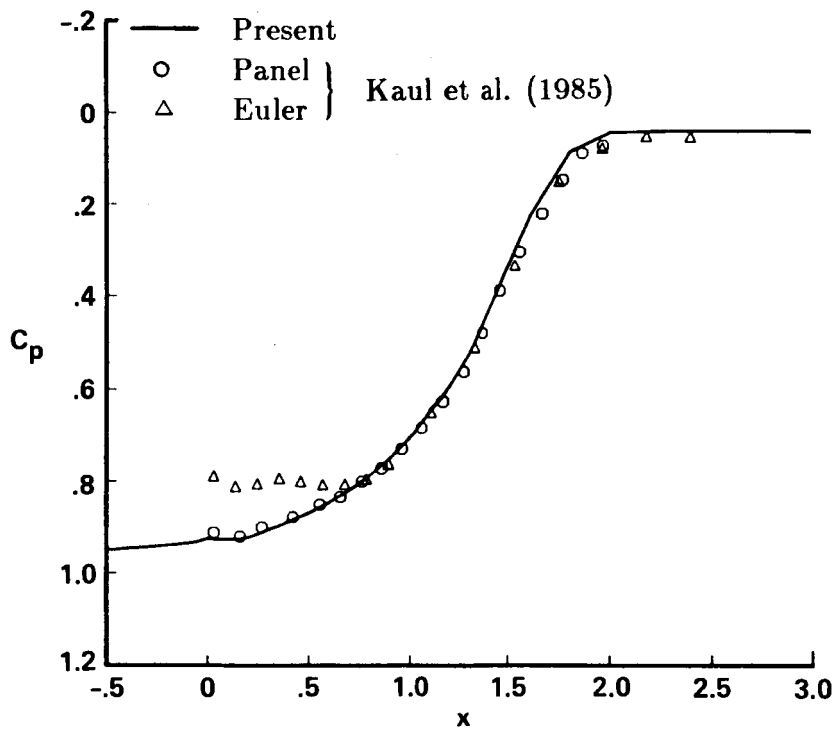

Figure 8. Variation of pressure coefficient with length on the tunnel floor at mid-span

tion) are frequently used to improve the flow quality in the test section and isolate the wind tunnel from external turbulence. However, these devices induce a total pressure loss that varies with the upstream dynamic pressure. If they are placed in a region with substantial variation of upstream velocity, they can induce a significant total pressure variation (and, therefore, rotational flow) that can persist far downstream. Placing a screen in the wind-tunnel inlet can therefore induce an undesirable nonuniform flow in the test section. This effect is demonstrated in Figure 9 for the original NFAC inlet; the figure shows the variation of the dynamic pressure in the test section with the spanwise distance, y, at mid-height in the tunnel. The quantity plotted in this figure is the normalized dynamic pressure, $(q/q_{cl})^2$, where the subscript *cl* refers to the centerline. Three numerical results are shown in the figure: screens alone, screens and straight vanes, and screens and splayed vanes. In one case, the vanes are straight, that is, they are aligned with the axis of the tunnel [$\theta = 0$ in equation (3.15)] just as in the original NFAC design. In the other case the vanes are splayed at angles developed for the redesigned NFAC (Ross et al., 1986; van Aken, 1986). Along with the numerical results, experimental data from a 1/15-scale model with straight vanes (van Aken, 1986) are also plotted in this figure. The agreement with experiment is relatively good and indicates that the original inlet configuration results in an unacceptably high variation of flow quality in the test section.

A numerical and experimental study of the NFAC (Ross et al., 1986) resulted in a slight modification to the inlet geometry. The curved walls in the span (or y-direction) were replaced with straight walls near the entrance of the inlet and the vanes were splayed at angles that are close to the "ideal" streamline angles at the entrance of the inlet. A schematic view of this new geometry is shown in

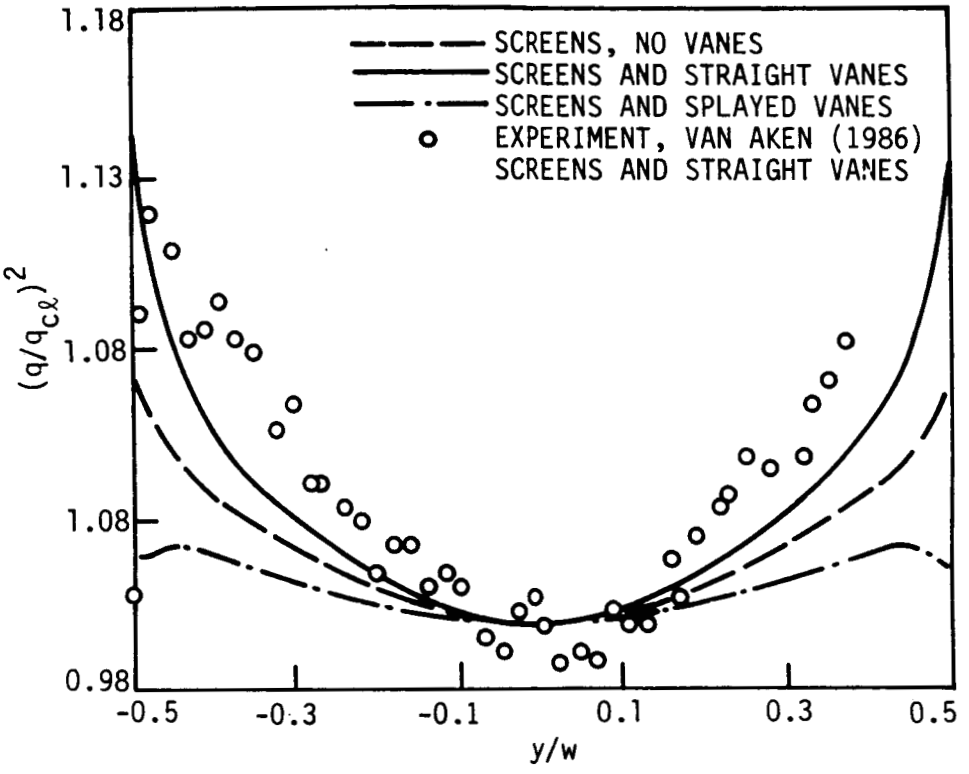

Figure 9. Variation of dynamic pressure in the test section with span at mid-height, $K_s = 1.6, K_v = 0.396$

Figure 10; again, the true lip geometry is not represented. Results obtained for this modified tunnel are shown in Figures 10-14. Also shown in these figures are experimental data from a 1/15-scale model (van Aken, 1986). Figure 10 shows the variation of the total pressure coefficient, $(p_0 - p_{0_{cl}})/\frac{1}{2}\rho q_{cl}^2$, with spanwise distance at mid-height of the test section. Again, two splay distributions were examined: zero splay angles and the redesigned splay distribution. The results show a dramatic improvement in test-section flow quality for the case of splay distribution and the agreement with experiment is good except near the walls. This is perhaps expected because viscous effects are not taken into account in the present procedure and the correct lip geometry is not modeled. Figures 11 through 14 compare predictions with measurements of the dynamic pressure at various height and span locations in the test section. Overall, the agreement with experiment is satisfactory except near the walls.

The above calculations were performed with zero free-stream velocity, that is, with no wind outside the tunnel. With the present code, a variety of outside wind conditions can be simulated by changing the far-field boundary conditions on ϕ (including rotational incoming flow if the vector potential functions are solved there). The effect of wind direction on the test-section flow quality was studied by simulating a case in which the wind velocity was about 15% of the test-section velocity and blowing at an angle of 45° with respect to the axis of the tunnel. The results are presented in Figure 15, along with results for the case in which the wind was blowing at 0°. Figure 15a shows the spanwise variation of dynamic pressure at mid-height, and Figure 15b shows the variation of the dynamic pressure with height at mid-span of the test section. The results indicate that the vanes, inlet length, and screens do a relatively good job of isolating the test section from such extreme variation in

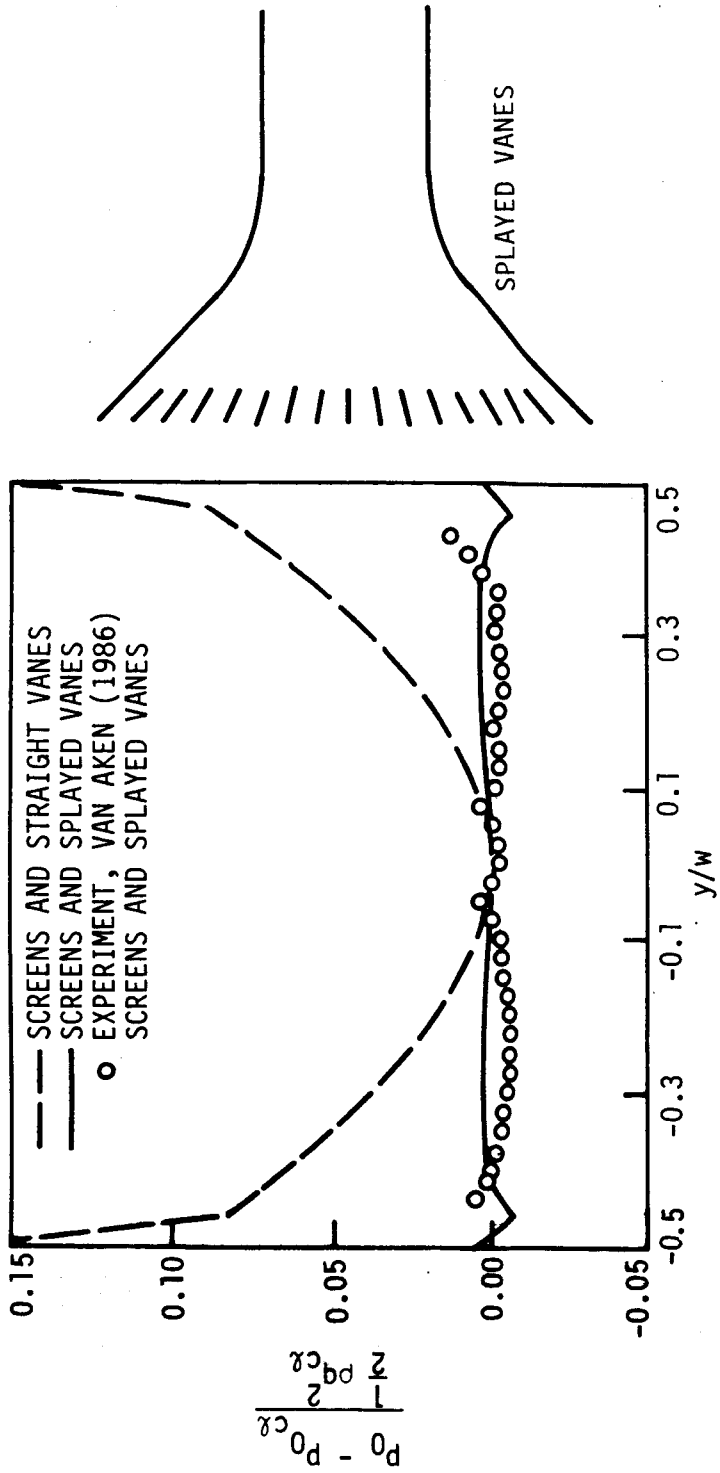

Figure 10. Variation of total pressure coefficient in the test section with spanwise distance at mid-height

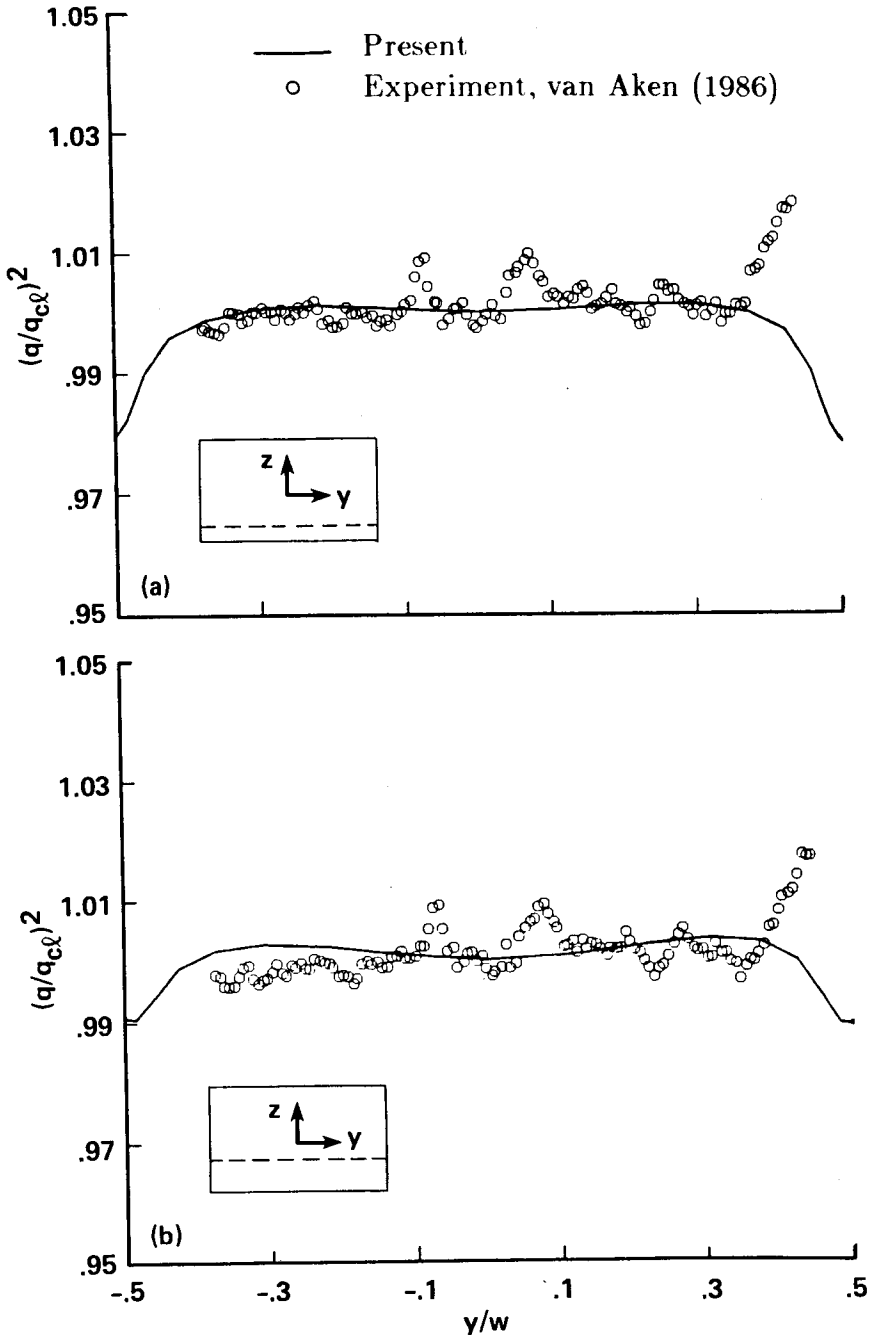

Figure 11. Spanwise variation of dynamic pressure in the test section at different height locations: a) $z/h = -0.332$; b) $z/h = -0.166$

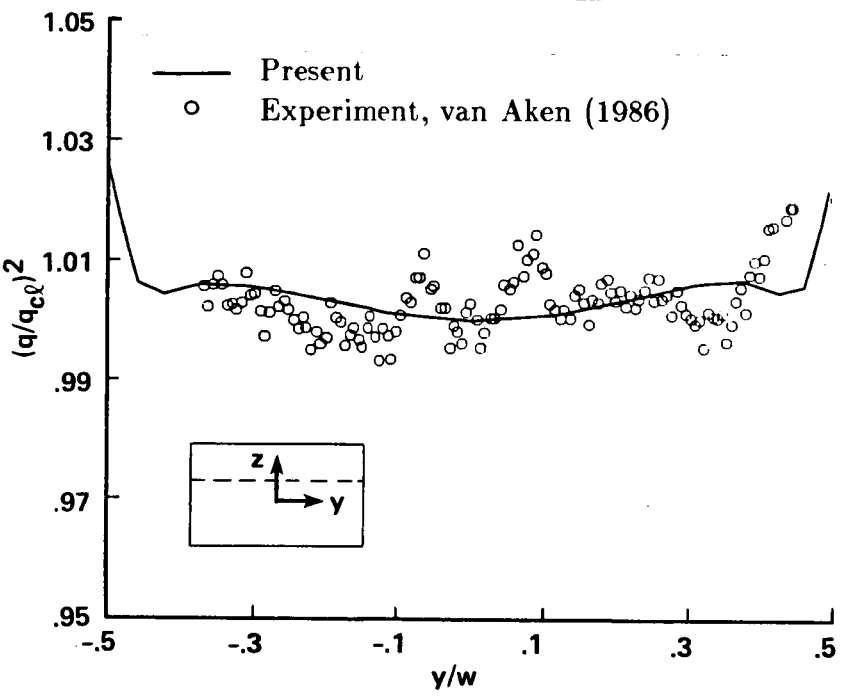

Figure 12. Spanwise variation of dynamic pressure in the test section at $z/h = 0.166$

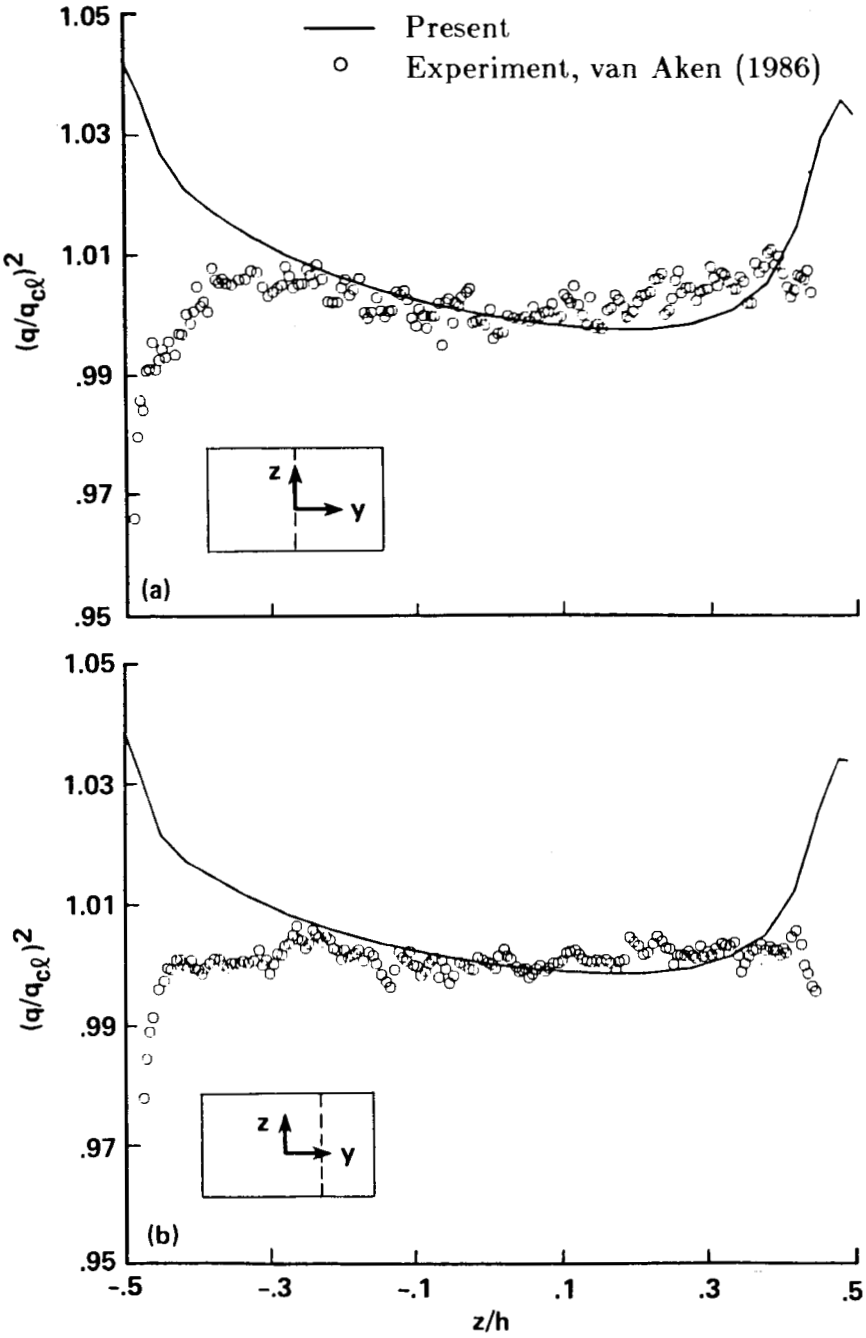

Figure 13. Variation of dynamic pressure with height in the test section at different span positions: a) $y/w = 0.0$; b) $y/w = 0.229$

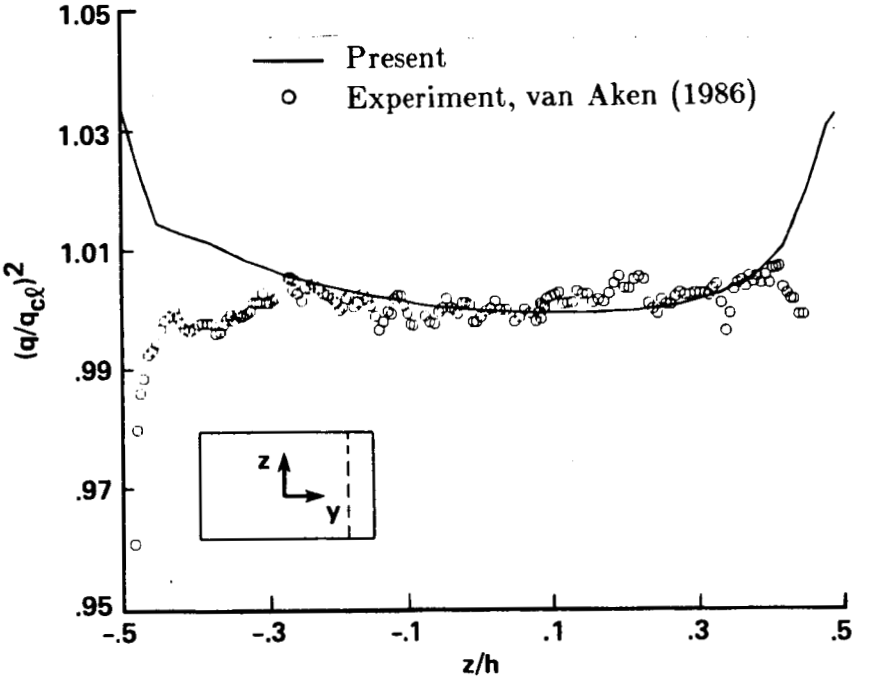

Figure 14. Variation of dynamic pressure with height in the test section at $y/w = 0.375$

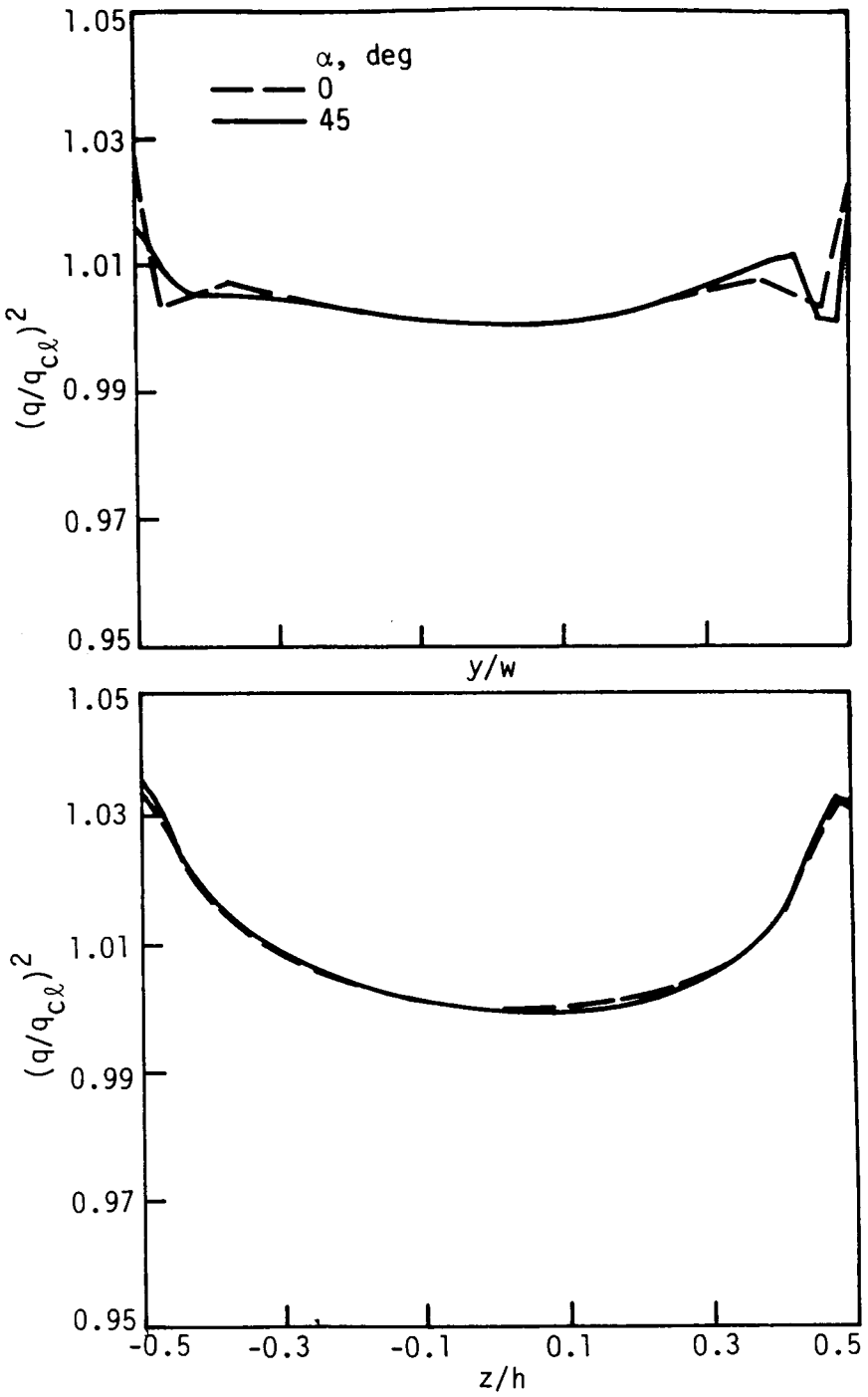

Figure 15. Effect of wind direction on dynamic pressure in the test section. a) Spanwise variation of dynamic pressure at mid-height; b) Variation of dynamic pressure along height at mid-span

external flow conditions. This has been confirmed experimentally though quantitative data are not available for comparison. Figure 16 shows the velocity vectors in the horizontal and vertical planes at midspan and midheight, respectively, for the case in which the wind is at an angle of 45°.

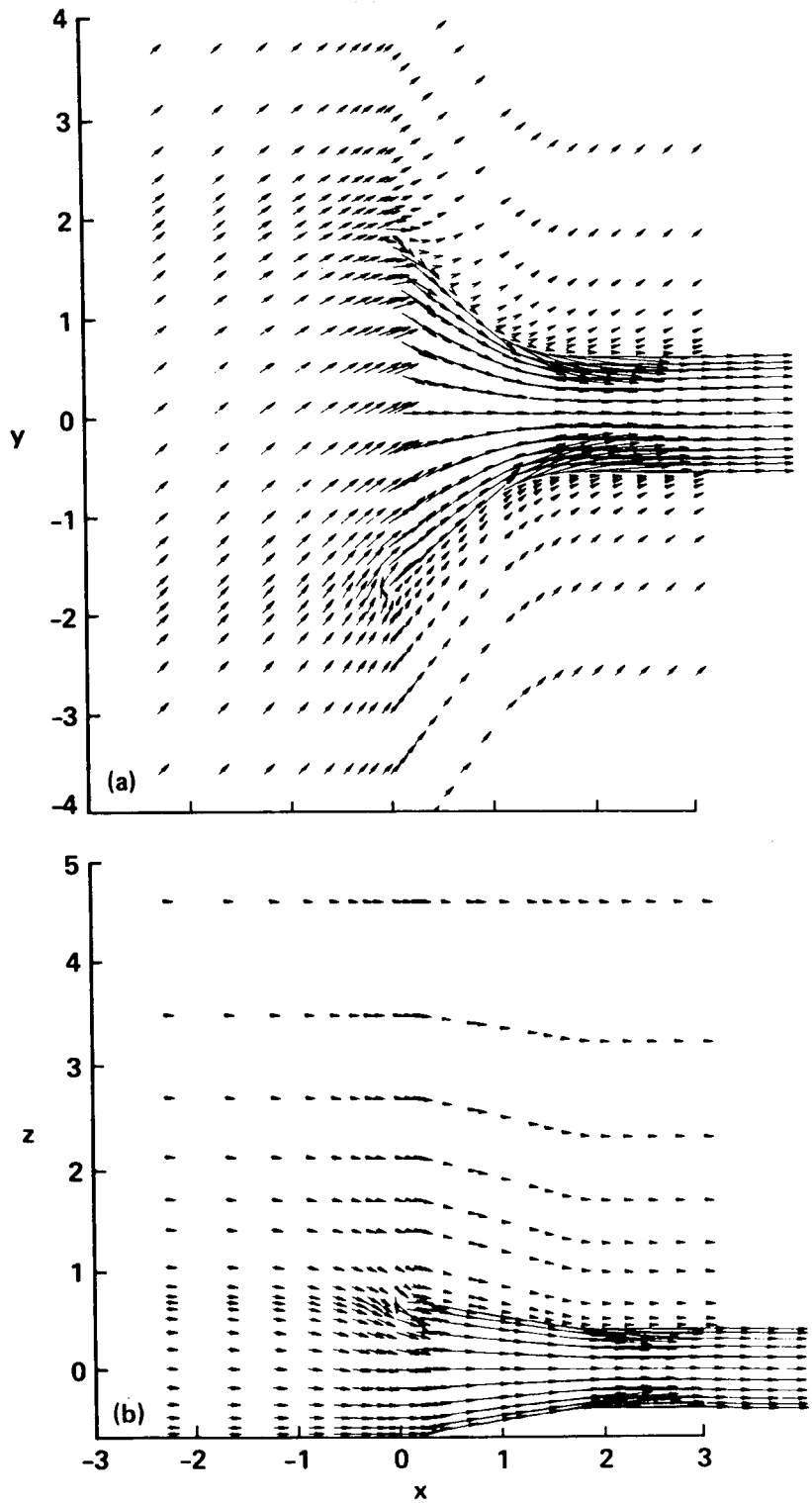

Figure 16. Plot of velocity vectors for wind blowing at 45°. a) Velocity vectors at mid-height; b) Velocity vectors at mid-span

IV. EVALUATION OF A DUAL POTENTIAL - BOUNDARY LAYER INTERACTION SCHEME

The dual potential decomposition scheme was applied to compute inviscid irrotational and rotational flows in Chapter III. It is possible to use the same formulation to compute viscous flows by additionally solving equation (2.47) for the transport of vorticity. Most numerical techniques for equations of this type are notoriously inefficient because of the multiple length scale phenomena that arise in high Reynolds number viscous flows. With the dual potential formulation presented earlier, it might be possible to take advantage of the speed and efficiency of boundary-layer algorithms to compute the vorticity - which can be used to determine the velocity field by solving the Poisson equations for the vector potential functions. The validity of such an interaction scheme for separated flow is examined in a preliminary way by computing the flow over a two-dimensional configuration which has been studied by others using conventional viscous-inviscid interaction schemes. The present dual potential interaction scheme is also applied to compute the attached flow over a three-dimensional trough configuration. These three-dimensional results are compared with other numerical data.

The three-dimensional boundary-layer equations are presented in §IV.A. A reduced version of the dual potential formulation for two-dimensional viscous flows is also presented in this section for convenience. The interaction scheme between the dual potential and boundary-layer equations is discussed in §IV.B. Applications of the present interaction scheme to two- and three-dimensional trough configurations are presented in §IV.C and §IV.D respectively.

All the calculations presented in this chapter were made with the flow assumed to be incompressible (density was assumed to be constant).

A. Governing Equations for Viscous Flow

1. Three-dimensional boundary-layer equations

The boundary-layer equations are derived from the Navier-Stokes equations using an order of magnitude analysis (Schlicting, 1979). The basic assumption in deriving the boundary-layer equations is Prandtl's hypothesis that for sufficiently large Reynolds numbers, there is a thin layer adjacent to the wall where viscous effects are at least as important as inertial effects. It is found from an order of magnitude analysis that viscous diffusion terms in the streamwise direction are negligible. Further, it is found that pressure variations in the normal direction are negligible and the normal momentum equation need not be solved. To distinguish the boundary-layer variables from the dual potential ones, boundary-layer variables are indicated with bars ($\bar{}$). In a regular Cartesian coordinate system, the boundary layer equations for steady, incompressible laminar flow are (Anderson et al., 1984):

continuity:

$$\bar{u}_{\bar{x}} + \bar{v}_{\bar{y}} + \bar{w}_{\bar{z}} = 0 \tag{4.1}$$

streamwise, $\bar{x}$-momentum:

$$\bar{\rho}(\bar{u}\bar{u}_{\bar{x}} + \bar{v}\bar{u}_{\bar{y}} + \bar{w}\bar{u}_{\bar{z}}) = -\bar{p}_{\bar{x}} + \bar{u}_{\bar{z}\bar{z}} \tag{4.2}$$

cross-flow, $\bar{y}$-momentum:

$$\bar{\rho}(\bar{u}\bar{v}_{\bar{x}} + \bar{v}\bar{v}_{\bar{y}} + \bar{w}\bar{v}_{\bar{z}}) = -\bar{p}_{\bar{y}} + \bar{v}_{\bar{z}\bar{z}} \tag{4.3}$$

In these equations, the variables are nondimensionalized by free stream values as indicated in Chapter II. Also, the normal coordinate $\bar{z}$ and the corresponding velocity component $\bar{w}$ are scaled by the square root of the free-stream Reynolds number

Re so that they may have the same magnitude as the streamwise components (for laminar flow).

a. Boundary conditions At a solid wall boundary, the no-slip boundary condition was applied:

$$\bar{u}(\bar{x},\bar{y},0) = \bar{v}(\bar{x},\bar{y},0) = \bar{w}(\bar{x},\bar{y},0) = 0 \tag{4.4}$$

If no streamwise separation is present, these equations can be solved with pressure specified as the forcing function (the direct mode), where the pressure is calculated from the inviscid flow variables. Near and in reversed-flow regions, the boundary-layer equations are solved in the inverse mode to avoid saddle-point behavior at the separation point. To solve the momentum equations in the inverse mode, the boundary conditions are modified so that inverse forcing functions can be specified. In conventional viscous-inviscid interaction approaches, the inviscid flow is computed over a equivalent body rather than the actual body surface, that is, viscous effects are assumed to have the effect of altering the effective body surface by an amount equal to the displacement thickness and it is perhaps convenient to specify the displacement thickness as the inverse forcing function (cf Carter and Wornum, 1975; Kwon and Pletcher, 1978; Lee and Pletcher, 1986). However, following the work of Klineberg and Steger (1974), and Van Dalsem and Steger (1983), the wall shear stress is specified as the inverse forcing function in this study. The inverse forcing function is specified in the solution scheme by replacing the direct forcing functions (pressure terms) with expressions containing the inverse forcing functions. In the present procedure, these relations were obtained by evaluating the momentum equations at the wall. For example, the $\bar{x}$-momentum equation evaluated at the wall gives

$$\bar{p}_{\bar{x}} = \bar{u}_{\bar{z}\bar{z}} \tag{4.5}$$

A Taylor series expansion about a point at the wall gives

$$\bar{u}_2 = \bar{u}_1 + \bar{u}_{\bar{z}}(\bar{z}_2 - \bar{z}_1) + \frac{1}{2}\bar{u}_{\bar{z}\bar{z}}(\bar{z}_2 - \bar{z}_1)^2 + \text{higher order terms} \qquad (4.6)$$

Defining the nondimensional shear stress at the wall as

$$\tau_{wx} = \bar{u}_{\bar{z}}\, w \qquad (4.7)$$

and making use of equations (4.5) - (4.6) gives the following relationship between the pressure gradient and the component of wall shear stress in the $\bar{x}$-direction:

$$\bar{p}_{\bar{x}} = \frac{2\left[\frac{\bar{u}_2 - \bar{u}_1}{\bar{z}_2 - \bar{z}_1} - \tau_{wx}\right]}{\bar{z}_2 - \bar{z}_1} \qquad (4.8)$$

In this work, the wall shear stress (τ_{wx}) was used as the inverse boundary condition, and the inverse method was used in only the $\bar{x}$-momentum equation, with the $\bar{y}$-momentum equation solved in the direct mode. The inverse method can be used even for attached flows, though it was used mainly in the separated flow regions in this study.

The boundary-layer equations shown above were solved using the relaxation method given by Van Dalsem and Steger (1985). The numerical algorithm is written to solve the equations in a transformed domain which is a uniformly spaced, rectangular coordinate region, using upwind differencing in the streamwise and spanwise directions, and central differencing in the normal direction. Details of the transformation and the numerical schemes used can be obtained from Van Dalsem and Steger (1985).

In analyzing three-dimensional boundary-layer solutions, it is useful to define some dimensionless parameters such as the wall shear stress components τ_{wx}, τ_{wy};

and integral thicknesses δ_x, δ_y as

$$\begin{aligned} \tau_{wx} &= \frac{\partial \bar{u}}{\partial \bar{z}}|_w \\ \tau_{wy} &= \frac{\partial \bar{v}}{\partial \bar{z}}|_w \\ \delta_x &= \int_0^\infty \left(1 - \frac{\bar{u}}{\bar{u}_e}\right) d\bar{z} \\ \delta_y &= \int_0^\infty \left(\frac{\bar{v}_e - \bar{v}}{\bar{u}_e}\right) d\bar{z} \end{aligned} \tag{4.9}$$

in which the subscript e refers to values at the edge of the boundary layer. Note that in these definitions, the normal coordinate $\bar{z}$ is scaled by $Re^{\frac{1}{2}}$.

Unlike two-dimensional flows, the integral thickness δ_x is not the correct measure of the displacement effect of a three-dimensional boundary layer. For three-dimensional flows, Moore (1953) showed that the displacement thickness δ^* has to account for cross-flow effects. He derived a partial differential equation for the displacement thickness, which, in terms of the integral thicknesses defined in equation (4.9), is given as

$$\frac{\partial}{\partial \bar{x}}\left[\bar{u}_e(\delta^* - \delta_x)\right] + \frac{\partial}{\partial \bar{y}}(\bar{v}_e\delta^* - \bar{u}_e\delta_y) = 0 \tag{4.10}$$

From a known solution of the boundary-layer variables, it is relatively easy to numerically solve the partial differential equation given by equation (4.10) and obtain the displacement thickness. For the geometries considered in this study, the flow was assumed to be two-dimensional at the inflow boundary, and hence, $\delta^* = \delta_x$ there. With known values of $\bar{u}_e$, $\bar{v}_e$, δ_x, and δ_y, an integration algorithm similar to that used for integrating the vorticity in §II.E.3 was used to obtain the displacement thickness.

2. Two-dimensional dual potential equations

It is, of course, possible to use the three-dimensional formulation to compute two-dimensional flows. However, it is more convenient to present the dual potential equations for the two-dimensional case separately.

a. Governing equations To retain the terminology used earlier, the normal coordinate is denoted as z instead of the traditional y. With this convention, the governing Navier-Stokes equations for steady, incompressible, laminar two-dimensional flow are:

Continuity:

$$u_x + w_z = 0 \tag{4.11}$$

x-momentum:

$$\rho(uu_x + wu_z) = -p_x + \frac{1}{Re}(u_{xx} + u_{zz}) \tag{4.12}$$

z-momentum:

$$\rho(uw_x + ww_z) = -p_z + \frac{1}{Re}(w_{xx} + w_{zz}) \tag{4.13}$$

Using the dual potential decomposition defined in terms of the scalar potential function ϕ and the stream function χ as

$$\begin{aligned} u &= \phi_x - \chi_z \\ w &= \phi_z + \chi_x \end{aligned} \tag{4.14}$$

the continuity equation is written as

$$\nabla^2\phi = 0 \tag{4.15}$$

and with the vorticity defined as

$$\omega = u_z - w_x \tag{4.16}$$

the stream function equation is

$$\nabla^2 \chi = -\omega \tag{4.17}$$

The momentum equations are written in terms of the vorticity as

$$\rho(u\omega_x + w\omega_z) = \frac{1}{Re}(\omega_{xx} + \omega_{zz}) \tag{4.18}$$

Note the absence of the vorticity stretching terms in the two-dimensional vorticity transport equation.

b. Boundary conditions Boundary conditions at any boundary surface are no-slip and tangency, that is,

$$u = v = 0 \tag{4.19}$$

No-slip is enforced implicitly by evaluating the vorticity at the wall appropriately. Tangency is enforced by selecting the stream function to be a constant along the surface and computing ϕ appropriately.

$$\psi = \text{constant}; \quad \vec{n} \cdot \nabla\phi = 0 \tag{4.20}$$

As in the three-dimensional case, vorticity for the interaction scheme was obtained from a boundary-layer solution. The algorithm used to solve the boundary-layer equations was a two-dimensional version of that used for the three-dimensional case (Van Dalsem and Steger, 1985) and is described in Appendix B.

B. Dual Potential - Boundary Layer Interaction Scheme

As mentioned earlier, the present interaction scheme involves obtaining the vorticity from the boundary-layer equations. To solve the boundary-layer equations, it is necessary to determine the pressure from the dual potential solution. A schematic

view of this coupling method is given in Figure 17. Such an interaction scheme was proposed and implemented for two-dimensional flows by Steger and Van Dalsem (1985).

1. Solution strategy for the interaction scheme

An iterative solution strategy, similar to the one used for inviscid flows is used for the dual potential - boundary-layer interaction scheme and is described below.

At each grid point an initial guess is made for values of $\phi, \vartheta, \chi, \psi$, and for ω_1, ω_2, and ω_3. The following iteration scheme is then implemented:

1) Vector potential functions, ϑ, χ, ψ. Individually update ϑ, χ, and ψ from the Poisson equations given by equation (2.45) for assumed values of ω_1, ω_2, and ω_3. Boundary conditions for these equations are again kept compatible with the consistency relation, equation (2.50).

2) Scalar potential function, ϕ. Update ϕ from the continuity equation (2.44) using the ADI-like algorithm for the transonic full potential function and previously updated values of ϑ, χ, and ψ.

3) Pressure, p. With the velocity components known, pressure is calculated by integrating the normal momentum equation from the far field (uniform flow, $p = p_\infty$) to the wall. The numerical scheme employed is similar to the one described in §II.E.3 for integrating the vorticity consistency equation.

4) Vorticities, ω_1, ω_2, and ω_3. With pressure known, the vorticity components are evaluated from the solution of the three-dimensional boundary-layer equations

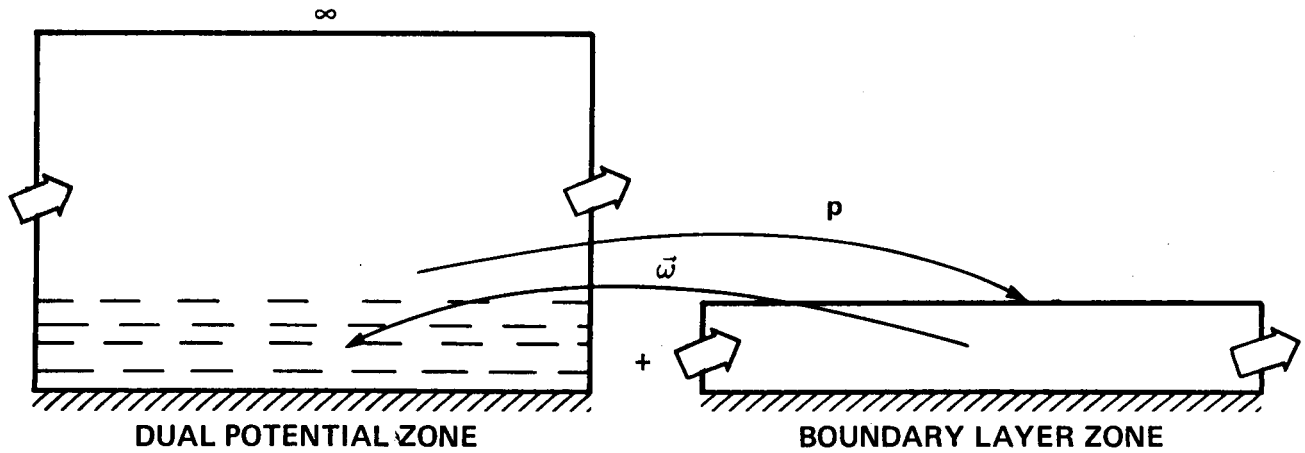

Figure 17. Schematic view of coupling method between the dual potential and boundary layer zones

as

$$\omega_1 = -\bar{v}_{\bar{z}}\, Re^{\frac{1}{2}}$$

$$\omega_2 = \bar{u}_{\bar{z}}\, Re^{\frac{1}{2}} \tag{4.21}$$

$$\omega_3 = \bar{v}_{\bar{x}} - \bar{u}_{\bar{y}}$$

Note that the bars on the variables at the right hand side of equation (4.21) refer to boundary-layer quantities. Also, in accordance with the boundary-layer assumption, the contribution of the normal velocity is neglected in evaluating ω_1 and ω_2. Furthermore, the scale factor $Re^{\frac{1}{2}}$ appears on the right-hand-side of equation (4.21) since the normal coordinate $\bar{z}$ is scaled by this quantity in the boundary-layer equations.

5) Test for convergence and, if necessary, return to (1).

The numerical algorithm used to integrate the normal momentum equation is described below.

2. Integration scheme for pressure

In the dual potential - boundary layer interaction procedure described above, the boundary-layer equations require the knowledge of pressure from the dual potential solution. However, pressure is not a dependent variable in the dual potential formulation and a method for calculating the pressure from the dual potential solution needs to be devised. If the flow above the boundary-layer is irrotational, it is, in principle, possible to determine the edge of the boundary-layer (defined as the first location in the normal direction $\bar{z}$ where $\frac{\bar{u}}{\bar{u}_e} \geq \epsilon$; $\epsilon = 0.9995$ in this study) and evaluate the pressure from Bernoulli's equation applied to the dual potential solution at this height. However, this procedure was found to be inaccurate for various reasons. In particular, in regions of separated flow, there is considerable growth of the boundary-layer and the normal pressure gradient in this region is not necessarily

small in the dual potential solution and it was found necessary to use an alternative method to determine the pressure. Furthermore, with the stretched grids used in the calculations, some form of interpolation may be required in determining the edge of the boundary layer. Using the normal momentum equation appears to give a reasonable estimate of the pressure near the wall from the dual potential solution for the geometries and flow conditions considered in this study. With the use of the normal momentum equation, interpolation is avoided, and it is also possible to compute the pressure for the case in which the outer flow is rotational.

With z assumed to be in roughly the normal direction to the surface and neglecting viscous terms, the z-momentum equation (2.2) is written as

$$\rho(uw_x + vw_y + ww_z) = -p_z \tag{4.22}$$

In transformed coordinates, this equation becomes

$$\xi_z p_\xi + \eta_z p_\eta + \zeta_z p_\zeta = -\rho(Uw_\xi + Vw_\eta + Ww_\zeta) \tag{4.23}$$

This equation has the same form as equation (2.71) where $f = p$, $a_1 = \xi_z$, $a_2 = \eta_z$, $a_3 = \zeta_z$, and a_4 is the right hand side of equation (4.23). With the pressure known in the far field, that is, at $l = LMAX$, $p = p_\infty$, equation (4.23) can be integrated in the $-\zeta$-direction to obtain the wall pressure using algorithms similar to that given by equations (2.73) - (2.74). First-order backward differencing is used at the first ζ = constant plane, and second-order differencing at all subsequent planes.

3. Interaction scheme for separated flow

For attached flows, the solution strategy given above is easy and straightforward to implement. For separated flow, it is not possible to use pressure as the forcing

function, and a way of calculating or updating the shear stress needs to be devised. Van Dalsem and Steger (1985) found the following scheme to be fast and reliable for updating the shear stress:

$$\tau_{wx}^{n+1} = \tau_{wx}^{n} + \omega(\bar{p}^{n} - p_{w}^{n+1}) \tag{4.24}$$

and used a value of the relaxation parameter $\omega \approx 10$. In equation (4.24), p_w refers to the pressure at the wall which is obtained from the dual potential solution by integrating the normal momentum equation. Thus, they updated the shear stress from the difference between the viscous and the inviscid pressures at the wall. The viscous pressure $\bar{p}$ was obtained by using Bernoulli's equation at the edge of the boundary layer as

$$\bar{p} = \frac{\rho}{2}[1 - (\bar{u}_e^2 + \bar{v}_e^2)] \tag{4.25}$$

From equation (4.8), it can be seen that there is a direct relation between the shear stress and the pressure gradient. In an iterative solution method, this relation can be used to devise a new scheme to update the shear stress. Equation (4.8) can be rewritten as

$$r^{n} = \frac{\bar{z}_2 - \bar{z}_1}{2} p_x^{n+1} - \frac{\bar{u}_2^{n+1} - \bar{u}_1^{n+1}}{\bar{z}_2 - \bar{z}_1} + \tau_{wx}^{n+1} \tag{4.26}$$

When the interaction scheme between the dual potential and the boundary-layer formulation converges, the residual term r_n on the right-hand-side of equation (4.26) should be zero. Hence, a formula for updating the shear stress can be formed as

$$\tau_{wx}^{n+1} = \tau_{wx}^{n} - \omega r^{n} \tag{4.27}$$

where ω is a relaxation parameter. Note that the scheme for updating the shear stress at the wall given by equation (4.26) - (4.27) does not require the assumption of irrotationality at the edge of the boundary-layer. In fact, it does not require

any assumptions or values of variables at the edge of the boundary-layer provided the pressure gradient from the dual potential formulation can be obtained without the knowledge of any edge values. This is possible when the normal momentum equation is used to obtain the pressure from the dual potential solution.

C. Flow Over a Two-Dimensional Trough

The dual potential - boundary layer interaction procedure described above was used to compute the flow over a two-dimensional trough which was first studied by Carter and Wornum (1975), and subsequently by Kwon and Pletcher (1981), Veldman (1981) and Edwards and Carter (1985). The algorithm used to solve the boundary-layer equations was a two-dimensional version of the three-dimensional one given by Van Dalsem and Steger (1985) and is given in Appendix B. The boundary layer algorithm has been validated for a number of two- and three-dimensional flows by Van Dalsem and Steger (1985, 1986a). In the present study, the boundary-layer code was again verified by computing flow over a flat plate, both in the direct and inverse modes. In all cases, the agreement with known analytical/numerical results was good. The dual potential procedure was verified in Chapter III for inviscid flows. Details of the numerical algorithms for the two-dimensional case are given in Appendix B. The dual potential - boundary layer interaction procedure was verified by computing the flow over a flat plate and a detailed description of these results will not be presented here.

1. Geometry and grid

The geometry considered here is shown in Figure 18. It consists of a flat plate with a trough located at some distance from the sharp leading edge. The surface

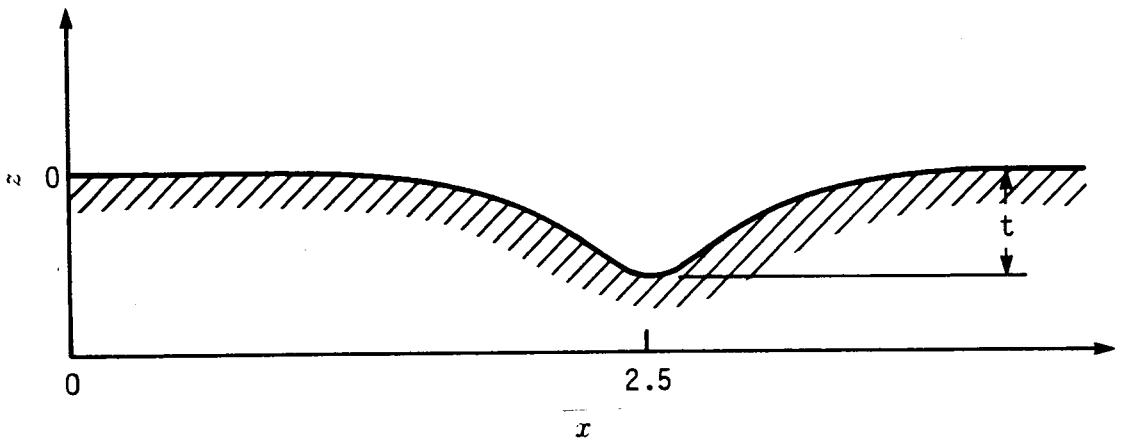

Figure 18. Geometry of the two-dimensional trough

of this geometry is described by the function

$$z(x) = -t\,\mathrm{sech}(4x - 10) \tag{4.28}$$

The reference length for this configuration is $L = 1\,m$. The free stream Reynolds number based on the reference length is 80,000. In the present calculations, the inflow and outflow boundaries for the dual potential set of equations were set to $x = -2.5$ and $x = 7.5$, respectively and the outer boundary was set at $z = 5$ with a mesh of 219×81 grid points in the x and z directions, respectively. Clustering functions given by Vinokur (1983) were used in order to cluster points in the streamwise direction at the location corresponding to the maximum depth of the trough, that is, $x = 2.5$. A stretching function was used in the normal direction to obtain a fine grid in the vicinity of the wall, with the minimum spacing at the wall set to 0.0001. The grid used to obtain the dual potential solution is shown in Figure 19. The interaction region extended from $x = 1.0$ to $x = 4.0$ which correspond to 121 points in the streamwise direction. The boundary-layer grid extended up to a distance of $\bar{z} = 0.2$ with 55 points in the normal direction. The same distribution of points in the normal direction as in the dual potential grid was used, hence the need for interpolating the vorticity was avoided. For the boundary-layer, a Falkner-Skan solution for zero pressure gradient scaled to the appropriate location in the $\bar{x}$-direction (in this case, $\bar{x} = 1.0$ from the leading edge of a flat plate) was used as the inflow boundary condition.

Once again, body fitted curvilinear coordinates were employed, and the flow domain mapped to a uniformly spaced rectangular coordinate region. The details of these transformations are very similar to that given for the three-dimensional transformation used in Chapter II and are given in Appendix B.

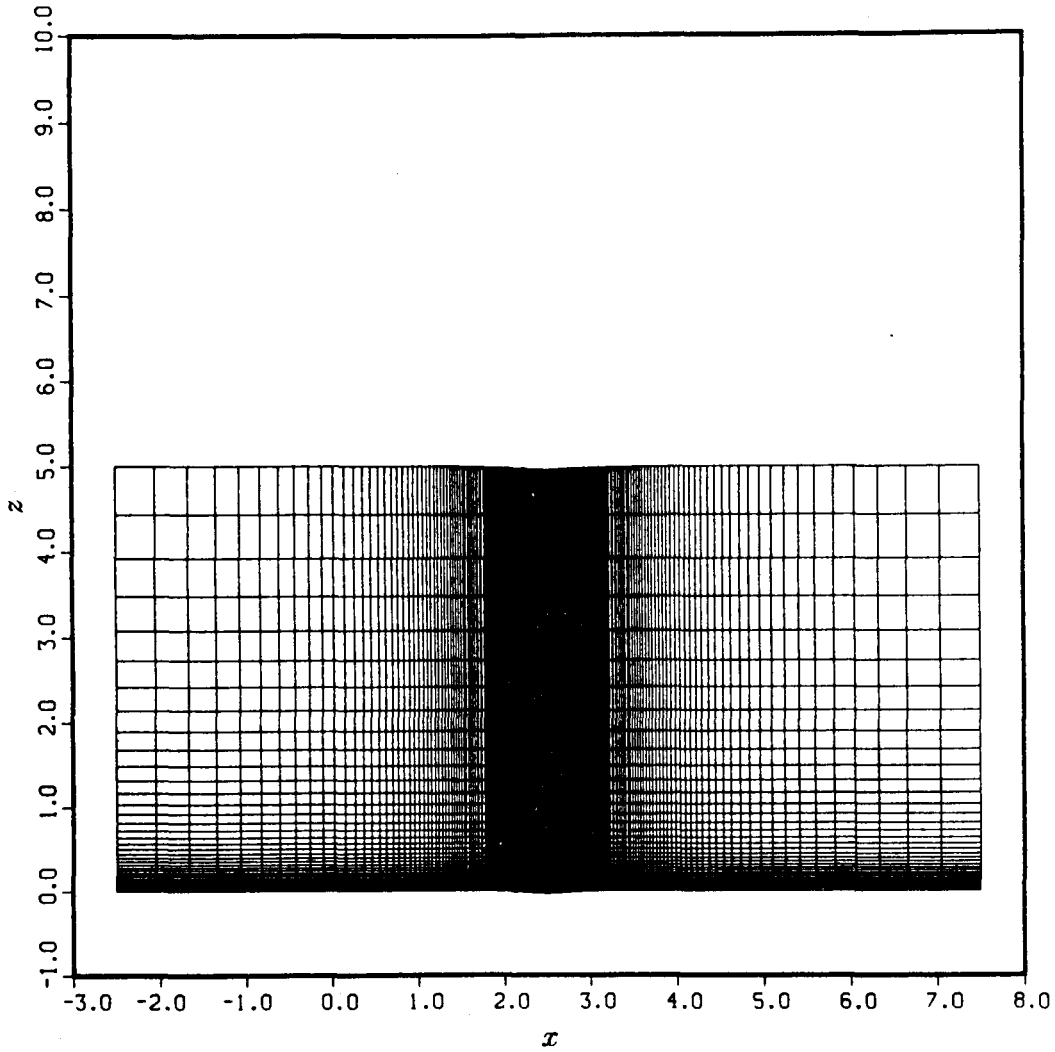

Figure 19. View of grid for the two-dimensional trough, $t = 0.03$

2. Results and discussion

To verify the boundary-layer code for separated flow, solutions were obtained from the code separately with the inverse forcing function specified. The shear stress distribution used as the inverse forcing function was obtained from the results of Davis et al. (1986) who used the vorticity/stream-function formulation to solve the Navier-Stokes equations. Figure 20 is a plot of the wall shear stress τ_{wx} which was prescribed for this case. Figure 21 show comparisons of the pressure $\bar{p} = \frac{1}{2}(1 - \bar{u}_e^2)$ where $\bar{u}_e$ is the velocity at the edge of the boundary layer, with the results of Veldman (1981) who studied the same configuration using a quasi-simultaneous viscous-inviscid interaction procedure. The present results are compared with those of Veldman because Davis et al. (1986) did not present values of the pressure in their report. The figure shows good agreement between the present boundary-layer results and that of Veldman. Convergence was obtained in about 100 iterations requiring 20 seconds on a CRAY XMP computer.

Attempts to compute the same flow with the dual potential - boundary layer interaction procedure failed, however, as it was not possible to obtain a converged solution.

In order to examine the reason for this failure, the vorticity was computed from the converged boundary-layer solution (for a specified wall shear stress distribution) and used to obtain a converged dual potential solution. Results for this case are presented in Figure 22 which is a plot of the streamwise variation of the pressure. The pressure from the dual potential solution was calculated by integrating the z-momentum equation from the far-field down to the vicinity of the wall as described earlier. Figure 22 is a comparison of the pressure between the dual potential solution and the result of Veldman (1981) for this case. It can be seen that there is

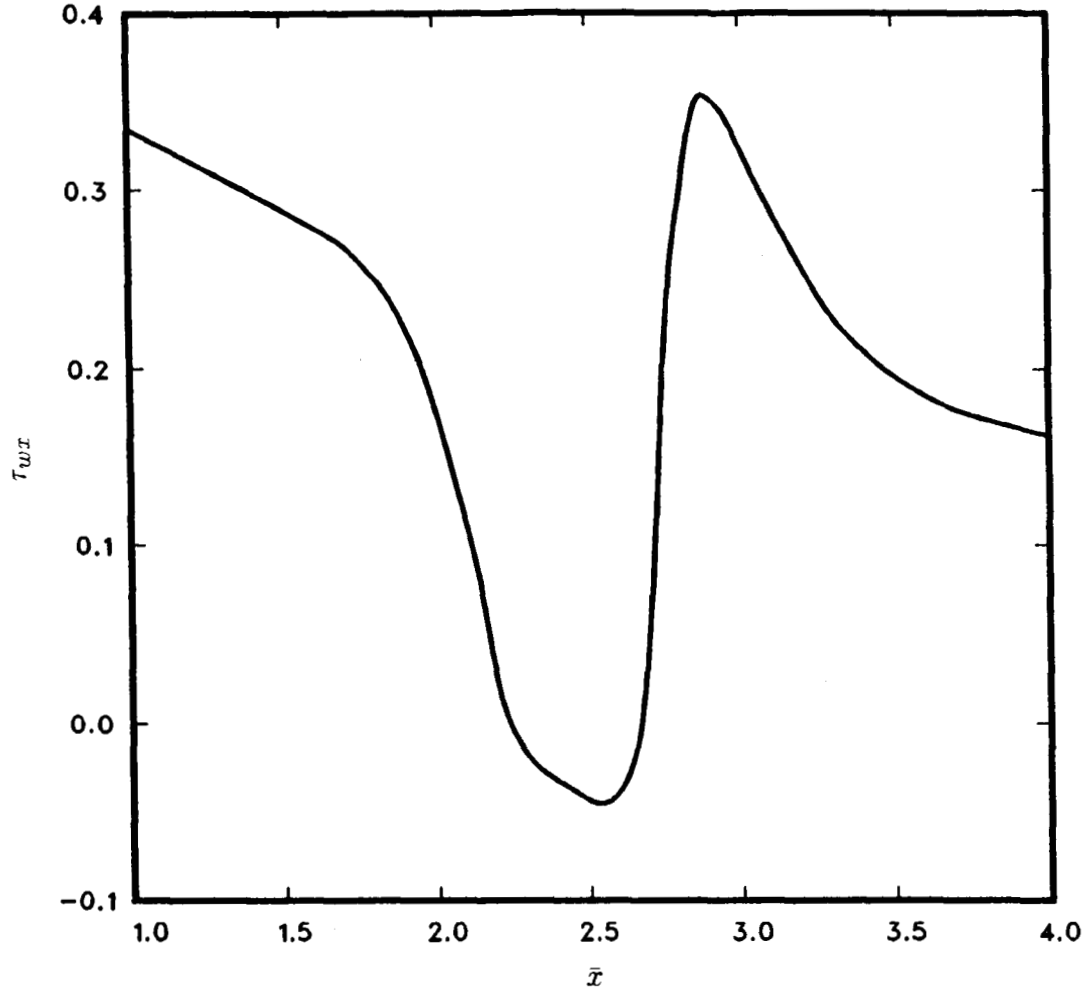

Figure 20. Dimensionless wall shear stress distribution for the two-dimensional trough, $t = 0.03$, from Davis et al. (1986)

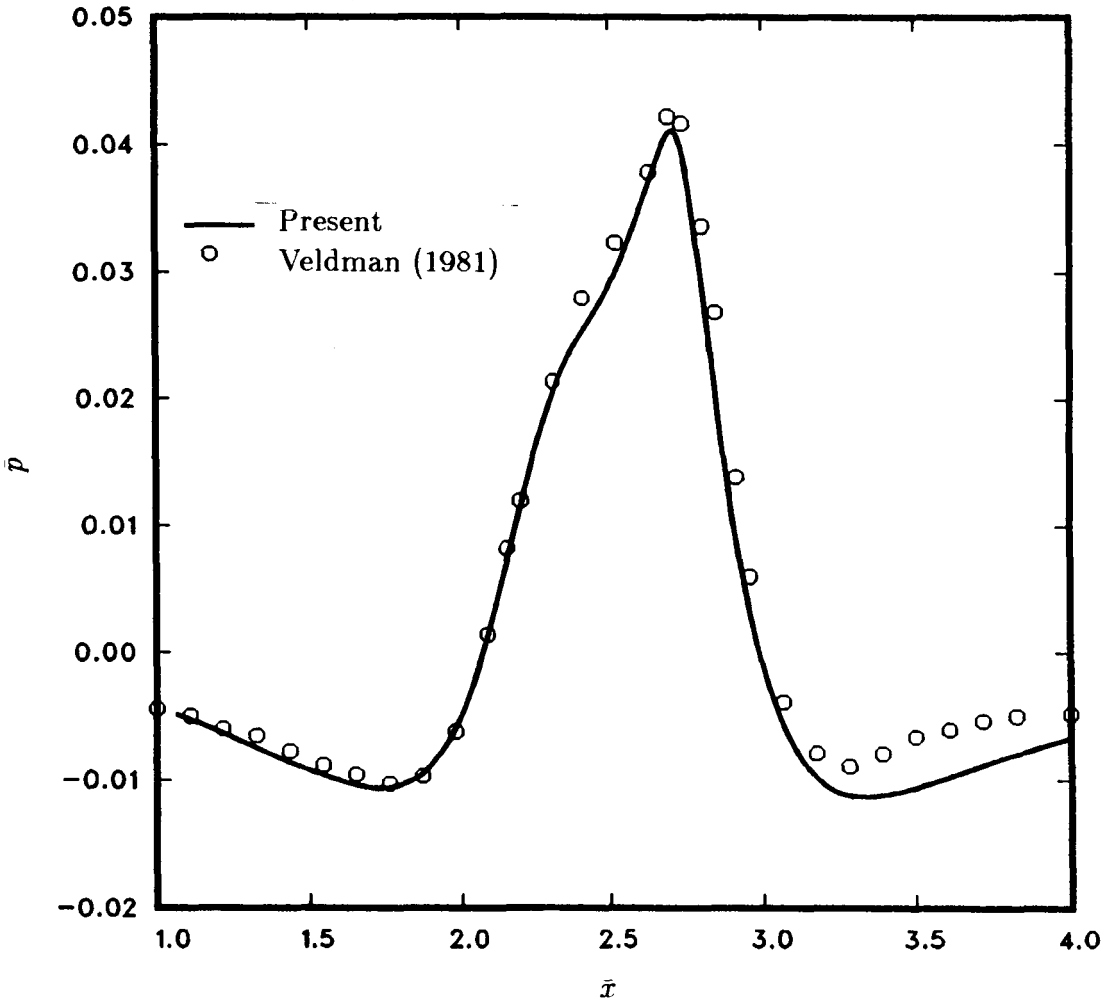

Figure 21. Pressure distribution for the two-dimensional trough from the boundary-layer solution for a specified wall shear stress distribution, $t = 0.03$

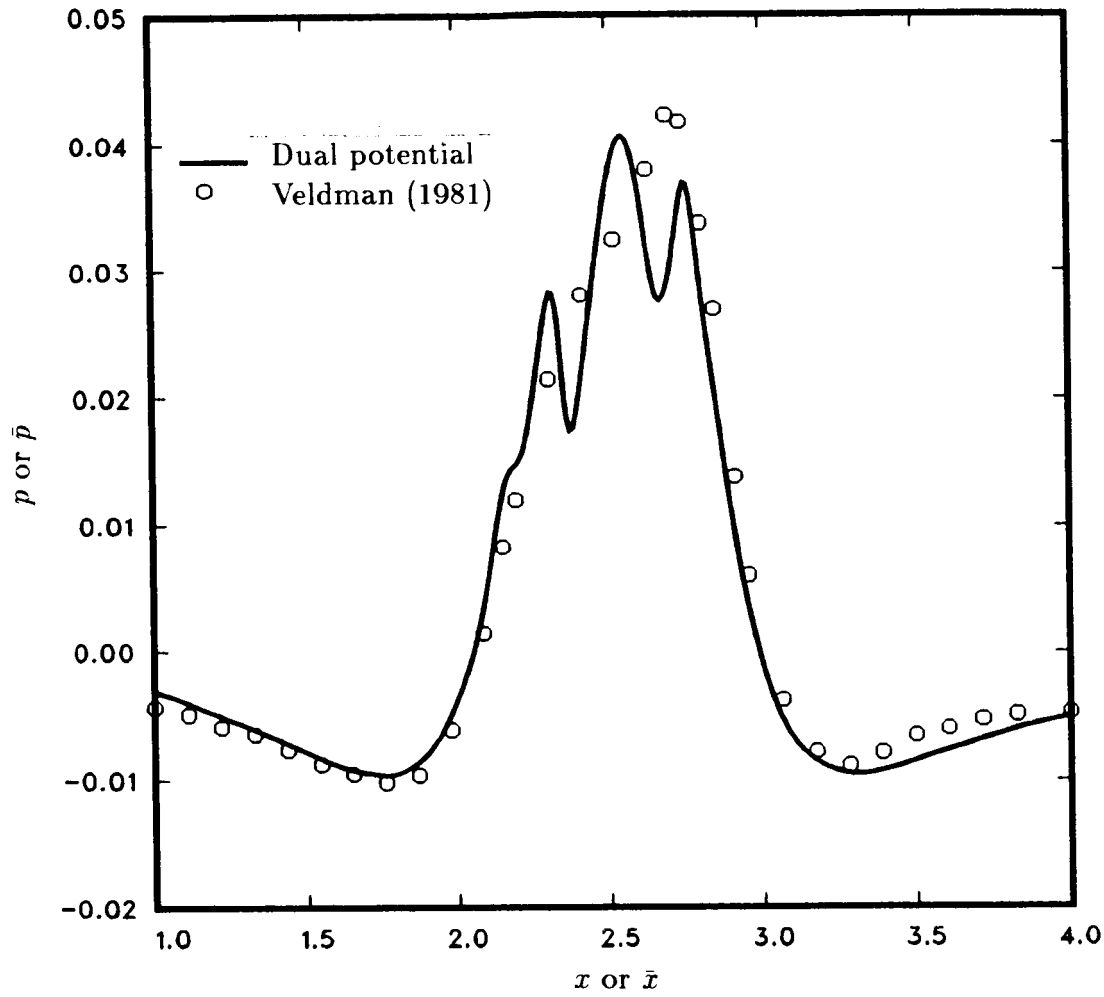

Figure 22. Pressure distribution for the two-dimensional trough from the dual potential solution for specified vorticity field

considerable disagreement between the two curves in the vicinity of the separated flow region. This discrepancy between the two solutions is the apparent reason for being unable to obtain a converged interaction solution for separated flows.

In general, the boundary-layer equations are sensitive to the forcing functions, that is, pressure or wall shear stress (*cf.* Klineberg and Steger, 1974; Lee and Pletcher, 1986). Any error in these functions generates an erroneous vorticity solution which in turn feeds back into the dual potential solution, in this case causing an unstable interaction process.

It should be pointed out that the interaction procedure described in this study is different from the more conventional viscous-inviscid interaction procedures in which boundary layer effects are imposed on the outer flow as a correction to the shape of the body surface. In the current procedure, the dual potential solutions are solved over the entire flow domain including the region where viscous effects are important, and the viscous effects are accounted for by injecting vorticity from the boundary layer equations. Since, in principle, the only approximation made is in using the boundary-layer equations rather than equation (4.18) to provide the vorticity, the issue arises as to whether this vorticity is an accurate input for the governing dual potential equations. To answer this question, the dual potential formulation was modified by obtaining the vorticity directly from the vorticity transport equation (4.18) thus avoiding any boundary-layer assumption. To be consistent with previous data, however, the specified shear stress described earlier was used to prescribe the wall vorticity. Thus, even though the full Navier-Stokes equations are solved for this case, the calculation used as its vorticity boundary condition the previous known solution obtained by other means. The numerical

algorithm for solving equation (4.18) is similar to the one described in §II.E.2 and is given in Appendix B.

In practice, the boundary-layer vorticity was used at the first two points in the normal direction, that is, at $l = 1, 2$, to avoid any of the numerical errors at the walls due to the stretched grids (*cf.* Appendix A). Solutions obtained from the Navier-Stokes formulation for this case are presented in Figure 23, which is a plot of the pressure from the dual potential solution along the length of the trough, compared with the result obtained by Veldman (1981). The agreement between the two pressures is noticeably better from the case where the boundary-layer vorticity was used in the viscous layer (Figure 22). To further study this case, vorticity profiles from the boundary-layer and Navier-Stokes solutions are compared at select locations in the streamwise direction in Figures 24-26. From these figures, it can be seen that there is considerable discrepancy between the two vorticities in the separated flow region.

It should be pointed out that at the flow conditions for this case, namely the moderate Reynolds number and the depth of the trough, the boundary-layer is relatively thick (almost twice the depth of the trough) and there is considerable variation of the pressure gradient in the normal direction. This fact is illustrated in Figure 27 by plotting pressure from the inviscid solution at the wall and at a location corresponding to the edge of the boundary layer for this configuration. Figure 27 shows that there is significant variation of the pressure gradient in the normal direction within the shear region. Hence, the boundary-layer assumption is questionable in such regions and the type of interaction considered here is perhaps not appropriate for this case. A more suitable form of interaction is needed in which the boundary-layer equations are solved in regions very close to the wall (e.g., for the

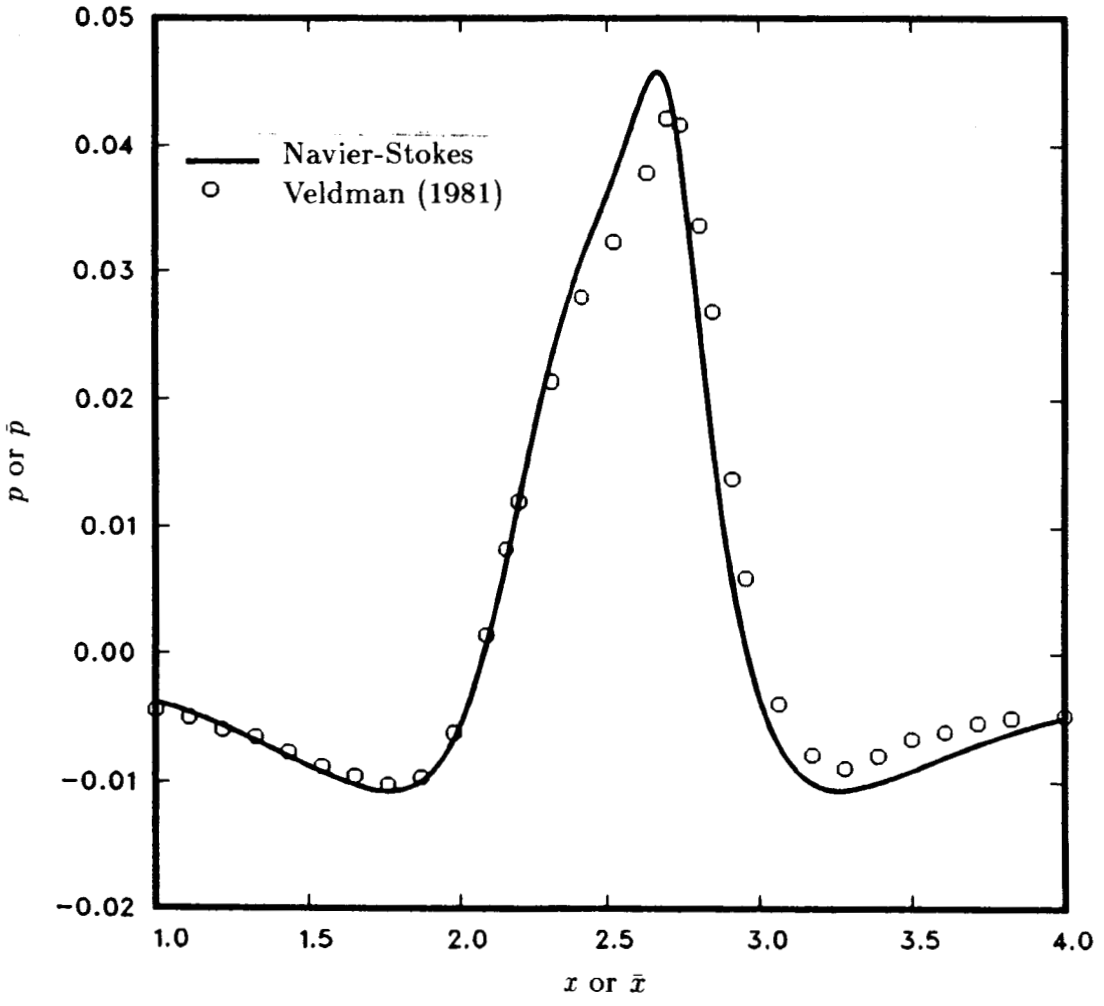

Figure 23. Pressure distribution from the Navier-Stokes solution with vorticity specified at the first two points from the wall, $l = 2$

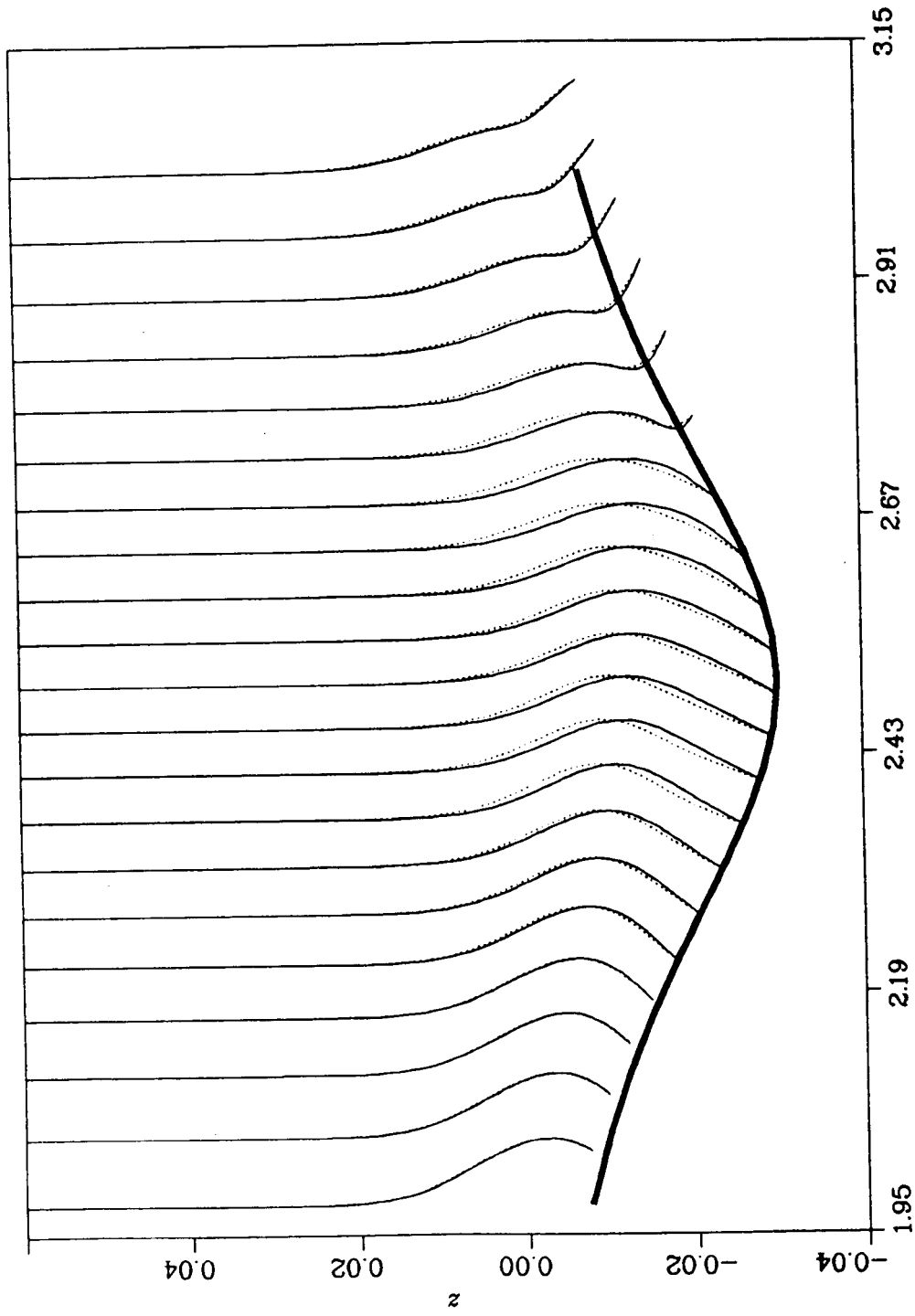

Figure 24. Comparison of vorticity profiles between Navier-Stokes and boundary-layer solutions, ——— Navier-Stokes; ..... boundary-layer

C-2

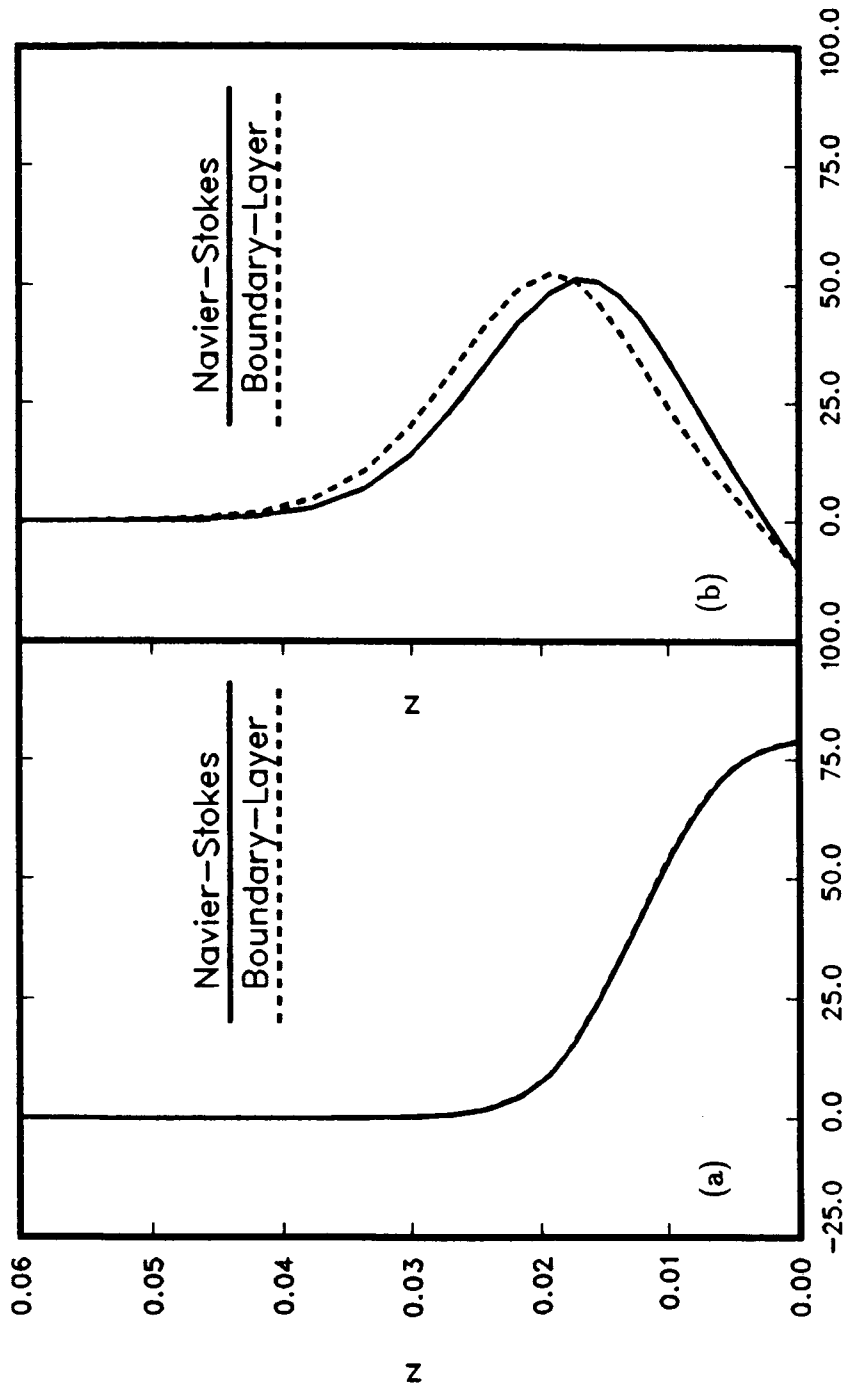

Figure 25. Comparison of vorticity profiles between Navier-Stokes and boundary-layer solutions. a) $x = 1.62$; b) $x = 2.41$

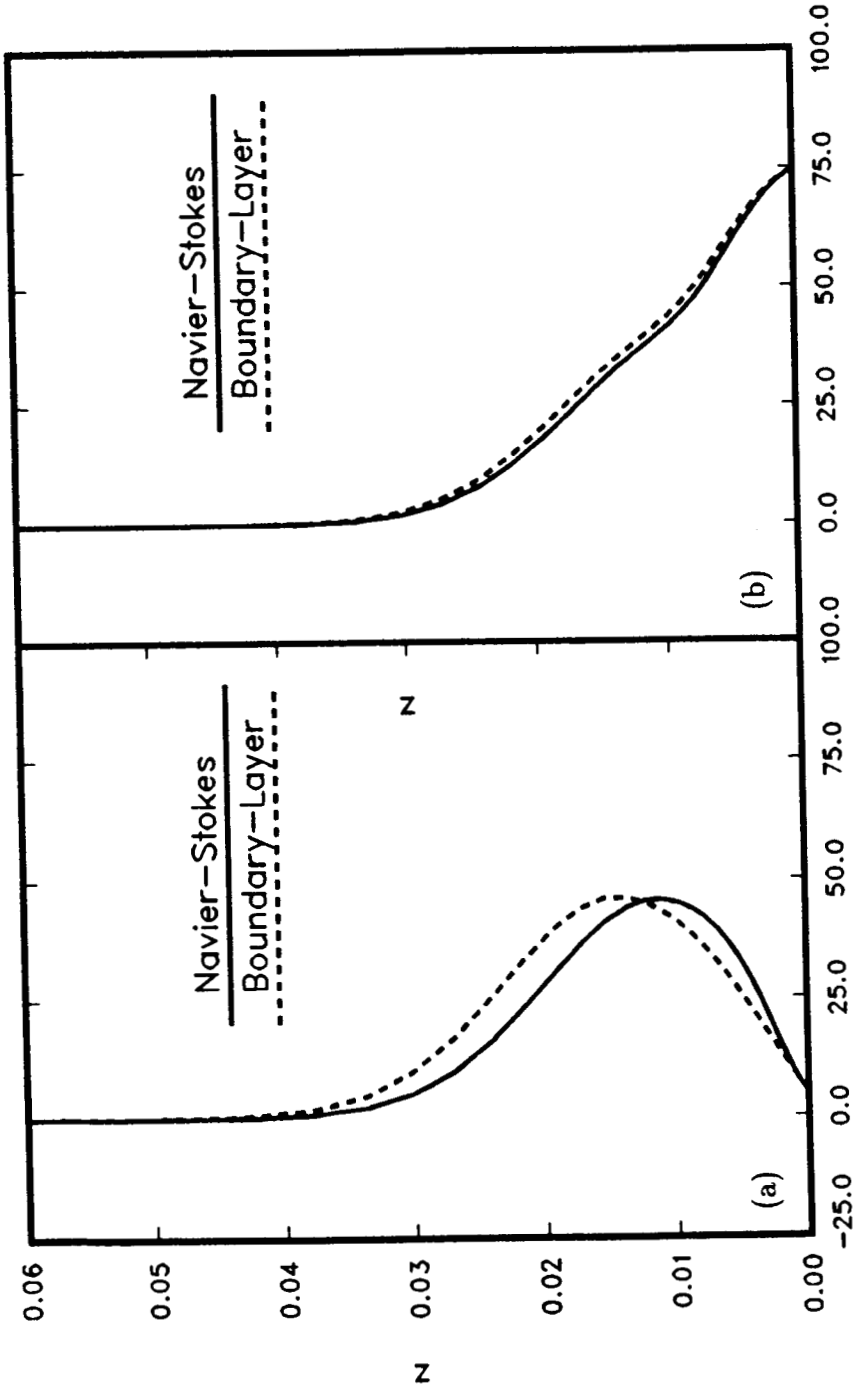

Figure 26. Comparison of vorticity profiles between Navier-Stokes and boundary-layer solutions. a) $x = 2.68$; b) $x = 3.17$

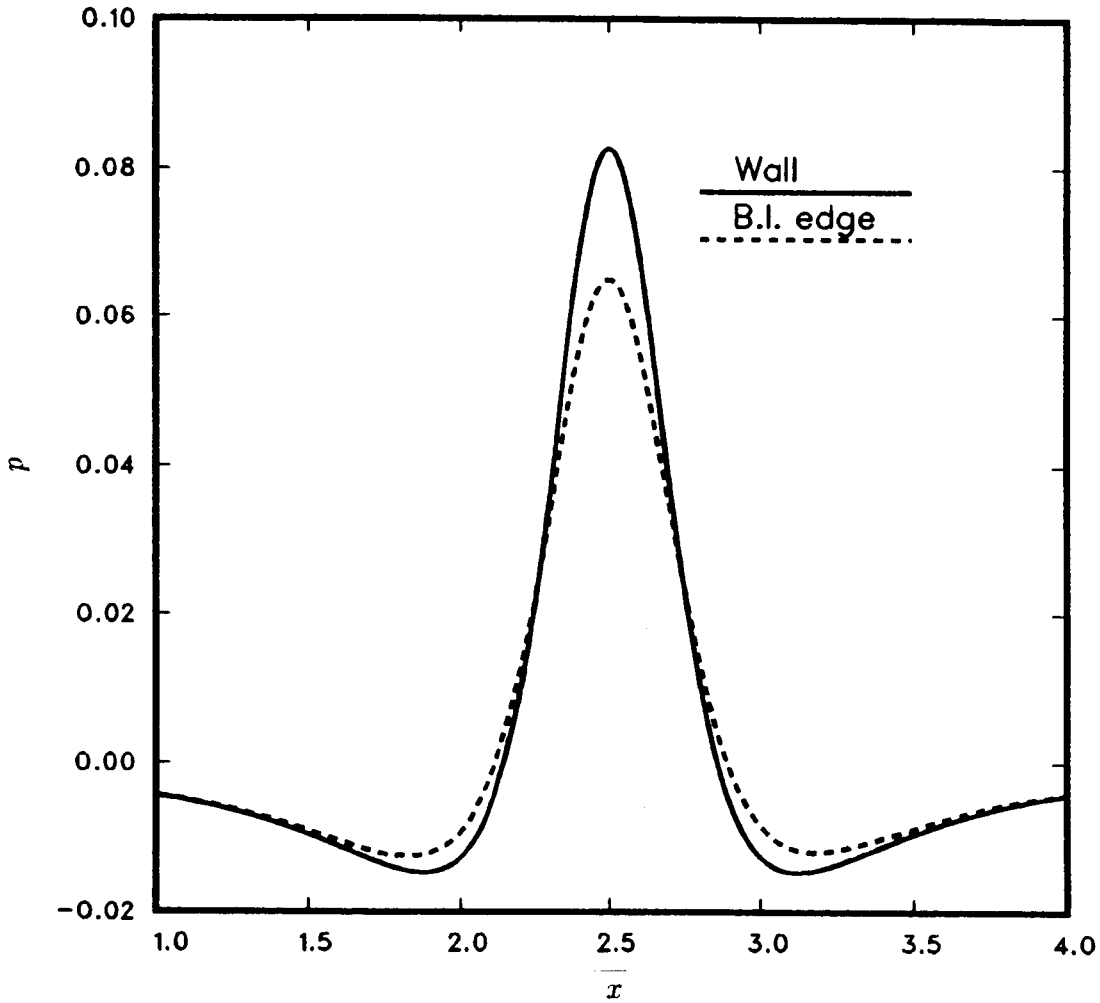

Figure 27. Variation of pressure gradient in the normal direction for inviscid flow

first twenty points considered in this study), with appropriate vorticity boundary conditions derived from the dual potential solution applied at the "edge" of the boundary-layer grid (instead of the usual irrotational assumption). Such a scheme could perhaps form the basis of a detailed study on the breakdown of the boundary-layer equations in separated flow regions.

From the results presented in this section, it is possible to conclude that the dual potential formulation of the Navier-Stokes equations can be applied to calculate separated flows, but caution has to be exercised in using the boundary-layer equations to supply the vorticity in regions away from the wall.

D. Flow Over a Three-Dimensional Trough

The dual potential - boundary layer interaction procedure was applied to compute the incompressible laminar attached flow over a three-dimensional trough configuration and results for this case are presented in this section.

1. Grid and geometry

The geometry considered here is a three-dimensional version of the geometry considered in the previous section and a schematic view is given in Figure 28. Edwards (1986) obtained a solution for this geometry using an interacting boundary-layer algorithm coupled with an inviscid small-disturbance analysis, while Davis et al. (1986) obtained a viscous flow solution for this geometry using a vorticity/stream-function type formulation for the Navier-Stokes equations. The surface of this geometry is described by the function

$$z(x,y) = -t\,\mathrm{sech}(4x - 10)\,\mathrm{sech}(4y - 6) \tag{4.29}$$

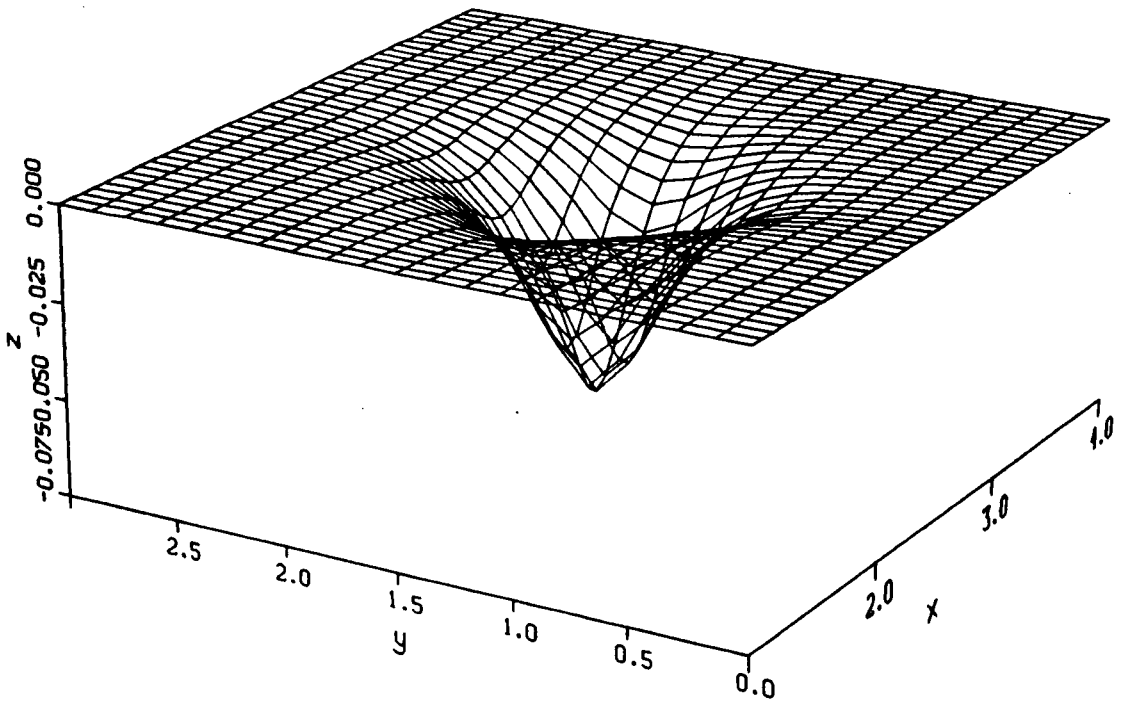

Figure 28. Schematic view of a three-dimensional trough

Once again, the reference length for this geometry is $L = 1\,m$. The shape of the trough is symmetrical about the $y = 1.5$ plane. Results for inviscid, and viscous flow at a free stream Reynolds number based on the reference length of 8000 were compared with those of Davis et al. (1986) and Edwards (1986). These results show that the present dual potential procedure is capable of accurately predicting three-dimensional inviscid and viscous laminar flows.

Figure 29 shows a view of the computational grid in the x-z plane which was used to obtain a three-dimensional dual potential solution. The x- and z-computational boundaries were located in the region $1 < x < 4$, $0 < y < 3$. A total of $41 \times 40 \times 51$ grid points were used. A uniform grid distribution was used in the x- and y-directions. The 51 points in the z-direction were distributed from the lower surface to $z = 5$ with a minimum spacing at wall equal to 0.0001. In all calculations, periodic boundary conditions were used in the y-direction. For inviscid flow, the following boundary conditions were used at the other boundaries:

Inflow:

$$\chi = \psi = \vartheta = 0; \quad \phi_x = u_\infty \tag{4.30}$$

Outflow:

$$\chi_{xx} = \psi_{xx} = \vartheta_{xx} = 0; \quad \phi_x = u_\infty \tag{4.31}$$

Wall:

$$\vartheta = \chi = 0, \quad \psi_z = -(\vartheta_x + \chi_y), \quad \phi_n = 0 \tag{4.32}$$

Far field:

$$\vartheta = \chi = 0, \quad \psi_z = -(\vartheta_x + \chi_y), \quad \phi = u_\infty x \tag{4.33}$$

Note that the flow at the inflow boundary ($x = 1$) is assumed to be uniform because the trough thickness asymptotically goes to zero away from the center so that at this

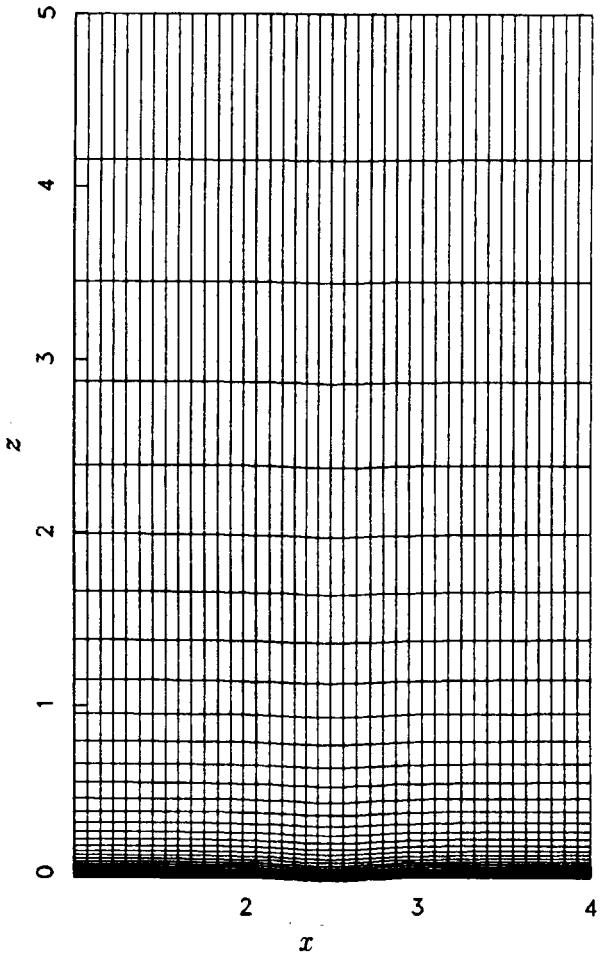

Figure 29. View of the sheared grid for the three-dimensional trough in the x-z plane at $y = 1.5$

boundary, the thickness is practically negligible ($t = 0.00016$). Another reason for choosing this boundary condition was to match those used by Davis et al. (1986). It will be shown that for the conditions studied, these boundaries are adequate to capture any elliptic effects, and provide a smooth solution for the flow field.

For viscous flow, the same boundary conditions were used at all but the inflow boundary, where χ was computed by solving a one-dimensional Poisson equation for a prescribed vorticity. The vorticity for this boundary was obtained from the boundary-layer profile for the velocity at this location, which was obtained from a Falkner-Skan solution (e.g., White, 1974).

Figure 30 shows the grid in the plane of symmetry which was used to obtain the boundary-layer solution. The edge of the grid in the $\bar{z}$-direction is not uniform in $\bar{x}$ but varies as the square root of $\bar{x}$. At the inflow boundary, the grid extends from $\bar{z} = 0$ to $\bar{z} = \bar{z}_{max} = \sigma\delta^*$ where δ^* is the displacement thickness for a flat plate boundary-layer at a distance of $\bar{x} = 1$ from the leading edge, and σ is a coefficient to account for boundary-layer growth due to adverse pressure gradients. In this study, a value of $\sigma = 50$ was used giving a value of $\bar{z}_{max} = 0.2$ at the inflow boundary. Once again, a nonuniform grid was used in the $\bar{z}$-direction, with a total of 51 points extending from $\bar{z} = 0$ to $\bar{z} = \bar{z}_{max}$ with a minimum spacing at the wall of 0.0001.

Since the grids in the z-direction in the boundary-layer and dual potential codes are not necessarily identical, a cubic spline function interpolation scheme is used to interpolate the vorticity components from the boundary-layer grid to the dual potential grid. For the geometries considered in this study, the variations in the x- and y-directions between the two grids is small and vorticity was interpolated only as a function of the normal direction z (or $\bar{z}$).

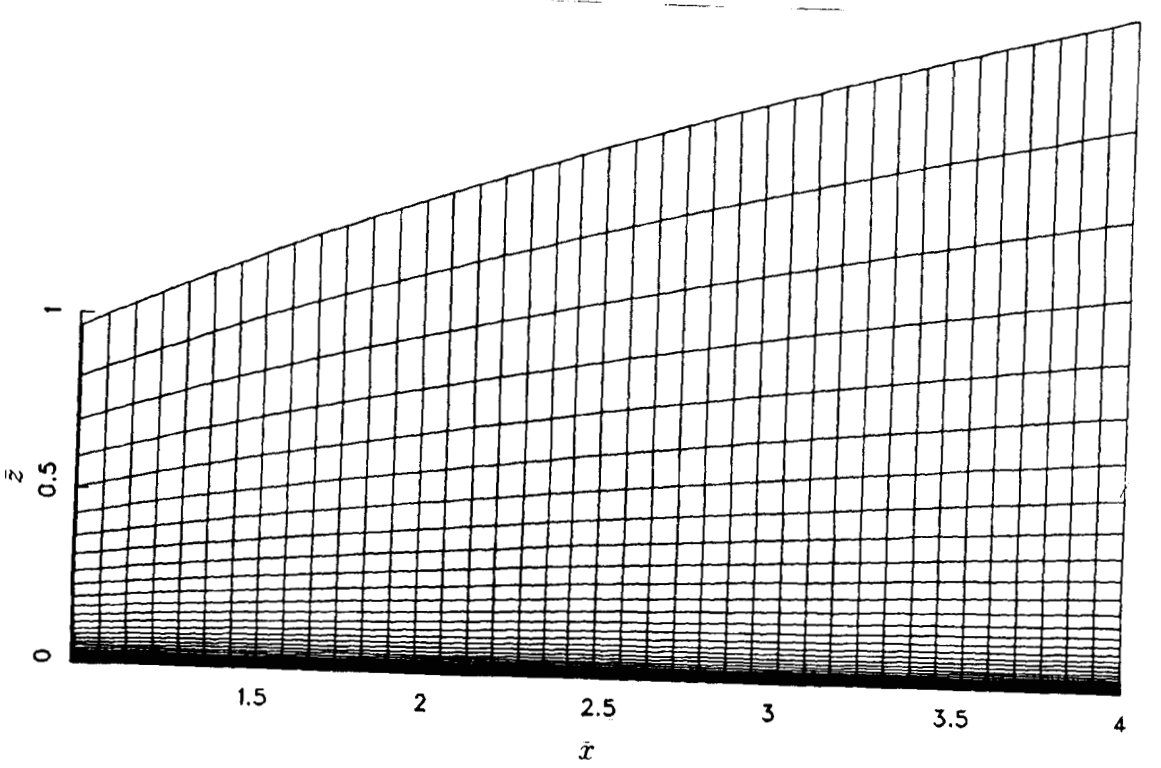

Figure 30. Boundary-layer grid in x-z plane

2. Inviscid results

As another simple verification of the numerical procedure, a three-dimensional inviscid solution was calculated for a $t = 0.06$ trough with the scalar potential function alone. Figures 31 and 32 are contour plots of the u- and v-velocity distributions on the surface of the trough. These figures show that the predicted velocity distributions are smooth and that the flow becomes almost uniform at the outflow boundaries. The three-dimensional flow produced by the trough is illustrated by Figure 32, which shows that upstream of the maximum depth of the trough, the pressure gradients created by the increasing depth of the trough push the flow towards the plane of symmetry, while in the downstream half of the geometry, the flow is in the direction away from the plane of symmetry. More detailed plots of the x- and y- components of the velocity are given in Figures 33 and 34 at two different y-planes and compared with other numerical results. Figure 33 is a plot of the streamwise velocity u on the surface of the trough versus x, while Figure 34 is a plot of the spanwise velocity v on the surface of the trough versus x. Comparisons with other numerical computations as taken from Davis et al. (1986) are shown in these two figures. The agreement with the results of Edwards (1986) and Davis et al. (1986) is relatively good for the u velocity with the present results having values in between these other results. However, for the v velocity (Figure 34), the present results agree well with those of Edwards and differ slightly from those of Davis et al.

It should be pointed out that the results of Davis et al. (1986) were obtained on a $81 \times 41 \times 81$ grid. In the present calculations, which were performed on a CRAY XMP-48 with a maximum allowable memory of 4 million bytes, it was not possible to obtain solutions with finer grids. Hence, results were obtained with coarser grids

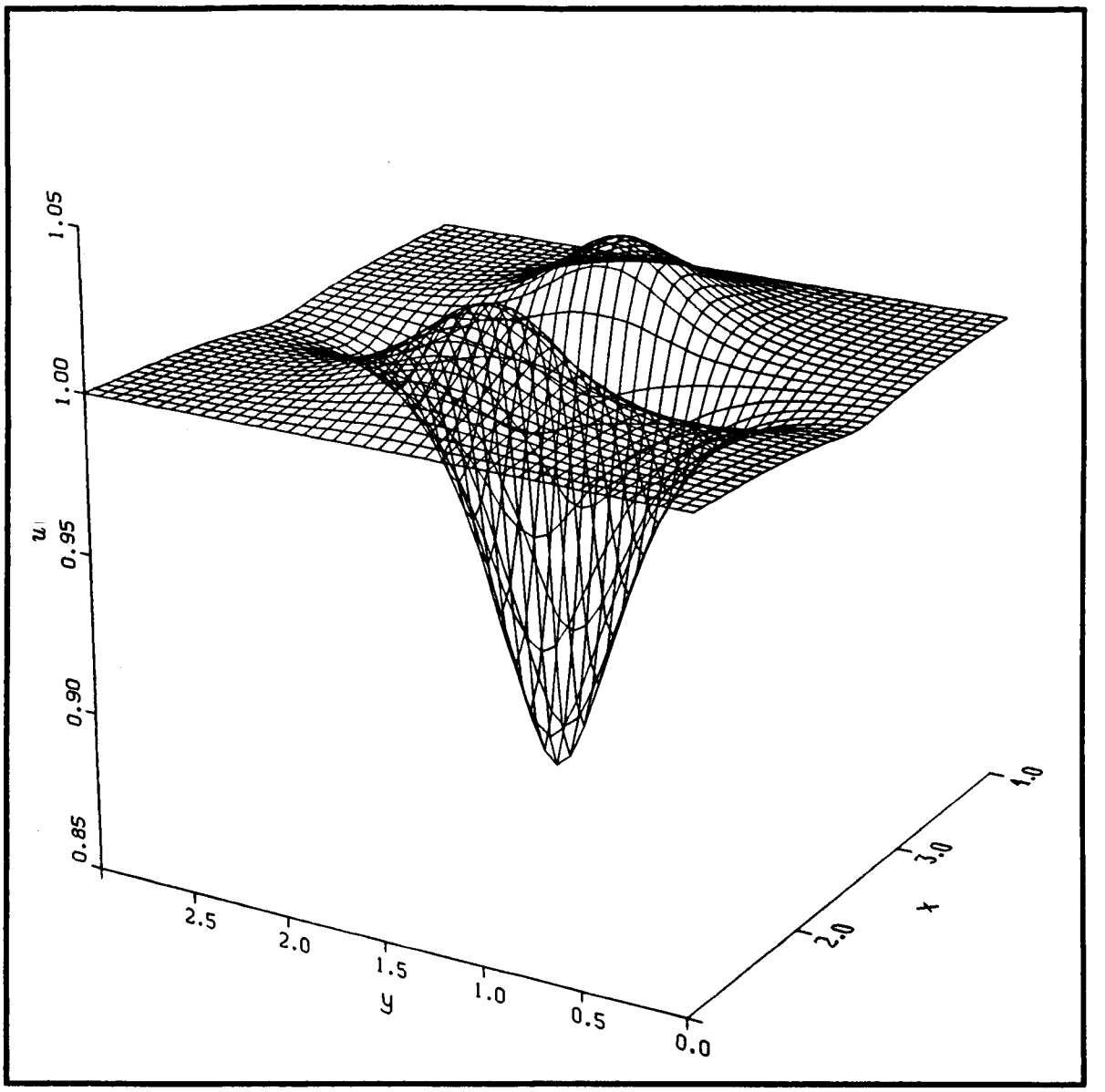

Figure 31. Contour plots of inviscid u velocity at the surface, $t = 0.06$

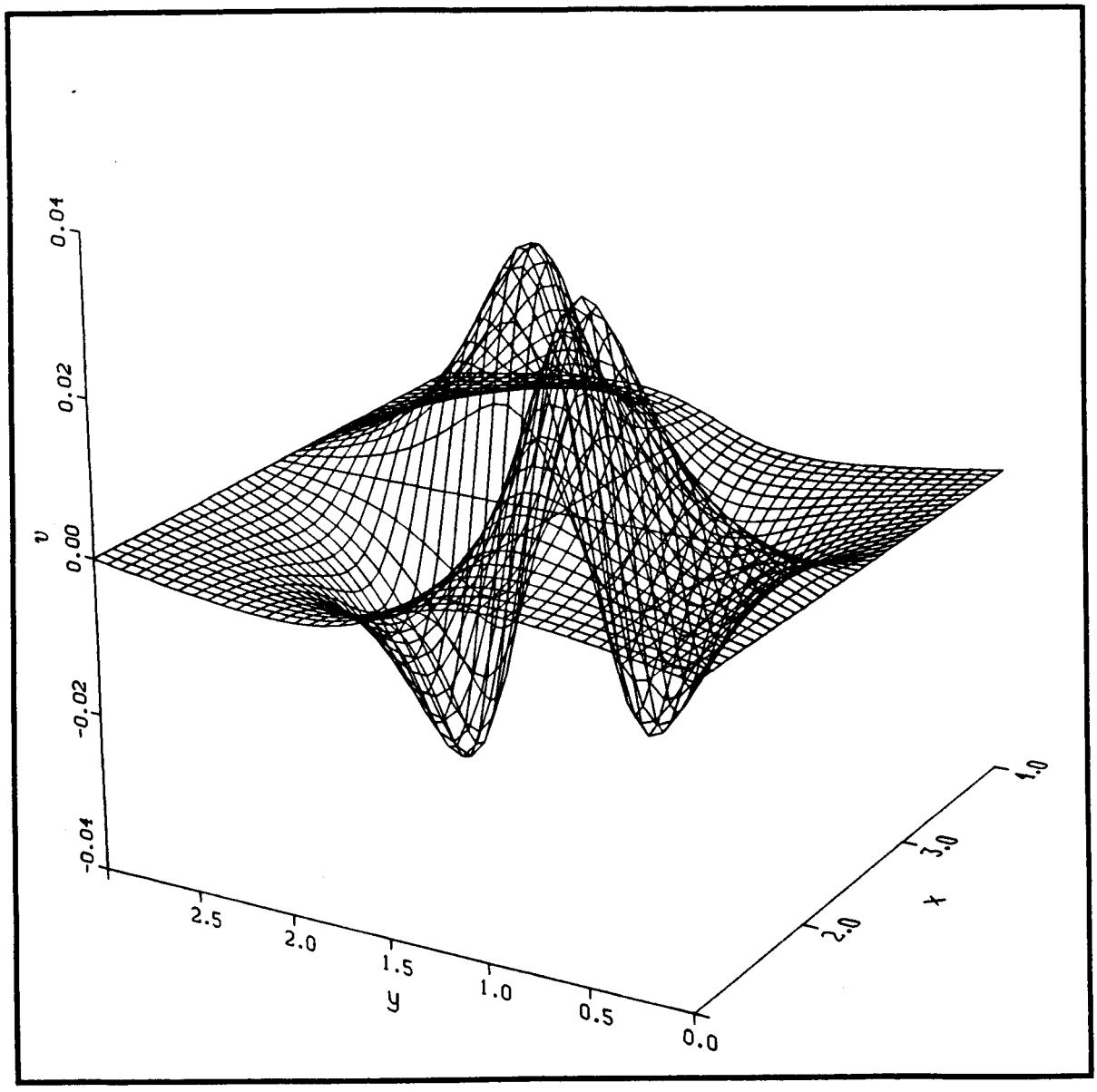

Figure 32. Contour plots of inviscid v velocity at the surface, $t = 0.06$

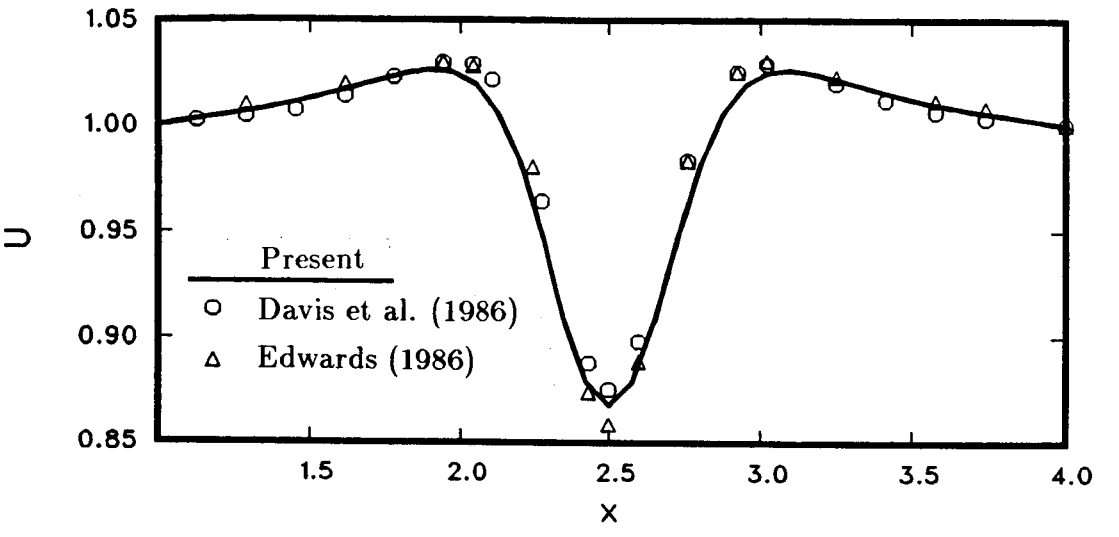

(a)

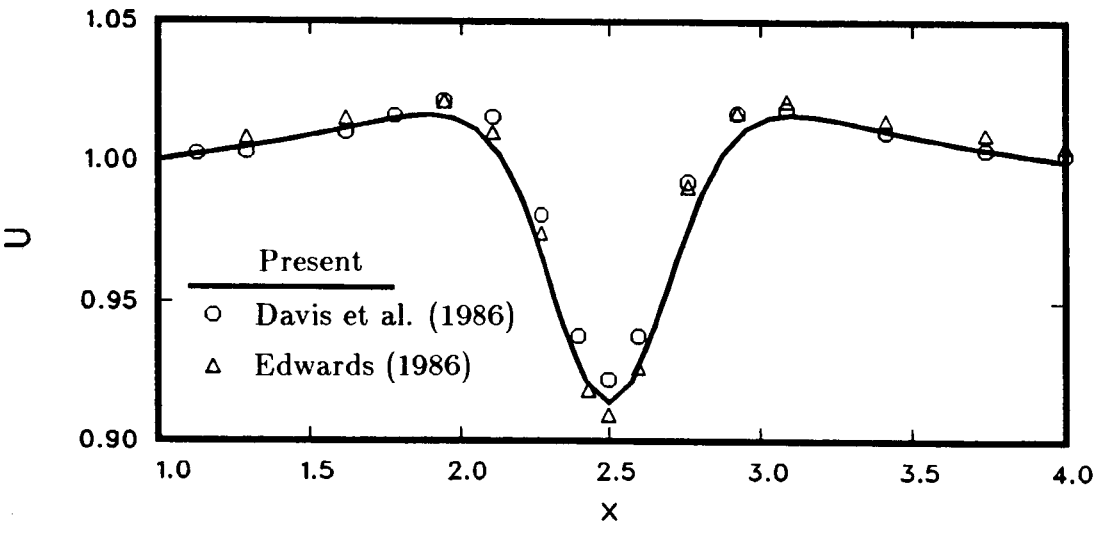

(b)

Figure 33. Streamwise variation of inviscid u velocity at the surface, $t = 0.06$. a) $y = 1.5$; b) $y = 1.2$

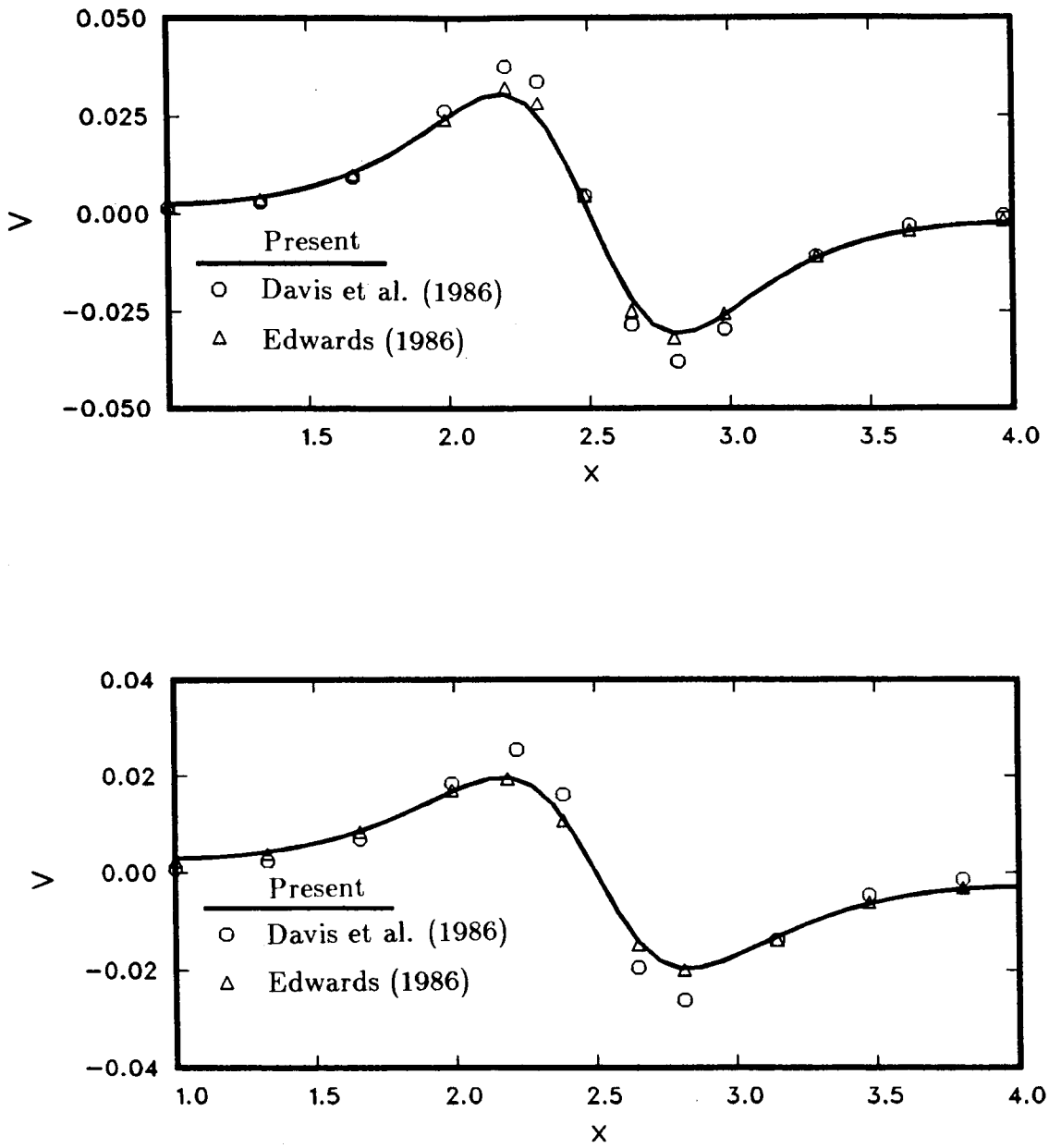

Figure 34. Streamwise variation of inviscid v velocity at the surface, $t = 0.06$. a) $y = 1.2$; b) $y = 0.9$

to determine the effect of grid size on the solutions. Figures 35 and 36 show results obtained with a $41 \times 20 \times 51$ grid compared with those from a $41 \times 40 \times 51$ grid. In these figures, the surface velocity components are plotted versus x at two spanwise locations for the two different grids. The figures show little or no difference in the results due to halving the number of grid points in the y-direction. All subsequent calculations, unless otherwise indicated, were performed on a $41 \times 40 \times 51$ grid

The present calculations required approximately 900 iterations and took about 300 seconds on the CRAY-XMP computer.

3. Viscous results

A three-dimensional viscous solution was calculated for a $t = 0.03$ trough at an upstream reference Reynolds number of 8000 with the interaction procedure described in §IV.B. For this configuration, the flow remained attached over the entire surface. The flow was once again assumed to be two-dimensional at the upstream boundary. The boundary layer velocity profile was found from a solution of the Falkner-Skan equations for zero pressure gradient flow (e.g., White, 1974) and scaled to the appropriate location in the $\bar{x}$-direction (in this case, $\bar{x} = 1.0$ from the leading edge of a flat plate).

As a measure of the agreement between the dual potential and boundary-layer solutions, the pressures from both schemes (that is, the pressure which is specified to the boundary-layer equations, and the pressure from the boundary-layer solution which is calculated from Bernoullis's equation applied at the edge of the boundary-layer) at the plane of symmetry are presented in Figure 37. The agreement between the two is relatively good indicating the convergence of the interaction scheme. Some discrepancy is attributed to the different formulations and numerical algorithms.

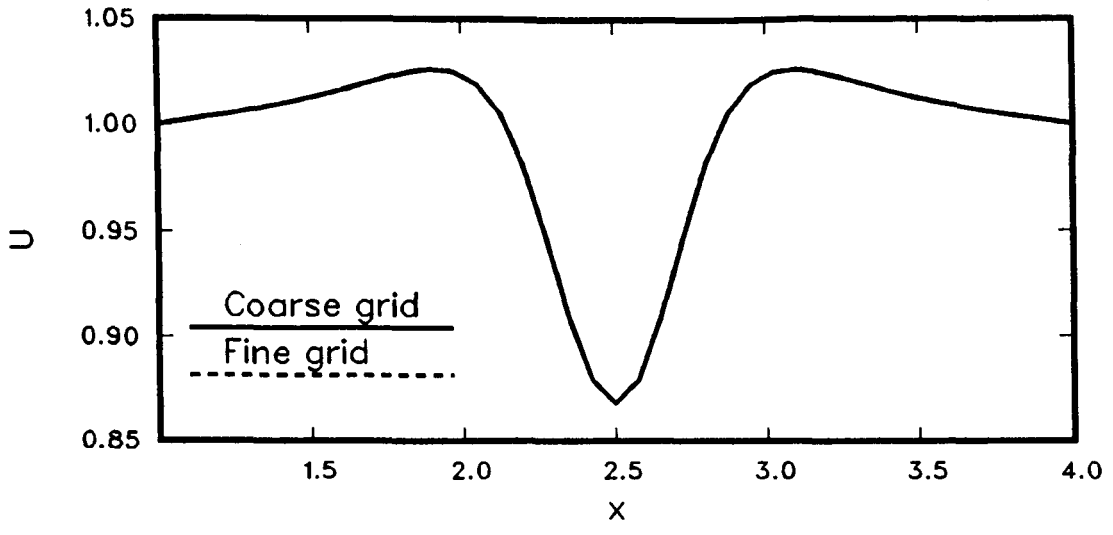

(a)

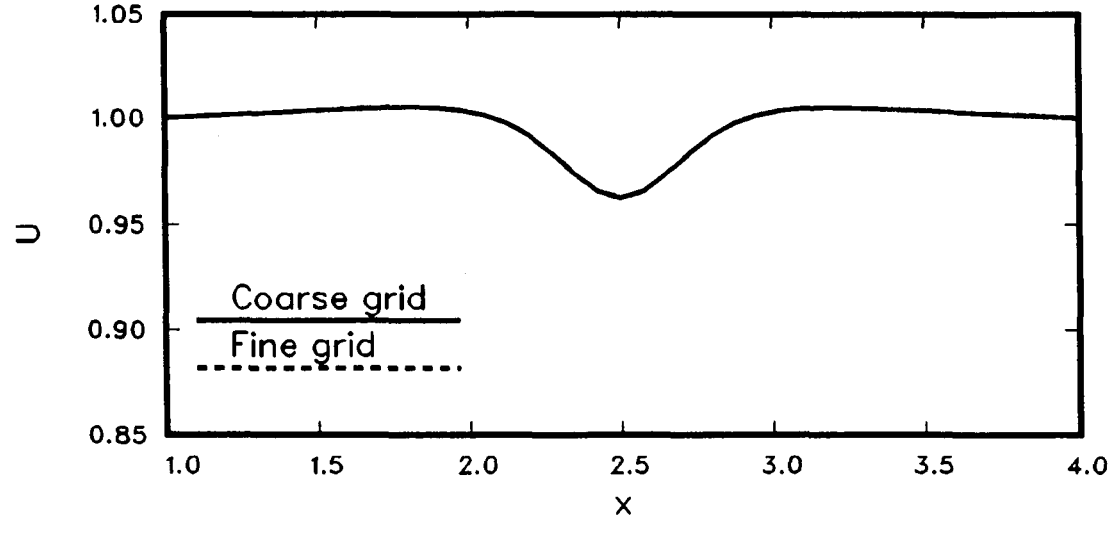

(b)

Figure 35. Effect of grid refinement on inviscid u velocity at the surface, $t = 0.06$. a) $y = 1.5$, b) $y = 0.9$

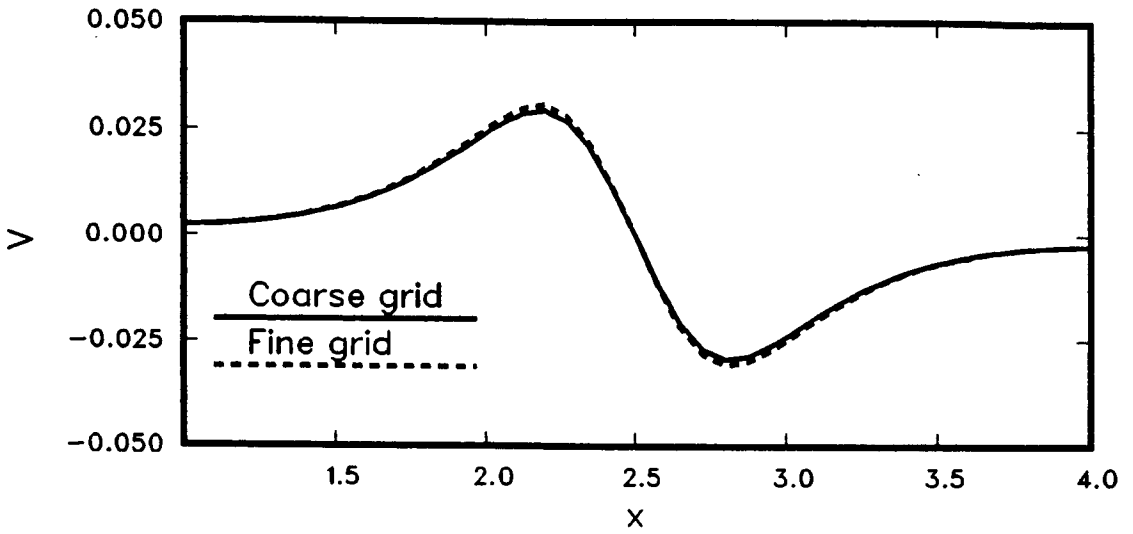

(a)

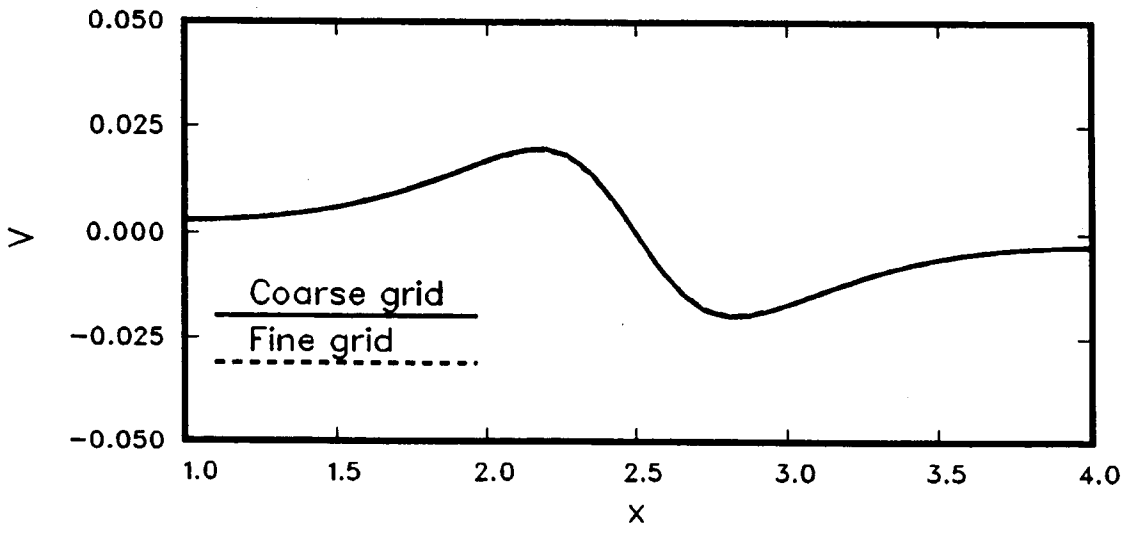

(b)

Figure 36. Effect of grid refinement on inviscid v velocity at the surface, $t = 0.06$. a) $y = 1.2$, b) $y = 0.9$

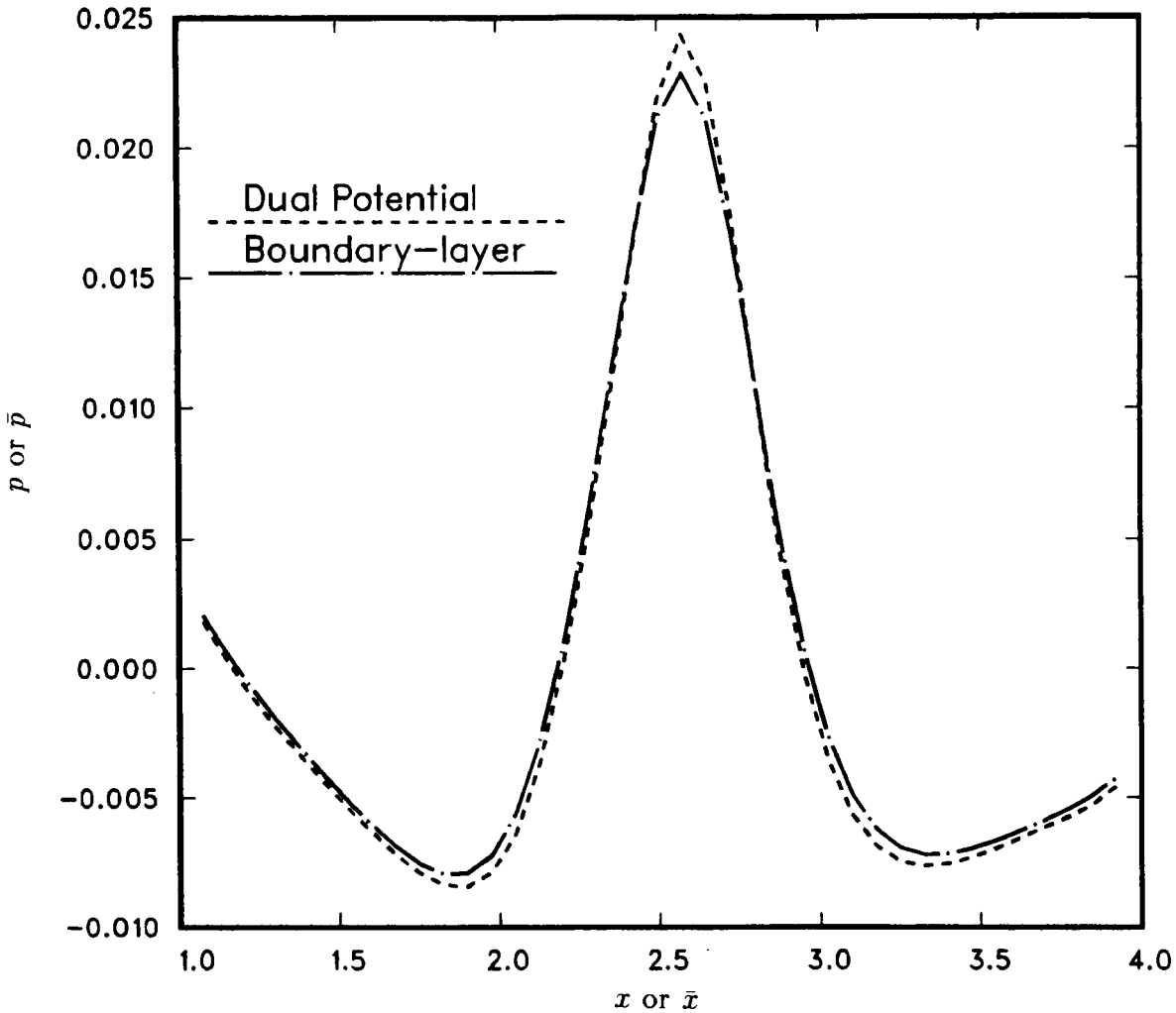

Figure 37. Comparison of dual potential and boundary-layer pressures at plane of symmetry ($y = 1.5$), $t = 0.03$

Figures 38-43 are contour plots of the wall shear stresses, the integral thicknesses, the displacement thickness, and the boundary-layer pressure, respectively, for the three-dimensional trough geometry. These figures give a qualitative picture of the flowfield. The growth of the boundary layer is evident from the displacement thickness plots. It can be seen from these figures that the flow starts as two-dimensional, and then following the geometry, becomes three-dimensional towards the center of the trough. However, the flow does not become two-dimensional as it approaches the outflow boundary, even though the geometry reverts to a flat surface, but reaches a quasi three-dimensional state. This is clearly evident in Figure 42, which is a contour plot of the displacement thickness. A comparison of Figures 40 and 42 also illustrates the effect of the cross-flow on the displacement thickness for the trough geometry. The presence of cross-flow has decreased the displacement effect of the boundary-layer from what it would have been if the flow was purely two-dimensional.

A qualitative estimate of the viscous effects on the inviscid flow is obtained by comparing the pressure from the interaction solution in Figure 43 with a contour plot of the inviscid pressure for this case which is given in Figure 44. The two figures show that even for this attached flow case, there is considerable interaction of the boundary-layer with the outer inviscid flow. In particular, the pressure from the interaction solution varies from -0.010 to 0.025 whereas the inviscid pressure varies from -0.02 to 0.08 in the flow domain.

Detailed results for the boundary-layer parameters are presented in the line plots given in Figures 45-49. These figures are plots of the streamwise variation of the various flow parameters at different span locations. Since the flow is symmetric about the $y = 1.5$ plane, results on only one side of the plane of symmetry are

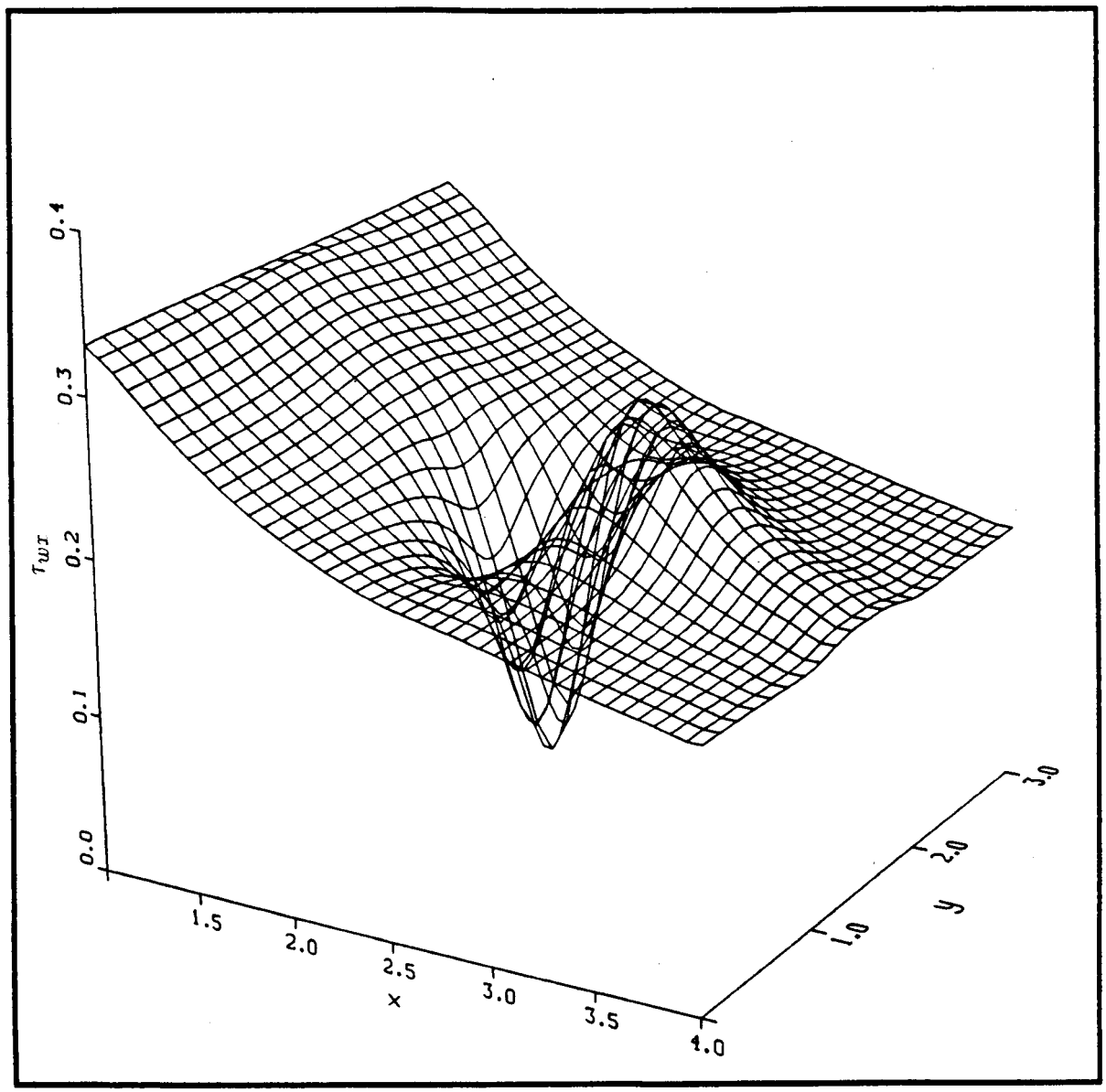

Figure 38. Contour plot of x-component of wall shear stress, $t = 0.03$

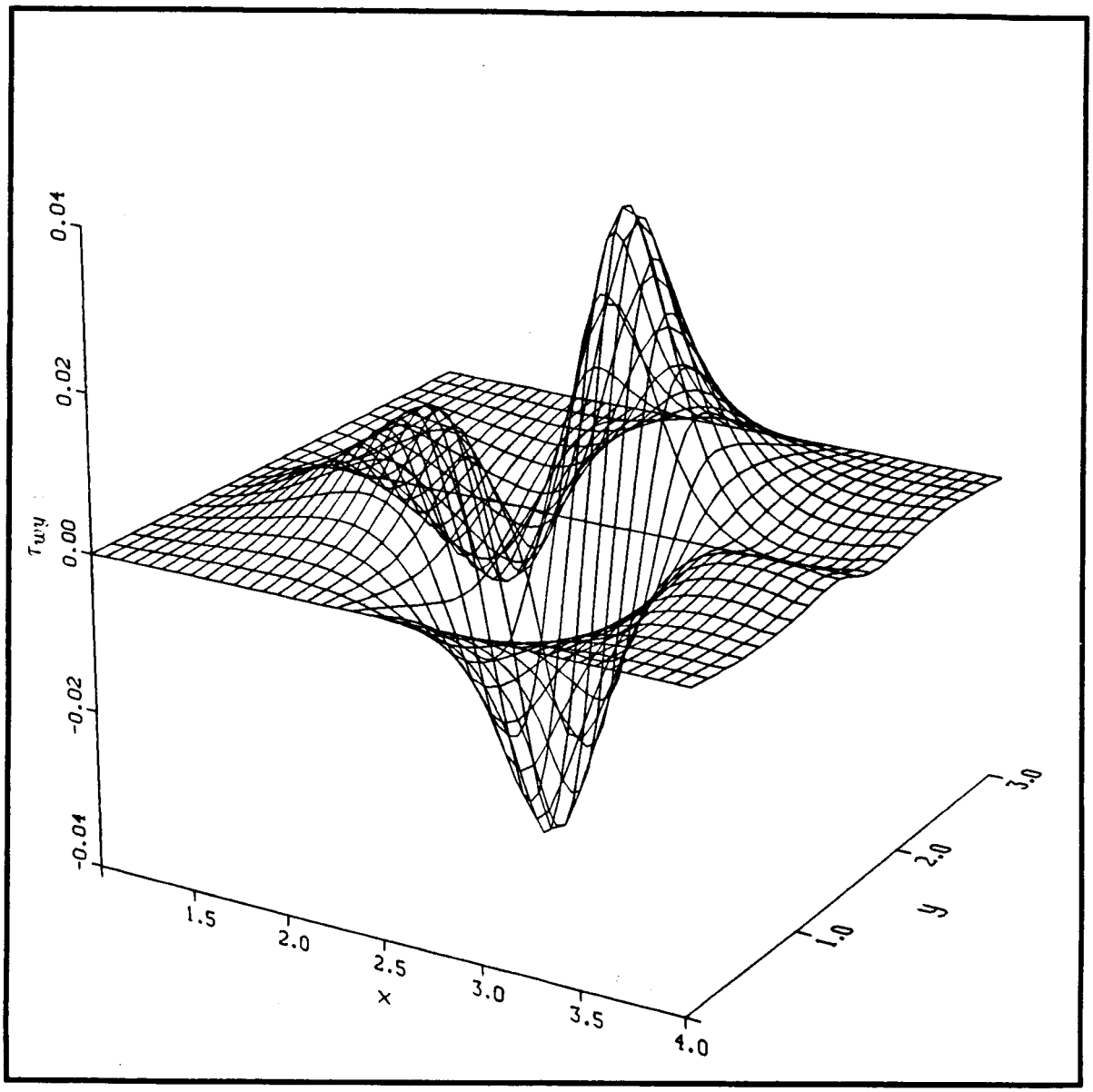

Figure 39. Contour plot of y-component of wall shear stress, $t = 0.03$

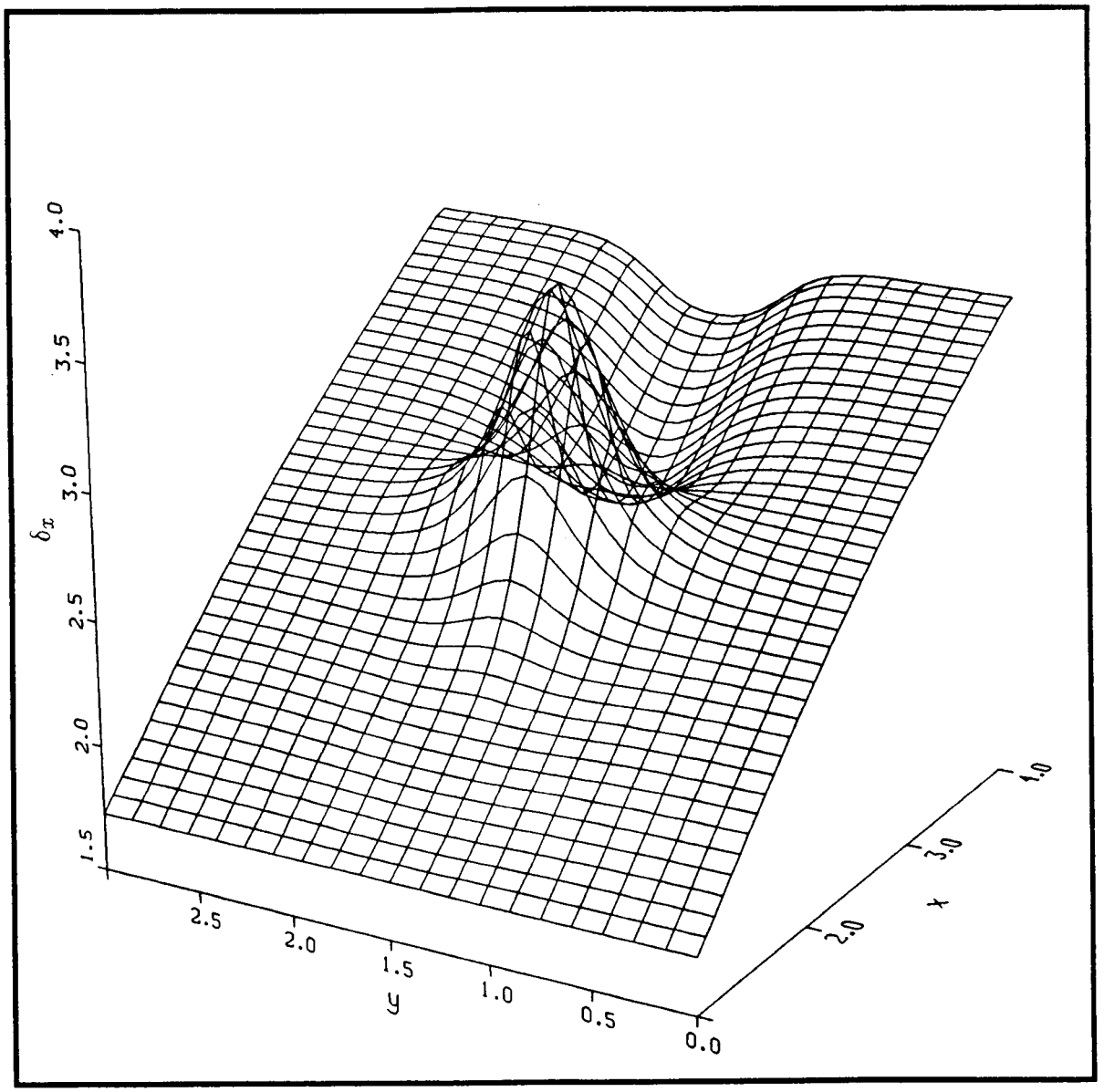

Figure 40. Contour plot of integral thickness in the x-direction, $t = 0.03$

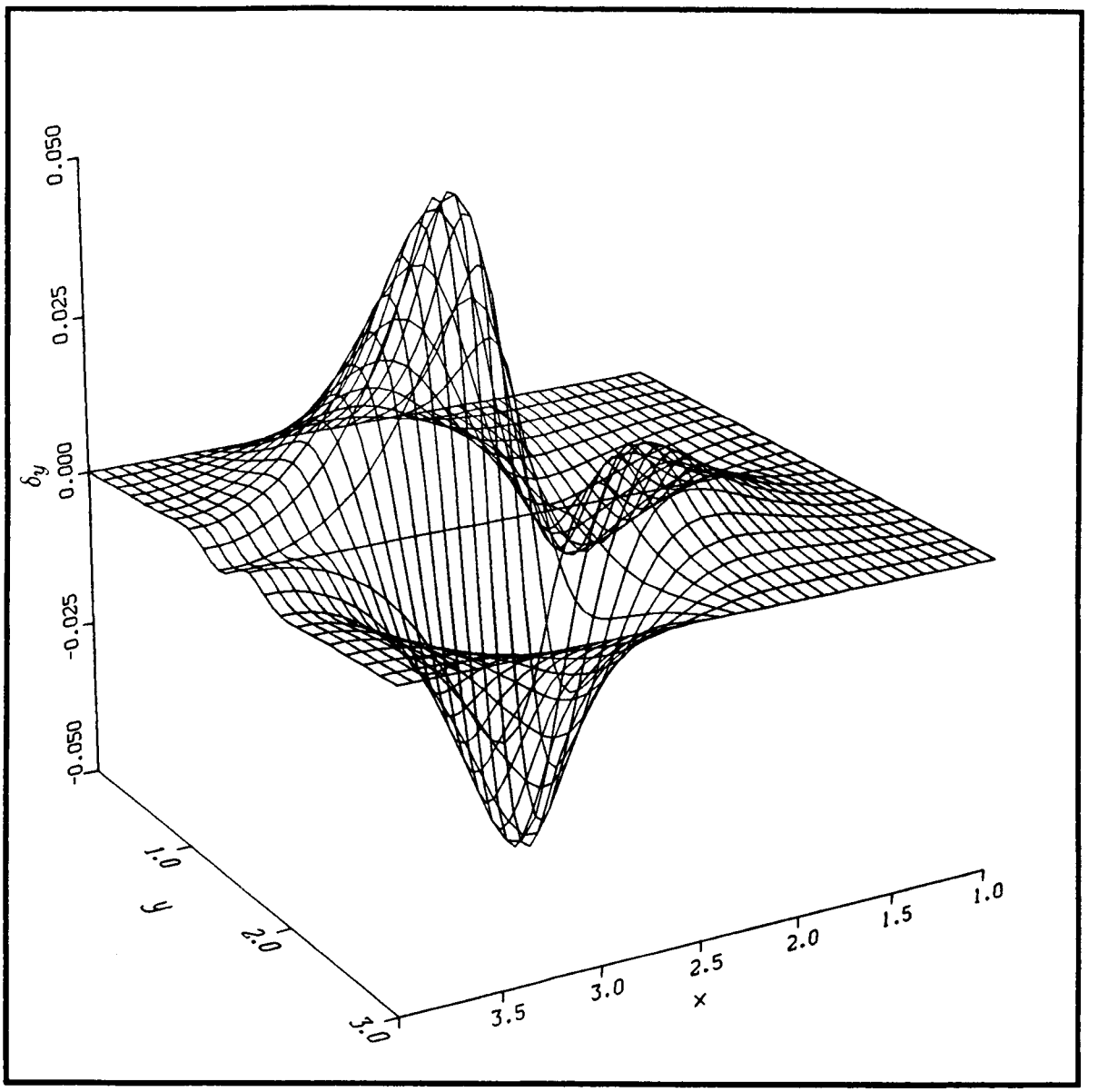

Figure 41. Contour plot of integral thickness in the y-direction, $t = 0.03$

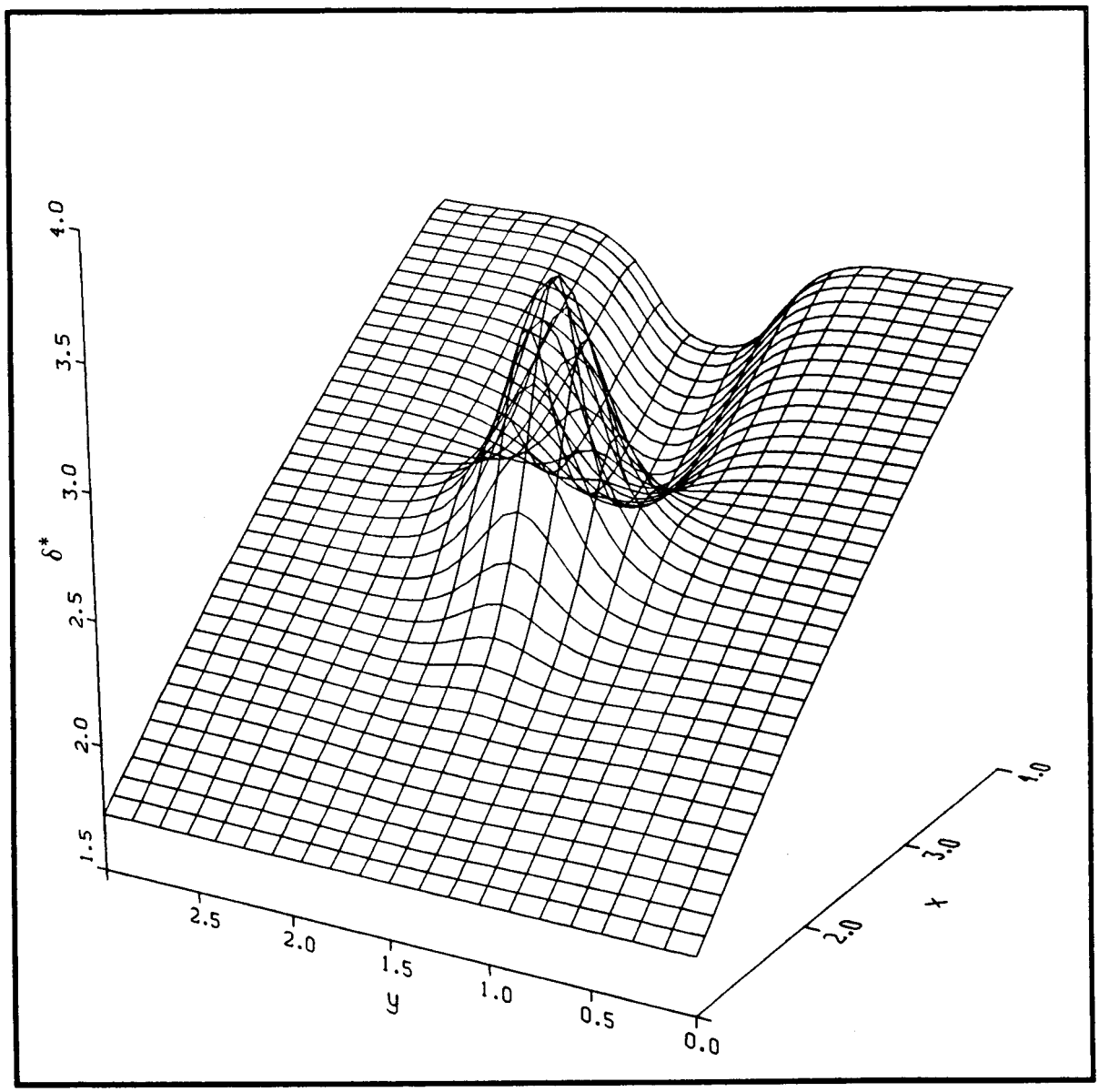

Figure 42. Contour plot of displacement thickness, $t = 0.03$

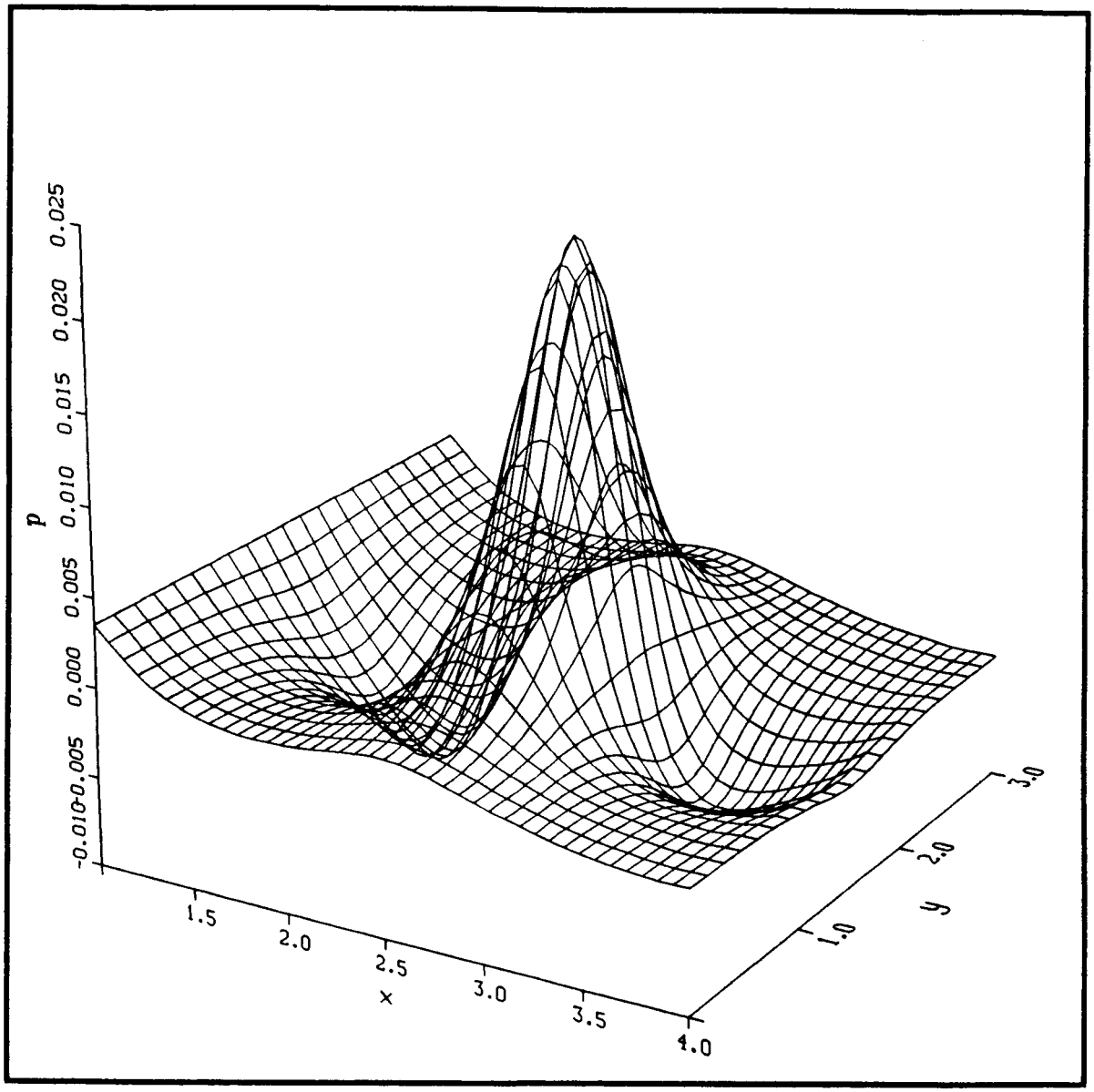

Figure 43. Contour plot of pressure from the interaction solution, $t = 0.03$

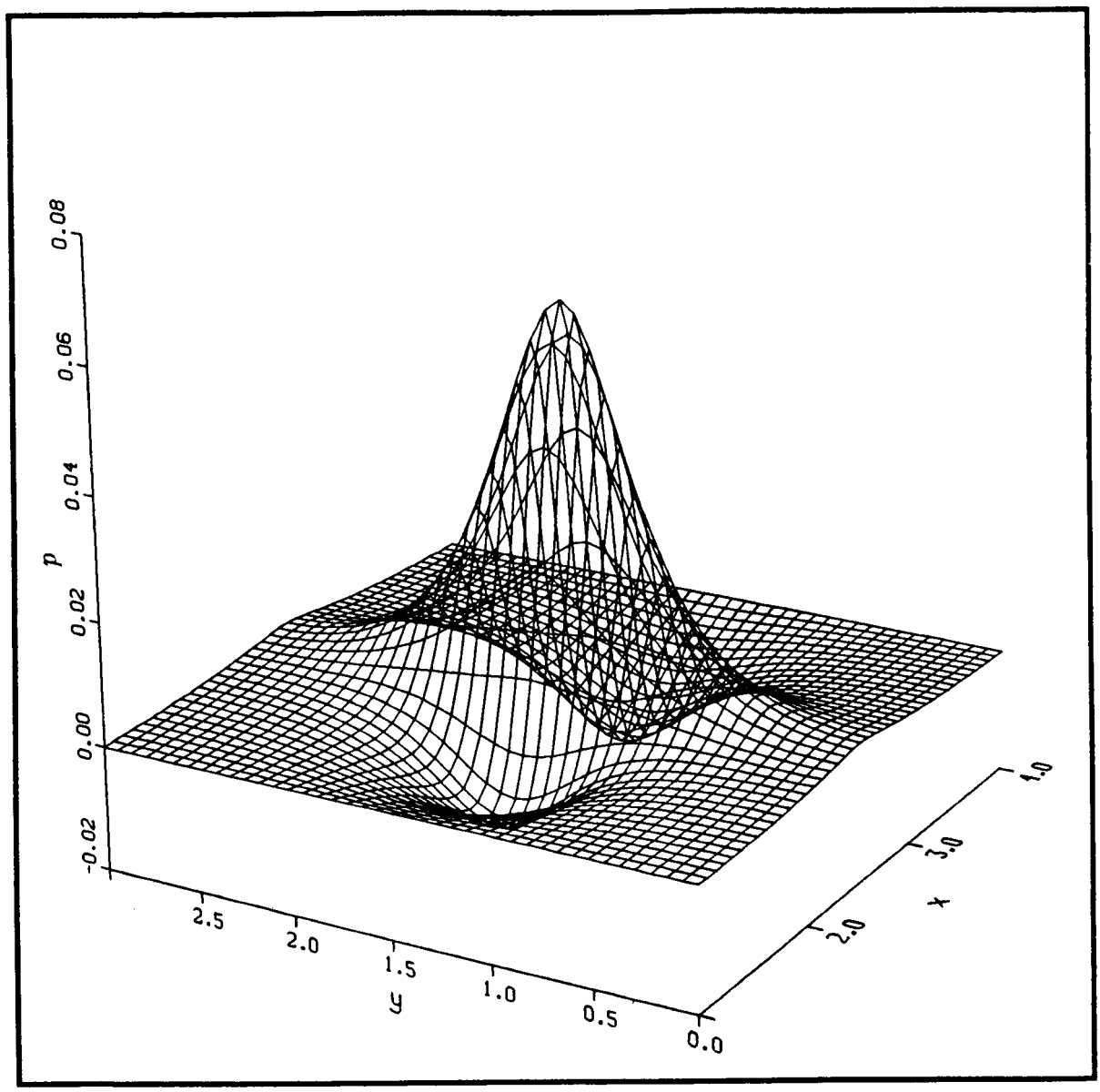

Figure 44. Contour plot of pressure from the inviscid solution, $t = 0.03$

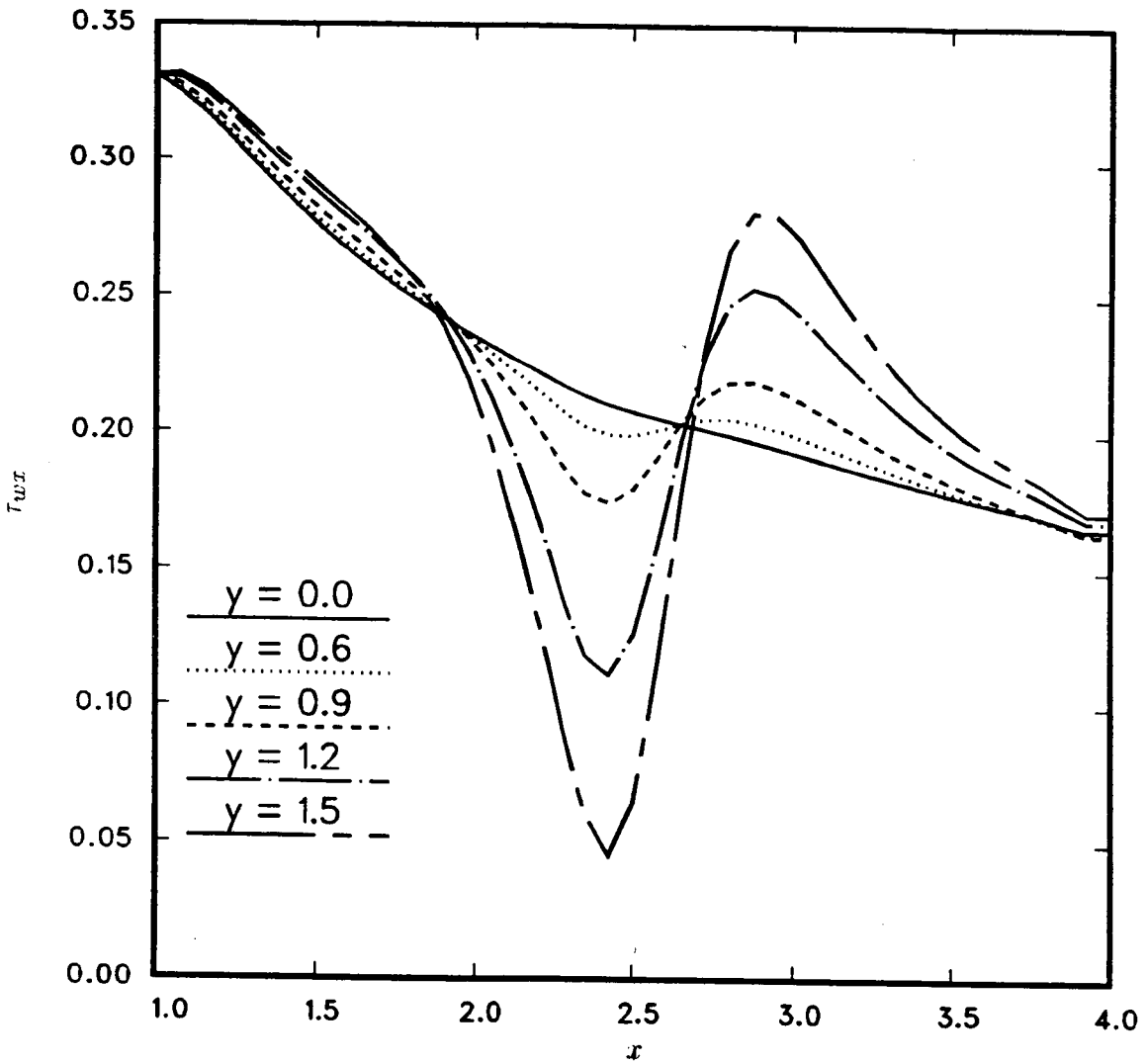

Figure 45. Variation of the x-component of wall shear stress, $t = 0.03$

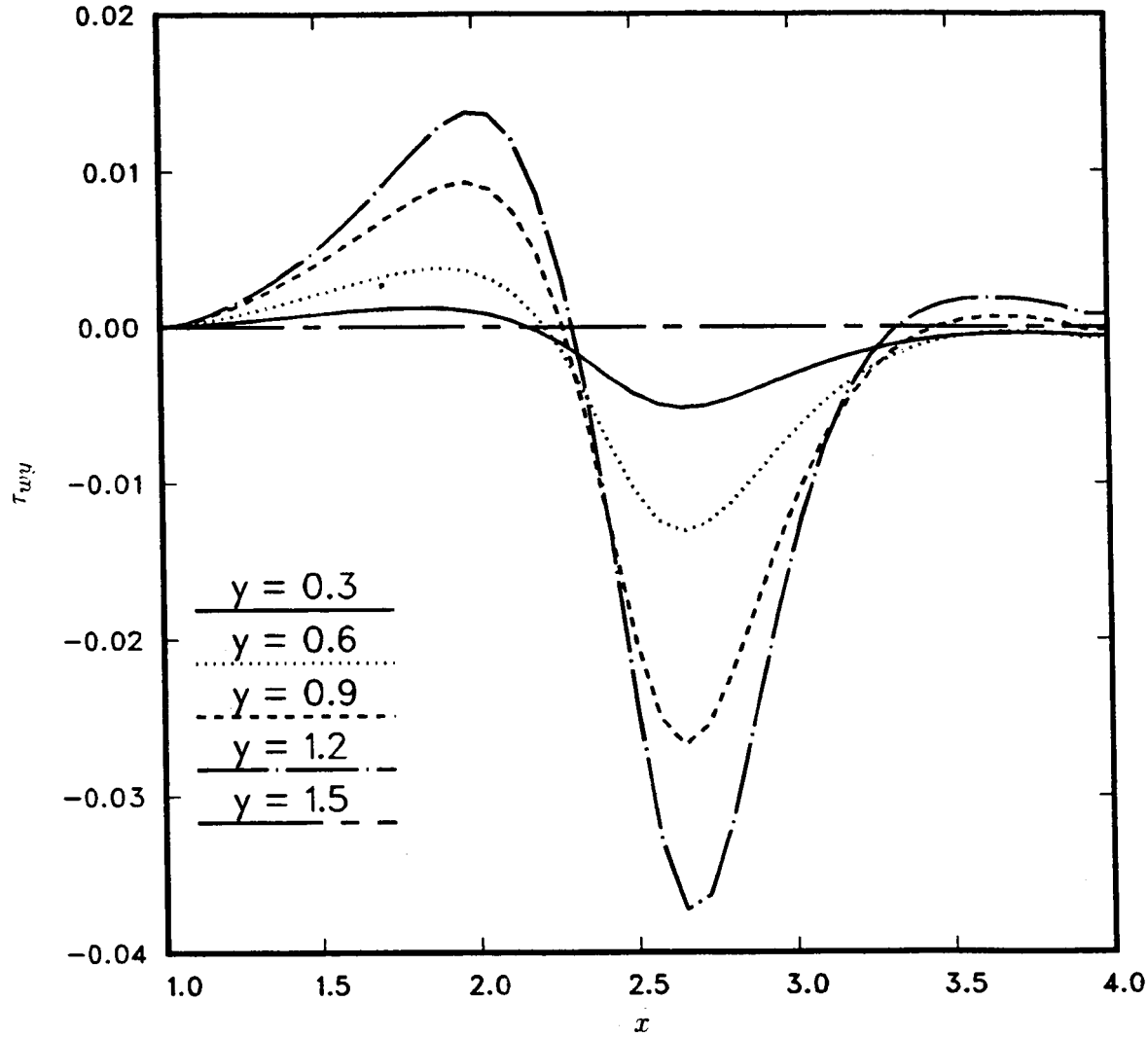

Figure 46. Variation of the y-component of wall shear stress, $t = 0.03$

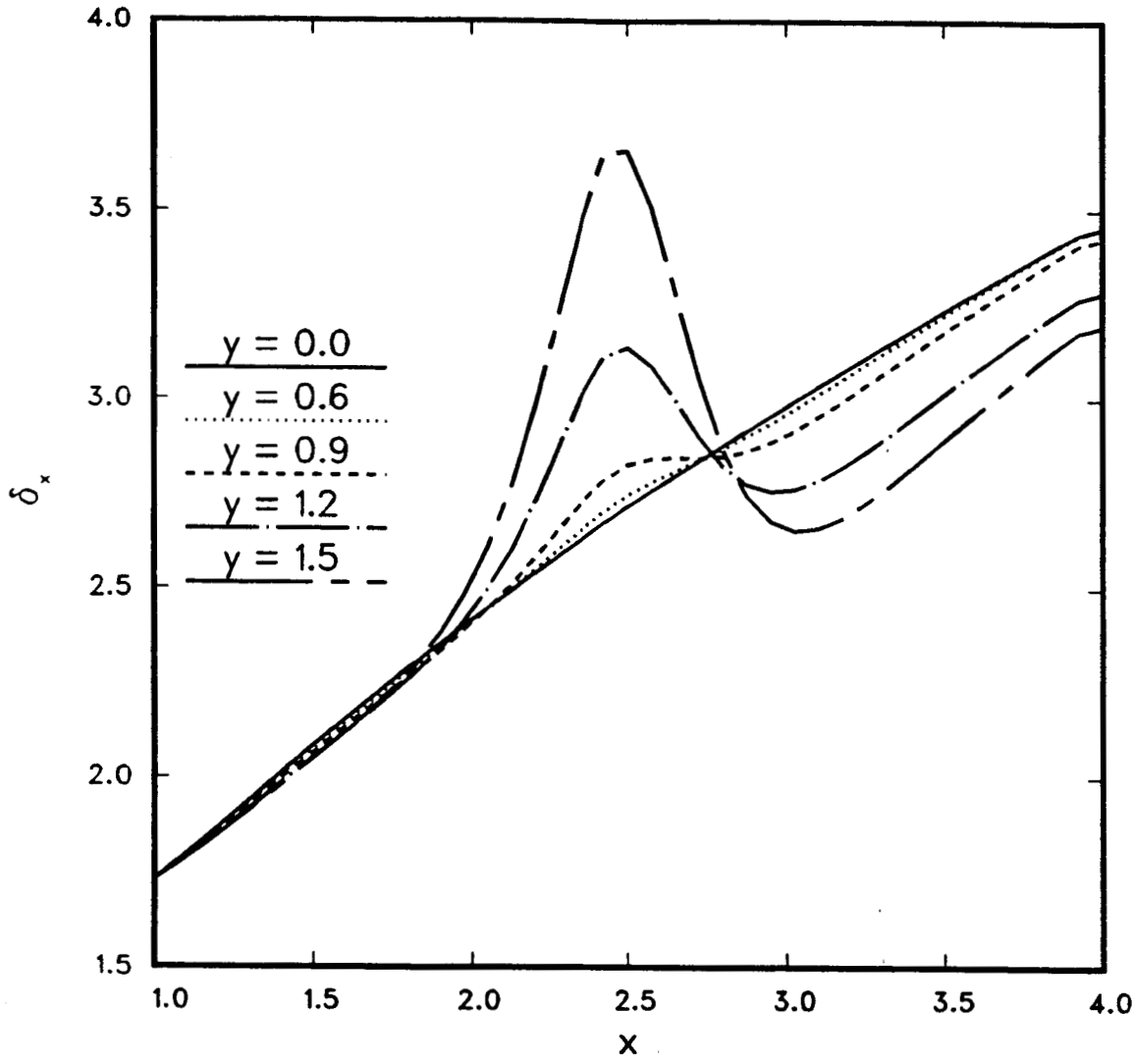

Figure 47. Variation of the integral thickness in the x-direction, $t = 0.03$

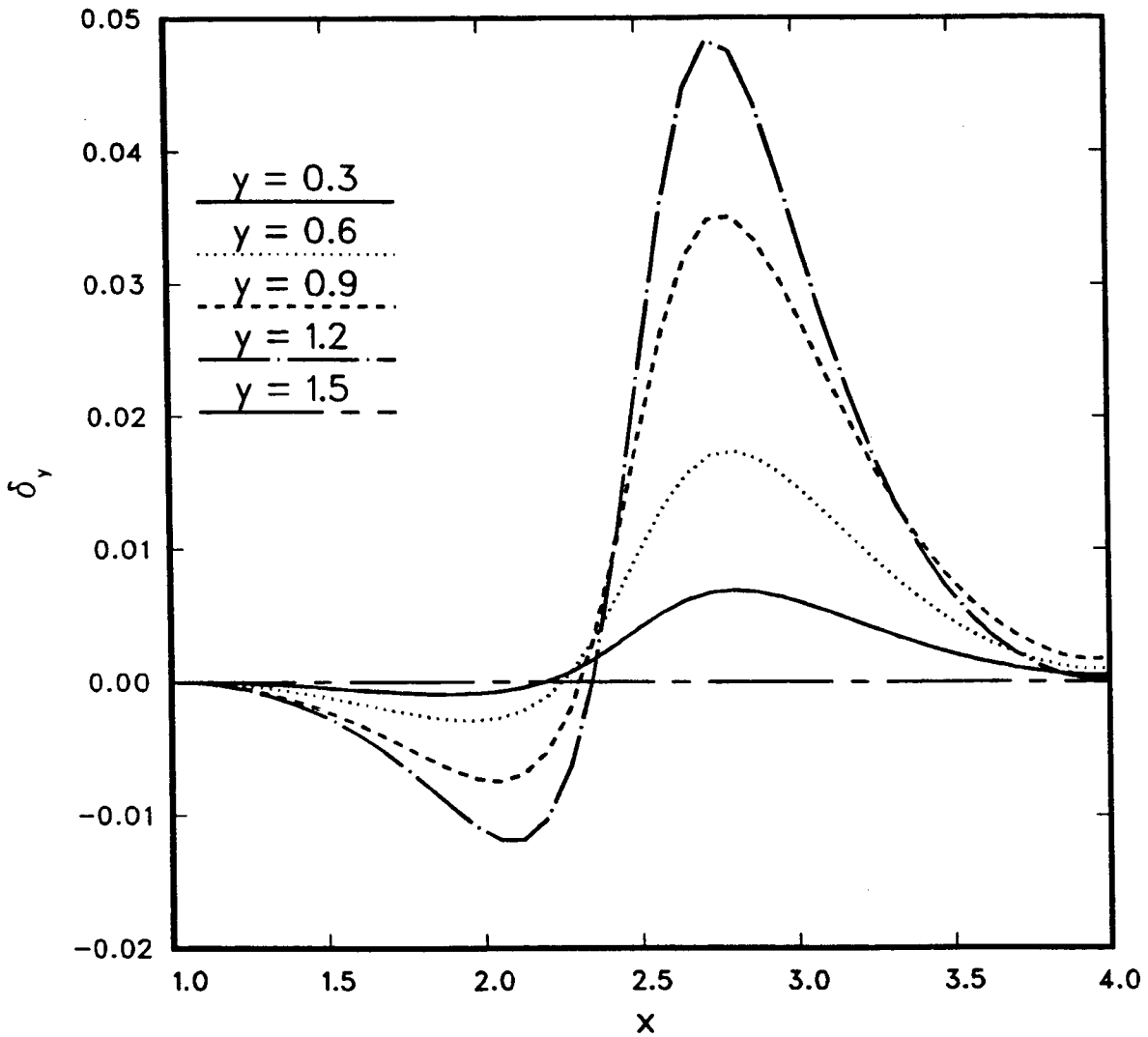

Figure 48. Variation of the integral thickness in the y-direction, $t = 0.03$

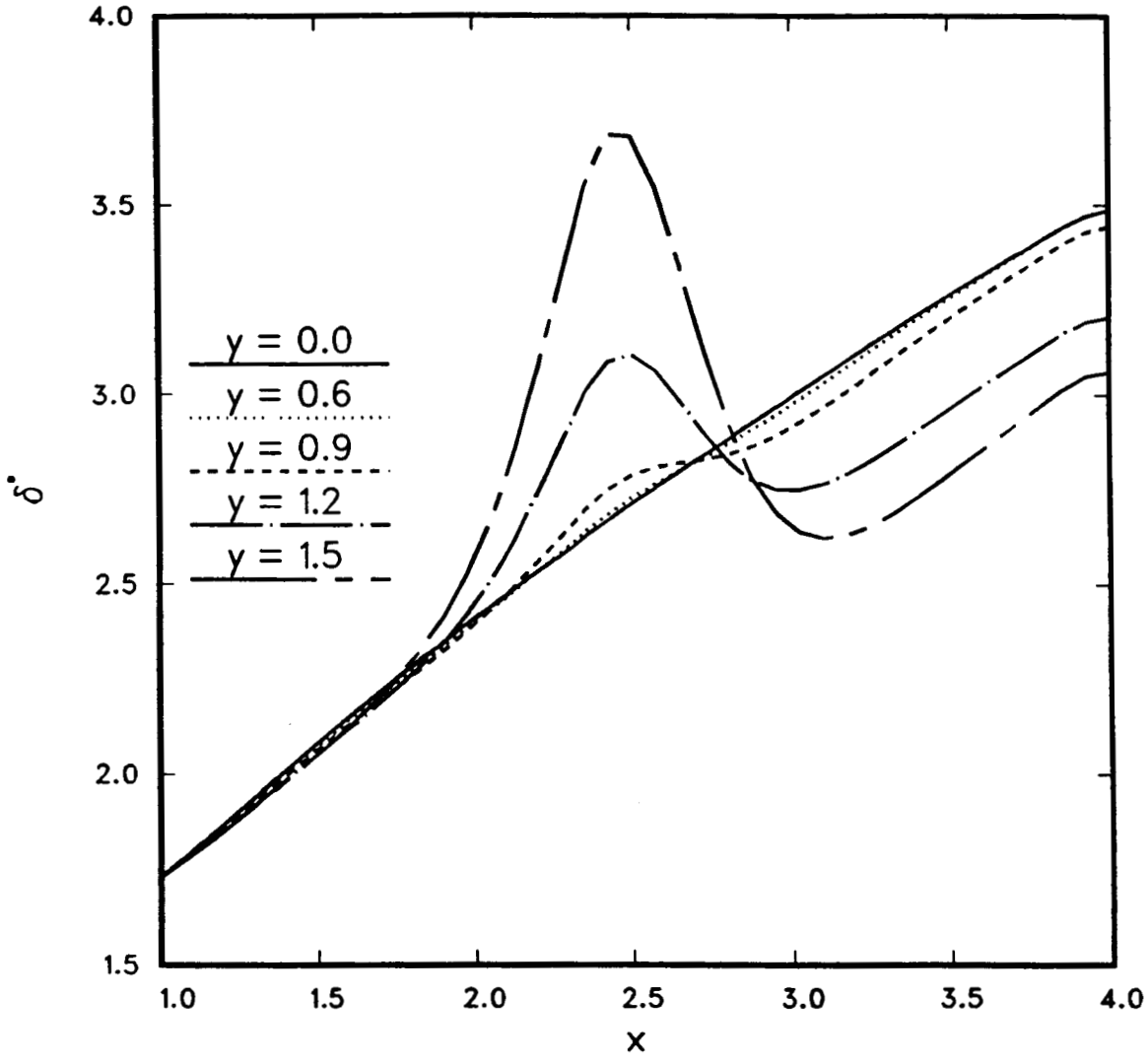

Figure 49. Variation of the displacement thickness, $t = 0.03$

plotted. Comparison with other numerical results as obtained from Davis et al. (1986) are presented in Figures 50 and 51. Figure 50 is a plot of the variation of τ_{wx} in the streamwise direction at two different y locations. The agreement with other results is relatively good. Figure 51 is a plot of τ_{wy} versus x again at two different y locations. In this figure, the agreement with the small-disturbance interaction results of Edwards (1986) is very good, while those of Davis et al. (1986) differ considerably. Davis et al. (1986) believed that the discrepancy in the two results was caused by the grid spacing, though no conclusive studies are available for explaining the discrepancy. It should be noted that it is difficult to study the effect of grid spacing in three-dimensional problems even with the supercomputers available today. As for the inviscid case, grid effects were examined by halving the number of points in the y direction. Once again, there was little or no difference in the results, and hence detailed comparisons are not presented here.

Further comparisons between the two solutions (boundary-layer and dual potential) are presented by plotting the velocity profiles from both the dual potential and the boundary layer solutions in Figures 52 through 54. Figure 52 is a plot of the u velocity profiles in the plane of symmetry at different x locations. The growth of the boundary layer and the effect of the adverse pressure gradient near the center of the trough are visible in this figure. The dual potential and boundary-layer profiles show very good agreement. Detailed plots are given in Figures 53 and 54 which are plots of the velocity profiles in the maximum trough depth region at two different y planes. Again the agreement between the two solutions is relatively good. The no-slip boundary condition is not imposed on the vector potential functions directly and there is a small slip velocity in the dual potential profiles of the order of 2% of the free stream velocity. This error is partially geometric in origin, produced by the

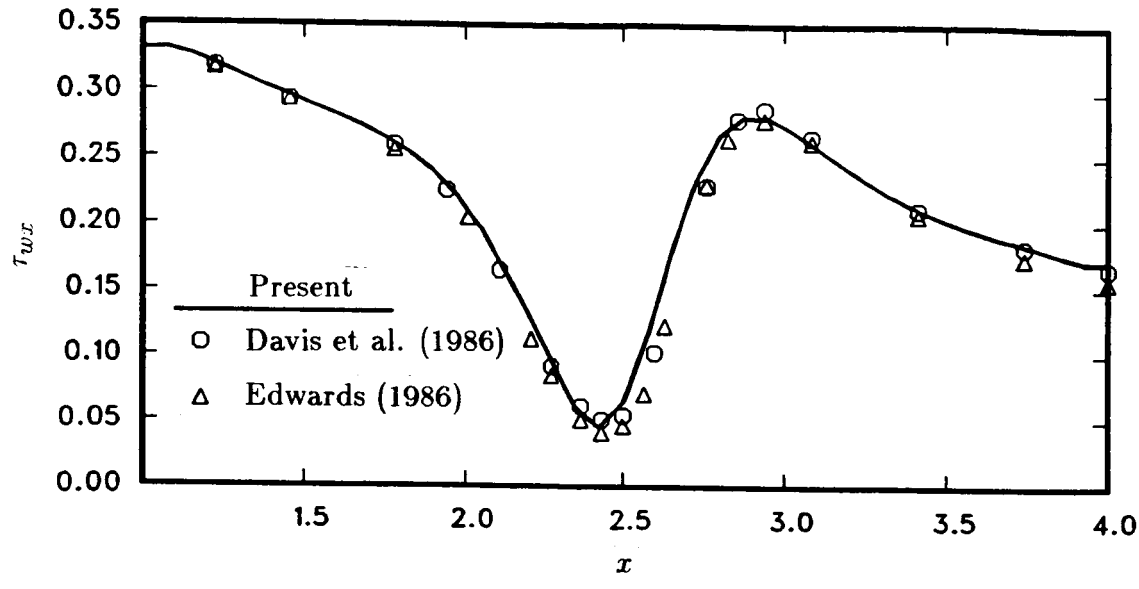

(a)

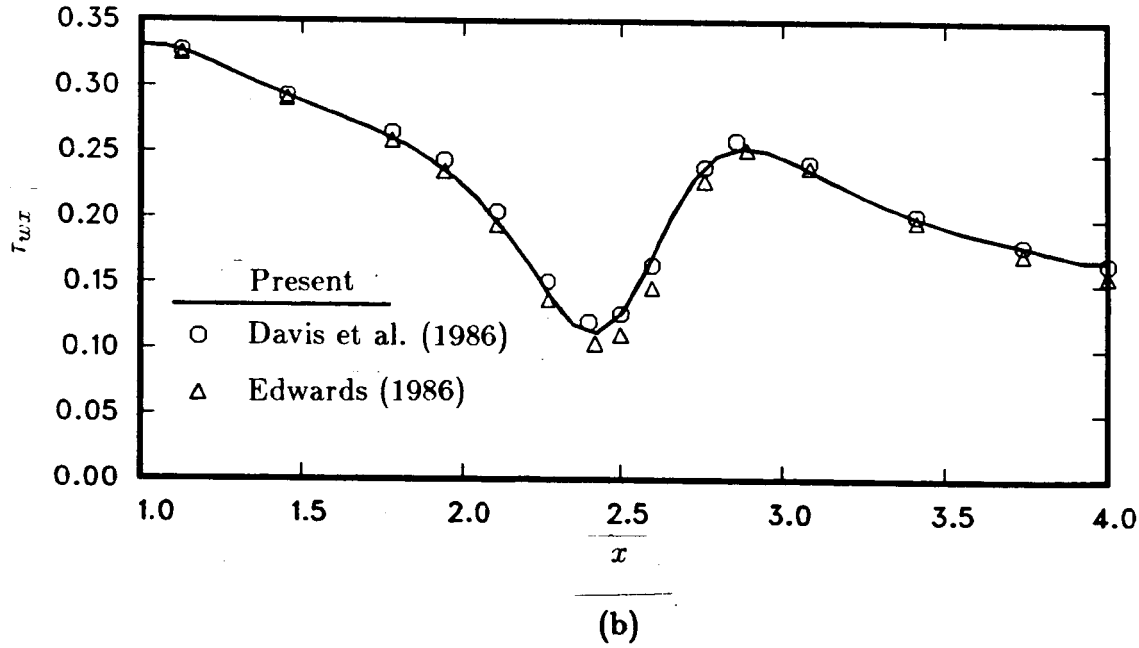

(b)

Figure 50. Comparison of the x-component of wall shear stress, $t = 0.03$. a) $y = 1.5$; b) $y = 1.2$

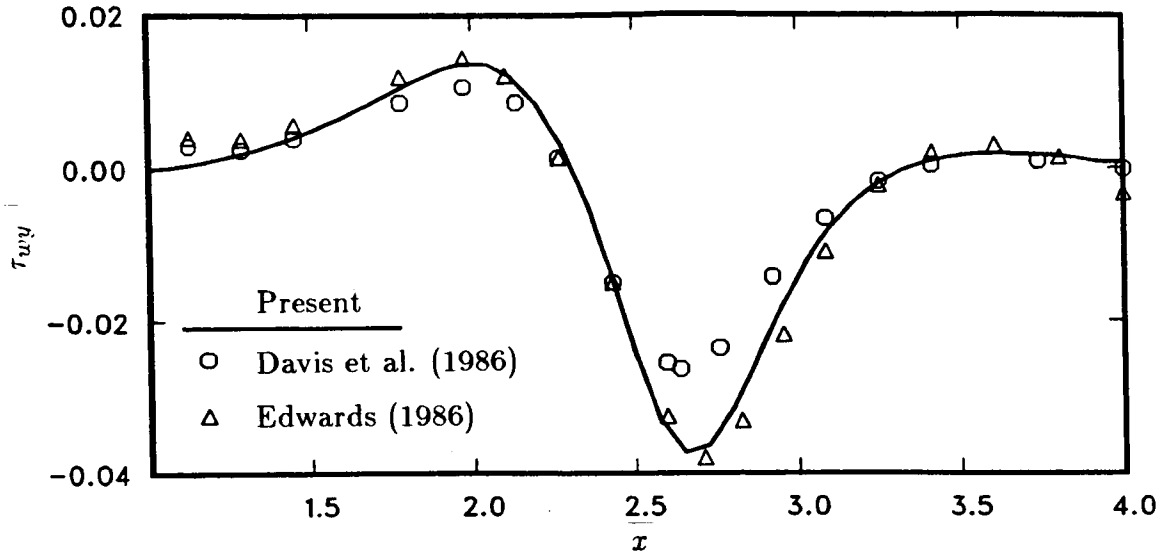

(a)

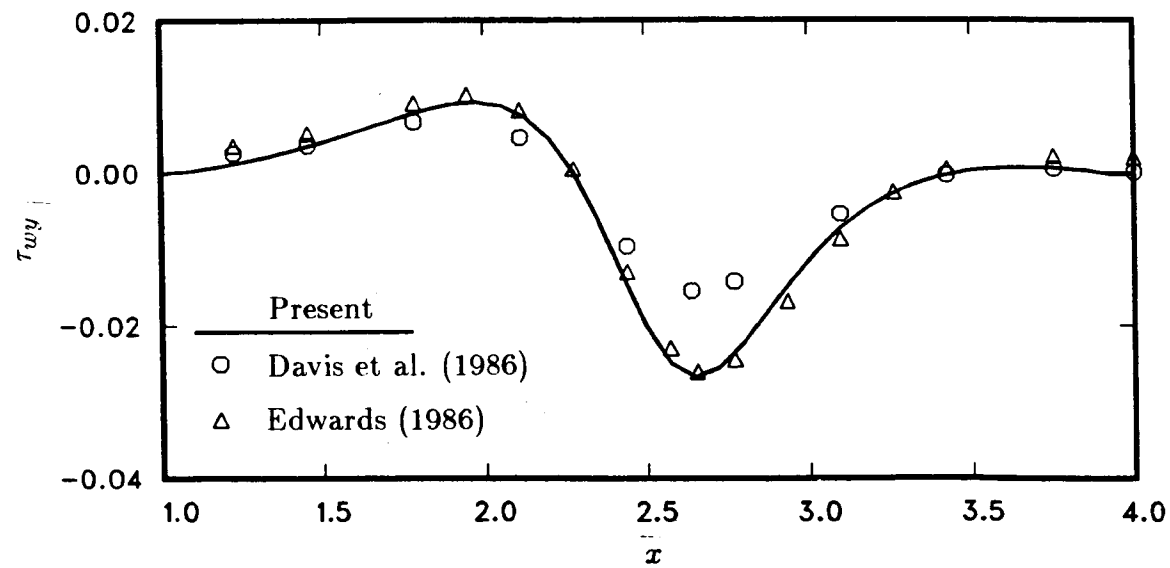

(b)

Figure 51. Comparison of the y-component of wall shear stress, $t = 0.03$. a) $y = 1.2$; b) $y = 0.9$

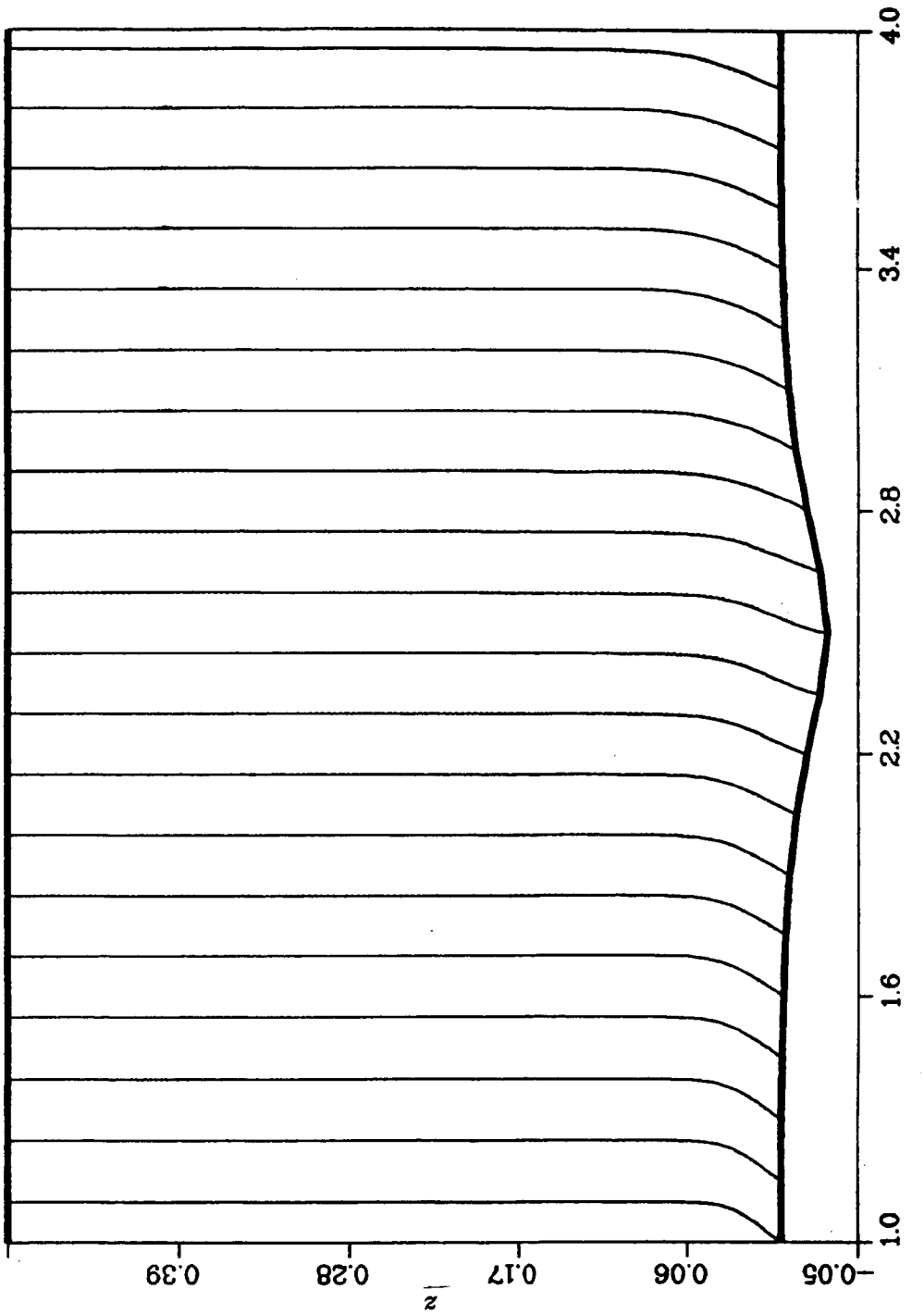

Figure 52. Velocity profiles from the dual potential and boundary-layer solutions at plane of symmetry ($y = 1.5$), $t = 0.03$, ——— dual potential; ..... boundary-layer

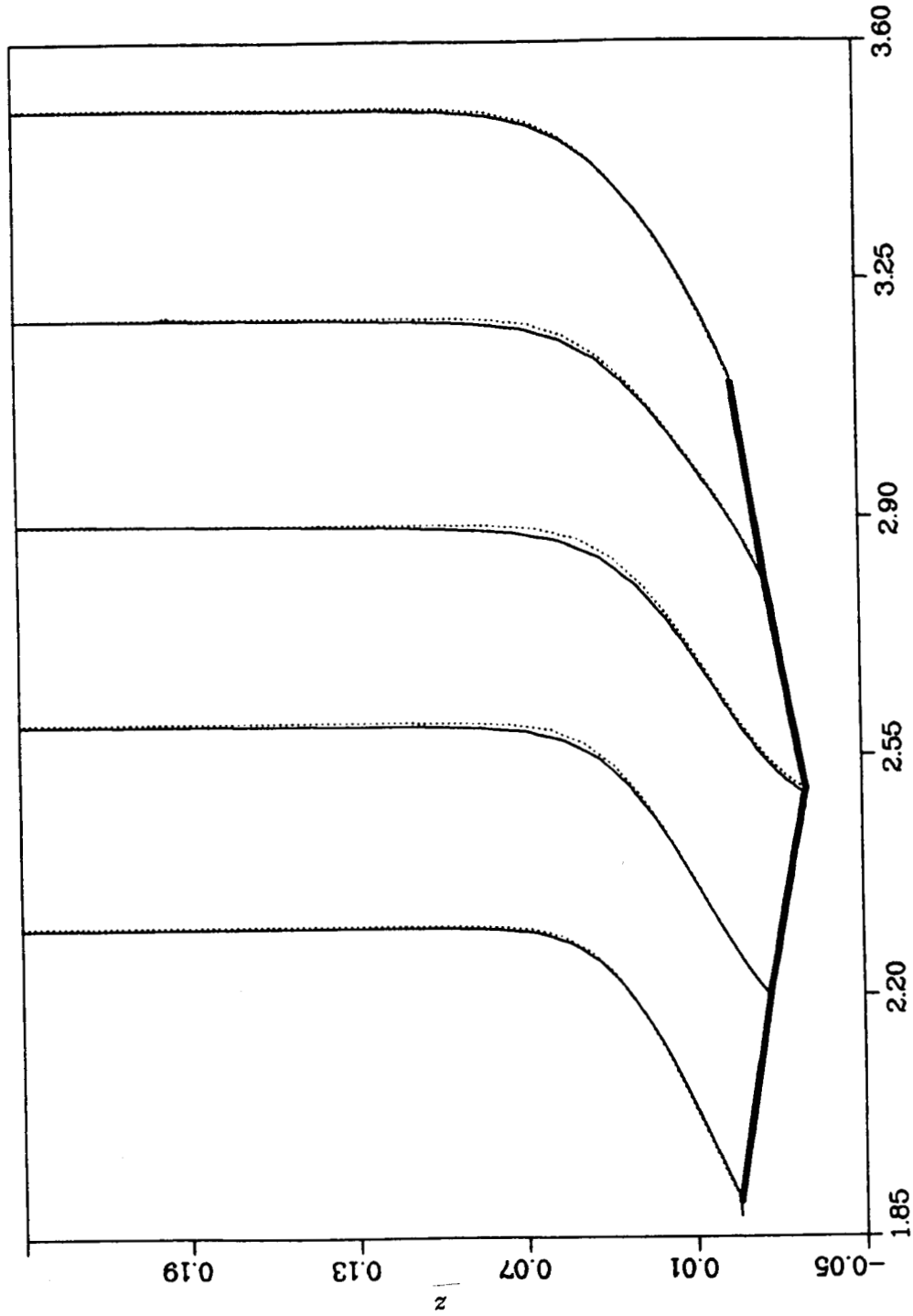

Figure 53. Comparison of u-velocity profiles from the dual potential and boundary-layer solutions at $y = 1.5$, $t = 0.03$, ——— dual potential; ..... boundary-layer

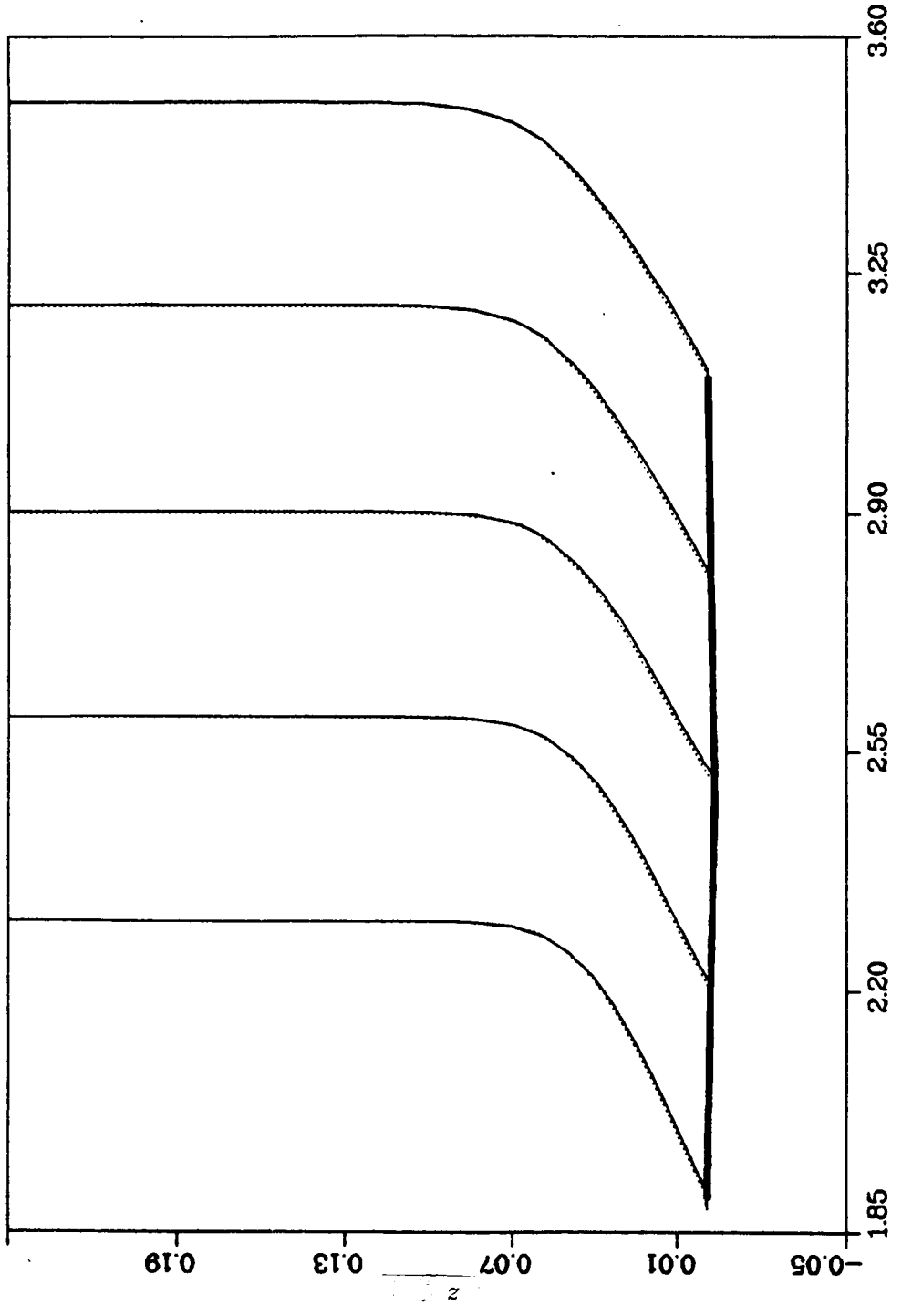

Figure 54. Comparison of u-velocity profiles from the dual potential and boundary-layer solutions at $y = 0.75$, $t = 0.03$, ——— dual potential; ..... boundary-layer

highly stretched grids which need to be used in the z-direction. A one-dimensional analysis of the cause of this error is given in Appendix A. Another possible source of error is interpolation errors due to the different grids used in the two schemes.

The three-dimensional interaction calculations required approximately 1400 iterations which took about 2500 seconds on the CRAY XMP. The iterative procedure was terminated when the residuals for both the dual potential and the boundary-layer algorithms had dropped by at least six orders of magnitude. As a practical convergence criteria of this method, the calculation was assumed to be converged when the relative changes in the pressures and the wall shear stress was less than 10^{-4} between successive iterations. The calculations were performed in the direct mode for the boundary-layer algorithm. Essentially the same solutions were obtained by using the inverse mode. However, the calculations in the inverse mode required more iterations.

The results described in this section show that the dual potential formulation, when coupled with an appropriate boundary-layer algorithm, can be used for solving three-dimensional viscous flow problems in which the viscous layer remains thin as in the case of attached flow.

V. CONCLUSIONS

A. Concluding Remarks

A dual potential decomposition scheme has been devised for computing three-dimensional rotational flows. With this formulation, rotational effects can be studied by adding the appropriate vorticity into the governing equations for the vector potential functions.

In the first part of this study, a finite-difference procedure for solving the dual potential equations has been developed and applied for calculating the inviscid but rotational flow through indraft wind tunnels, including the effects of screens and vanes. Actuator disk theory was used to model the stagnation pressure loss produced by flow straightening devices such as screens and vanes which are located at the inlet entrance. In particular, the flow through the 80- by 120-ft wind tunnel at the NASA Ames Research Center was successfully simulated using semi-empirical loss-coefficients to account for the pressure drop across the screens and vanes and the turning effect of these devices. The procedure was applied to compute the flow for two different inlet vane and screen configurations. The numerical solutions were in satisfactory agreement with experimental and other numerical results. With the use of this procedure, the relative effect of various passage geometries, flow straightening devices, and external wind conditions on test-section flow quality can be studied.

In the second part, viscous effects were modeled by adding vorticity in the boundary-layer region. This vorticity was obtained through a suitable boundary-layer interaction procedure. The numerical results obtained for attached flow over a three-dimensional trough compared favorably with other numerical solutions. For

separated flow, the numerical results indicate that the present formulation of the dual potential - boundary layer interaction procedure fails to converge. For two-dimensional separated flows, the dual potential form of the Navier-Stokes equations was solved using a prescribed vorticity boundary condition. A comparison of the vorticities from the boundary-layer and the Navier-Stokes solutions indicates that for the type of interaction considered in this study, the boundary-layer solution does not give a representation of the vorticity which is consistent with the dual potential formulation in regions where the boundary-layer is relatively thick as in separated flow.

Overall, a versatile and flexible tool has been developed by which it is possible to simulate a wide variety of flows with little or no changes to the numerical algorithm. In particular, it is possible to study rotational effects by adding the appropriate vorticity into the governing dual potential formulation.

B. Recommendations for Future Study

The dual potential velocity decomposition has been shown to be a viable alternative to primitive variable formulations for solving many three-dimensional flow problems. In this study, the formulation was used to develop a procedure for computing both inviscid and viscous flows with relatively small changes in the algorithms.

The dual potential formulation has already been applied successfully, in two dimensions to compute the inviscid transonic flow over airfoils (Chaderjian and Steger, 1985). The extension to transonic flow in three dimensions seems straightforward and needs to be implemented. While the present procedure has been successfully used to compute three-dimensional attached viscous flow, and some of the problems

associated with separated flow have been addressed in this study, the issue of separated flow remains an unsolved problem. In the interaction procedure used in this study, the boundary-layer equations were solved in the primitive variable form. It would perhaps be advantageous to use a vorticity/stream-function formulation of the boundary-layer equations in an alternate interaction procedure.

The dual potential formulation has not been clearly understood or developed for unsteady, compressible flows, even in two dimensions. Hence, further work remains to be done in extending the formulation to these more complex flows.

Finally, the treatment of turbulent flows is still one of the unsolved problems in fluid mechanics today. The use of the dual potential formulation for investigating turbulent flows needs to be examined; in particular, the selection of vorticity as the dependent variable in this formulation may have some advantages in this regard.

VII. REFERENCES

Anderson, D. A., Tannehill, J. C. and Pletcher, R. H. (1984). *Computational Fluid Mechanics and Heat Transfer.* New York: McGraw-Hill.

Aris, R. (1962). *Vectors, Tensors and the Basic Equations of Fluid Mechanics.* New York: Prentice-Hall.

Aregbesola, Y. A. S. and Burley, D. M. (1977). "The Vector and Scalar Potential for the Numerical Solution of Two- and Three-Dimensional Navier-Stokes Equations." *J. Computational Physics,* **24**, 398-415.

Atkins, H. L. and Hassan, H. A. (1983). "A New Stream Function Formulation For the Euler Equations." AIAA Paper 83-1947, Danvers, Massachusetts.

Aziz, K. and Hellums, J. D. (1967). "Numerical Solution of the Three-Dimensional Equations of Motion for Laminar Natural Convection." *Phys. Fluids,* **10**, 314-325.

Ballhaus, W. F., Jameson, A. and Albert, J. (1978). "Implicit Approximate Factorization Schemes for the Efficient Solution of Steady Transonic Flow Problems." *AIAA J.*, **16**, 573-579.

Beam, R. M. and Warming, R. F. (1976). "An Implicit Finite-Difference Algorithm for Hyperbolic Systems in Conservation-Law Form." *J. Computational Physics,* **22**, 87-110.

Bridgeman, J. O., Steger, J. L. and Caradonna, F. X. (1982). "A Conservative Finite Difference Algorithm for the Unsteady Transonic Potential Equation in Generalized Coordinates." AIAA Paper 82-1388, San Diego, California.

Briley, W. R. and McDonald, H. (1977). "Solution of the Multidimensional Compressible Navier-Stokes Equations by a Generalized Implicit Method." *J. Computational Physics,* **24**, 372-397.

Brown, S. N. and Stewartson, K. (1969). "Laminar Separation." *Ann. Rev. Fluid Mech.,* **1**, 1-28.

Buneman, O. (1981). "Compressible Flow Simulation Using Hamilton's Equations and Clebsch-type Vortex Parameters." *Lecture Notes in Physics,* **141**, 103-108.

Carter, J. E. and Wornum, S. F. (1975). "Solutions for Incompressible Separated Boundary Layers Including Viscous-Inviscid Interaction." *Aerodynamic Analyses Requiring Advanced Computers - Part I.* NASA SP-347, 125-150.

Catherall, D. and Mangler, K. W. (1966). "The Integration of the Two-Dimensional Laminar Boundary-Layer Equations Past the Point of Vanishing Skin Friction." *J. Fluid Mechanics,* **26**, 163-182.

Chaderjian, N. M. (1984). "The Numerical Simulation of Steady Transonic Rotational Flow Using a Dual Potential Formulation." Ph. D. Thesis, Stanford University, Stanford, California.

Chaderjian, N. M. and Steger, J. L. (1983). "A Zonal Approach for the Steady Transonic Simulation of Inviscid Rotational Flow." AIAA Paper 83-1927, Danvers, Massachusetts.

Chaderjian, N. M. and Steger, J. L. (1985). "The Numerical Simulation of Steady Transonic Rotational Flow using a Dual Potential Formulation." AIAA Paper 85-0368, Reno, Nevada.

Chang, S-C. and Adamczyk, J. J. (1983). "A Semi-Direct Solver for Compressible Three-Dimensional Rotational Flow." AIAA Paper 83-1909, Danvers, Massachusetts.

Chaviaropoulos, P., Giannakoglou, K. and Papailiou, K. D. (1986). "Numerical Computation of Three-Dimensional Rotational Inviscid Subsonic Flows, Using the Decomposition of the Flow Field Into a Potential and a Rotational Part." ASME Paper 86-GT-169, Dusseldorf, W. Germany.

Cousteix, J. and Houdeville, R. (1981). "Singularities in Three-Dimensional Turbulent Boundary-Layer Calculations and Separation Phenomena." *AIAA J.,* **19**, 976-985.

Davis, R. L., Carter, J. E. and Hafez, M. (1986). "Three-Dimensional Viscous Flow Solutions With a Vorticity-Stream Function Formulation." AFOSR-TR-86 (see also AIAA Paper 87-0601, Reno, Nevada).

Delery, J. M. and Formery, M. J. (1983). "A Finite-Difference Method for Inverse Solutions of Three-Dimensional Turbulent Boundary-Layer Flow." AIAA Paper 83-0301, Reno, Nevada.

Der Jr., J. and Raetz, G. S. (1962). "Solution of General Three-Dimensional Laminar Boundary Layer Problems by an Exact Numerical Method." *Institute of The Aerospace Sciences*, Paper 62-70. New York, New York.

Dwyer, H. A. (1968). "Solution of a Three-Dimensional Boundary-Layer Flow with Separation." *AIAA J.*, **6**, 136-142.

Edwards, D. E. (1986). "Analysis of 3-D Separated Flow Using Interacting Boundary-Layer Theory." *IUTAM Symposium on Boundary Layer Separation*, London, England.

Edwards, D. E. and Carter, J. E. (1985). "Analysis of Three-Dimensional Separated Flow with the Boundary-Layer Equations." AIAA Paper 85-1499, Cincinnati, Ohio.

Emmons, H. W. (1948). "Flow of a Compressible Fluid Past a Symmetrical Airfoil in a Wind Tunnel and in Free Air." NACA TN 1746.

Flores, J., Reznick, S. G., Holst, T. L. and Gundy, K. (1987). "Transonic Navier-Stokes Solutions for a Fighter-Like Configuration." AIAA Paper 87-0032, Reno, Nevada.

Goble, B. D. and Fung, K-Y. (1987). "A Truncation Error Injection Approach to Viscous-Inviscid Interaction." AIAA Paper 87-540, Reno, Nevada.

Goldstein, S. (1948). "On Laminar Boundary Layer Flow Near a Position of Separation." *Q. J. Mech. Appl. Math.*, **1**, 43-69.

Grossman, B. (1983). "The Computation of Inviscid Rotational Gasdynamic Flows Using an Alternate Velocity Decomposition." AIAA Paper 83-1900, Danvers, Massachusetts.

Hafez, M., Habashi, W. G., Przybytkowski, S. M. and Peeters, M. F. (1987). "Compressible Viscous Internal Flow Calculations by a Finite Element Method." AIAA Paper 87-0644, Reno, Nevada.

Hafez, M. and Lovell, D. (1981). "Numerical Solution of Transonic Stream Function." AIAA Paper 81-1017, Palo Alto, California.

Hafez, M. and Lovell, D. (1983). "Entropy and Vorticity Corrections for Transonic Flows." AIAA Paper 83-1926, Danvers, Massachusetts.

Halim, A. and Hafez, M. (1984). "Calculations of Separation Bubbles Using Boundary-Layer-Type Equations - Part I & II." AIAA Paper 84-1585, Snowmass, Colorado.

Hindman, R. D. (1981). "Geometrically Induced Errors and Their Relationship to the Form of the Governing Equations and the Treatment of Generalized Mappings." *AIAA J.*, **20**, 1359-1367.

Hirasaki, G. J. and Hellums, J. D. (1967). "A General Formulation of the Boundary Conditions on the Vector Potential in Three-Dimensional Hydrodynamics." *Q. Appl. Math.*, **26**, 331-342.

Hirasaki, G. J. and Hellums, J. D. (1970). "Boundary Conditions on the Vector and Scalar Potentials in Viscous Three-Dimensional Hydrodynamics." *Q. Appl. Math.*, **28**, 293-296.

Holst, T. L. (1987). "Numerical Solution of the Navier-Stokes Equations About Three-Dimensional Configurations - A Survey." *Supercomputing in Aerospace.* NASA CP 2454, 281-298.

Horlock, J. H. (1978). *Actuator Disk Theory.* London: McGraw-Hill.

Kaul, U. K., Ross, J. C. and Jacocks, J. L. (1985). "A Numerical Simulation of the NFAC (National Full-Scale Aerodynamics Complex) Open-Return Wind Tunnel Inlet Flow." AIAA Paper 85-0437, Reno, Nevada.

Kitchens, Jr., C. W., Sedney, R. and Gerber, N. (1975). "The Role of the Zone of Dependence Concept in Three-Dimensional Boundary-Layer Calculations." *Proc. AIAA 2nd Computational Fluid Dynamics Conference*, Hartford, Connecticut.

Klineberg, J. M. and Steger, J. L. (1974). "On Laminar Boundary-Layer Separation." AIAA Paper 74-94, Washington, D. C.

Krause, E., Hirschel, E. H. and Kordulla, W. (1976). "Fourth Order "Mehrstellen"-Integration of Three-Dimensional Turbulent Boundary Layers." *Computers and Fluids*, **4**, 77-92.

Kwon, O. K. and Pletcher, R. H. (1979). "Prediction of Subsonic Separation Bubbles on Airfoils by Viscous-Inviscid Interaction." *J. Fluids Engineering*, **101**, 466-472.

Lee, D-S. and Pletcher, R. H. (1986). "Application of Viscous-Inviscid Interaction Methods to Transonic Turbulent Flows." Iowa State University, Report HTL-42, CFD-16, ISU-ERI-Ames-87055.

Lighthill, M. J. (1958). "On Displacement Thickness." *J. Fluid Mechanics,* **4**, 383-392.

Lock, R. C. (1981). "A Review of Methods for Predicting Viscous Effects on Aerofoils and Wings at Transonic Speeds." AGARD CP-291, Paper 2, Colorado Springs, Colorado.

MacCormack, R. W. (1982). "A Numerical Method for Solving the Equations of Compressible Viscous Flow." *AIAA J.*, **20**, 1275-1281.

Mallinson, G. D. and de Vahl Davis, G. (1973). "The Method of the False Transient for the Solution of Coupled Elliptic Equations." *J. Computational Physics*, **12**, 435-461.

McDonald, H. and Briley, W. R. (1983). "A Survey of Recent Work on Interacted Boundary-Layer Theory for Flow with Separation." *Numerical and Physical Aspects of Aerodynamic Flows II*, pp. 141-162. (T. Cebeci, Ed.), New York: Springer-Verlag.

Melnik, R. E. (1981). "Turbulent Interaction on Aerofoils at Transonic Speeds - Recent Developments." AGARD CP-291, Paper 10, Colorado Springs, Colorado.

Moore, F. K. (1953). "Displacement Effect of a Three-Dimensional Boundary Layer." NACA Report No. 1124.

Morino, L. (1985). "Scalar/Vector Potential Formulation for Compressible Viscous Unsteady Flows." NASA CR 3921.

Orszag, S. A. and Israeli, M. (1974). "Numerical Simulation of Viscous Incompressible Flows." *Ann. Rev. Fluid Mech.*, **6**, 281-318.

Ozoe, H., Chao, P. K., Churchill, S. W. and Lior, N. (1982). "Laminar Natural Convection in an Inclined Rectangular Box with the Lower Surface Half Heated and Half Insulated." ASME Paper 82-HT-72, St. Louis, Missouri.

Ozoe, H., Yamamoto, K., Churchill, S. W. and Sayama, H. (1976). "Three-Dimensional Numerical Analysis of Laminar Natural Natural Convection

Patterns in a Confined Fluid Heated From Below." *J. Heat Transfer,* **98**, 202-207.

Ozoe, H., Yamamoto, K., Sayama, H. and Churchill, S. W. (1977). "Natural Convection Patterns in a Long Inclined Rectangular Box Heated From Below. Part II. Three-Dimensional Numerical Results." *Int. J. Heat Mass Transfer,* **20**, 131-139.

Panton, R. L. (1984). *Incompressible Fluid Flow.* New York: Academic Press.

Pulliam, T. H. (1985). "Artificial Dissipation Models for the Euler Equations." AIAA Paper 85-0438, Reno, Nevada.

Pulliam, T. H. and Steger, J. L. (1980). "Implicit Finite-Difference Simulations of Three-Dimensional Compressible Flow." *AIAA J.,* **18**, 159-167.

Radwan, S. F. and Lekoudis, S. G. (1984). "Boundary-Layer Calculations in the Inverse Mode for Compressible Flows over Infinite Swept Wings." *AIAA J.,* **22**, 737-743.

Richardson, S. M. and Cornish, A. R. H. (1977). "Solution of Three-Dimensional Incompressible Flow Problems." *J. Fluid Mechanics,* **82**, 309-319.

Roache, P. J. (1972). *Computational Fluid Dynamics.* New Mexico: Hermosa Publishers.

Ross, J. C., Olsen, L. E., Meyn, L. A. and van Aken, J. M. (1986). "A New Design Concept for Indraft Wind-Tunnel Inlets with Application to the National Full-Scale Aerodynamics Complex." AIAA Paper 86-0043, Reno, Nevada.

Schlicting, H. (1979). *Boundary-Layer Theory.* 7th ed. Translated by J. Kestin. New York: McGraw-Hill.

Shang, J. (1985). "An Assessment of the Numerical Solutions of the Compressible Navier-Stokes Equations." *J. Aircraft,* **22**, 353-370.

Shang, J. and Scherr, S. J. (1986). "Numerical Simulation of the Flow Field Around a Complete Aircraft." *Applications of Computational Fluid Dynamics in Aeronautics,* AGARD-CP-412, Paper No. 32.

Sherif, A. and Hafez, M. (1983). "Computation of Three Dimensional Transonic Flows Using Two Stream Functions." AIAA Paper 83-1948, Danvers, Massachusetts.

Steger, J. L. (1978). "Implicit Finite-Difference Simulation of Flow About Arbitrary Two-Dimensional Geometries." *AIAA J.*, **16**, 679-686.

Steger, J. L. and Van Dalsem, W. R. (1985). "Developments in the Simulation of Separated Flows Using Finite-Difference Methods." *Proc. Third Numerical and Physical Aspects of Aerodynamic Flows*, Long Beach, California.

Thomas, P. D. and Lombard, C. K. (1978). "The Geometric Conservation Law – A Link Between Finite-Difference and Finite Volume Methods of Flow Computation on Moving Grids." AIAA Paper 78-1208, Seattle, Washington.

van Aken, J. M. (1986). "Experimental Investigation of Several Inlet Flow Cascades for the NFAC 80- by 120-Foot Indraft Wind Tunnel." KU-CRINC Rept. 6900-2, University of Kansas Center for Research, Inc., Lawrence, Kansas.

Van Dalsem, W. R. and Steger, J. L. (1983). "Finite-Difference Simulation of Transonic Separated Flow Using a Full Potential Boundary Layer Interaction Approach." AIAA Paper 83-1689, Danvers, Massachusetts.

Van Dalsem, W. R. and Steger, J. L. (1985). "The Efficient Simulation of Separated Three-Dimensional Viscous Flows Using the Boundary-Layer Equations." AIAA Paper 85-4064, Colorado Springs, Colorado.

Van Dalsem, W. R. and Steger, J. L. (1986a). "Using the Boundary-Layer Equations in Three-Dimensional Viscous Flow Simulation." NASA TM 88241.

Van Dalsem, W. R. and Steger, J. L. (1986b). "The Fortified Navier-Stokes Approach." *Workshop on Computational Fluid Dynamics*, University of California, Davis.

Veldman, A. E. P. (1981). "New Quasi-Simultaneous Method to Calculate Interacting Boundary Layers." *AIAA J.*, **19**, 79-85.

Vinokur, M. (1983). "On One-Dimensional Stretching Functions for Finite-Difference Calculations." *J. Computational Physics*, **50**, 215-234.

Vinokur, M. (1986). "An Analysis of Finite-Difference and Finite-Volume Formulations of Conservation Laws." NASA CR 177416.

White, F. M. (1974). *Viscous Fluid Flow.* New York: McGraw-Hill.

Whitfield, D. L. (1985). "Viscous-Inviscid Interaction Computations Using a Pseudo Navier-Stokes Approach." *Proc. Third Symposium on Numerical and Physical Aspects of Aerodynamic Flows*, Long Beach, California.

Whitfield, D. L., Swafford, T. M. and Jacocks, J. L. (1981). "Calculation of Turbulent Boundary Layers with Separation and Viscous-Inviscid Interaction." *AIAA J.*, **19**, 1315-1322.

Wigton, L. B. and Yoshihara, H. (1983). "Viscous-Inviscid Interaction with a Three-Dimensional Inverse Boundary Layer Code." *Proc. Second Symposium on Numerical and Physical Aspects of Aerodynamic Flows*, Long Beach, California.

Williams, P. G. (1975). "A Reverse Flow Computation in the Theory of Self-Induced Separation." *Lecture Notes in Physics*, **35**, 445-451.

Wong, A. K. and Reizes, J. A. (1984). "An Effective Vorticity-Vector Potential Formulation for the Numerical Solution of Three-Dimensional Duct Flow Problems." *J. Computational Physics*, **55**, 98-114.

Wong, A. K. and Reizes, J. A. (1986). "The Vector Potential in the Numerical Solution of Three-Dimensional Fluid Dynamics Problems in Multiply Connected Regions." *J. Computational Physics*, **62**, 124-142.

Yang, H. and Camarero, R. (1986). "An Improved Vorticity-Potential Method for Three-Dimensional Duct Flow Problems." *Int. J. Num. Meth. Fluids*, **6**, 35-45.

VIII. ACKNOWLEDGMENTS

The authors gratefully acknowledge the support provided for this study by NASA Ames Research Center under Interchange No. NCA2-17.

VIII. APPENDIX A: GEOMETRIC ERRORS

In this appendix, the geometric errors introduced by using stretched grids in the computational domain will be analyzed by considering a one-dimensional model problem of the vorticity/stream-function case.

Consider Laplace's equation in one dimension

$$\psi_{yy} = 0; \quad u = \psi_y \tag{A.1}$$

solved on a simple geometrically stretched grid defined by

$$dy(k) = \epsilon^{k-1} dyo; \quad k = 1, \ldots, KMAX - 1 \tag{A.2}$$

where $dy(k) = y(k+1) - y(k)$. and $KMAX$ is the total number of points. $\psi = y$ is a solution of this equation for the boundary conditions

$$\text{at } y = 0 : \psi = 0; \qquad \text{at } y = ymax : \psi_y = 0 \tag{A.3}$$

When the domain is transformed into a uniformly spaced computational domain defined by $\eta = \eta(y)$, the governing equation (A.1) is transformed as

$$\frac{d}{d\eta}\left(\frac{\eta_y^2}{J}\frac{d\psi}{d\eta}\right) = 0 \tag{A.4}$$

where J is the Jacobian of the transformation defined as

$$J = 1/y_\eta \tag{A.5}$$

and

$$\eta_y = 1/y_\eta \tag{A.6}$$

In the discretized domain, the left-hand-side (LHS) of equation (A.4) is approximated as

$$\begin{aligned} LHS = & \frac{1}{4}(y_{\eta_k} + y_{\eta_{k+1}})\left(\frac{1}{y_{\eta_k}^2} + \frac{1}{y_{\eta_{k+1}}^2}\right)(\psi_{k+1} - \psi_k) \\ & - \frac{1}{4}(y_{\eta_k} + y_{\eta_{k-1}})\left(\frac{1}{y_{\eta_k}^2} + \frac{1}{y_{\eta_{k-1}}^2}\right)(\psi_k - \psi_{k-1}) \end{aligned} \tag{A.7}$$

The metric quantities for this case can be calculated analytically for the particular stretching form that is used as shown below

k	y	y_η
1	$y_1 = 0$	$y_{\eta_1} = y_2 - y_1 = dyo$
2	$y_2 = dyo$	$y_{\eta_2} = \frac{1}{2}(y_3 - y_1) = \frac{1}{2}dyo(1+\epsilon)$
3	$y_3 = dyo(1+\epsilon)$	$y_{\eta_3} = \frac{1}{2}(y_4 - y_2) = \frac{1}{2}\epsilon dyo(1+\epsilon)$
4	$y_4 = dyo(1+\epsilon+\epsilon^2)$	$y_{\eta_4} = \frac{1}{2}(y_5 - y_3) = \frac{1}{2}\epsilon^2 dyo(1+\epsilon)$
5	$y_5 = dyo(1+\epsilon+\epsilon^2+\epsilon^3)$	

(A.8)

Setting $\psi = y$ and substituting the various terms in equation (A.7) for different values of k the left-hand-side can be evaluated exactly. For $k = 3, 4, \ldots, KMAX-2$ it can be shown that $LHS = 0$, and hence the analytical solution satisfies the numerical approximation exactly for any values of the stretching parameter ϵ. However, for $k = 2$, and for $k = KMAX - 1$, LHS is not zero but is evaluated as

$$LHS_{l=2} = \frac{1}{2}\epsilon\left(1 + \frac{1}{\epsilon^2}\right) - \frac{1}{8}\frac{(3+\epsilon)(\epsilon^2+2\epsilon+5)}{(1+\epsilon^2)} \tag{A.9}$$

In this case, $LHS = 0$ if, and only if, $\epsilon = 1$ which corresponds to a uniform mesh.

The geometric errors introduced in the computation domain for the case of the simple geometric stretching have been analyzed above. The exact nature of the error would depend on the type of grid used. This kind of error has been analyzed by others (*cf.* Hindman, 1981; Thomas and Lombard, 1978). It has been shown that

the error is localized to the boundary points for the kind of stretching considered here. This error is demonstrated in a solution of the one-dimensional homogeneous problem which is presented in Figure A1. Figure A1 is a plot of 'velocity' ($u = \psi_y$) versus y for the case in which $ymax = 5.0$, $KMAX = 81$, $dyo = 0.0001$. From the figure it can be seen that the error is localized and does not affect the solution for the interior points. In particular, when the nonhomogeneous Poisson equation is solved for boundary-layer type vorticity, the error is manifested as a small slip velocity as shown in Figures A2 and A3. In this case, the equation $\psi_{yy} = -\omega$ is solved where ω is computed from a polynomial equation for Blasius flow with a boundary-layer thickness of 0.02. The slip velocity at the wall is of the order of 1.5% for this case.

One of the commonly used cures for this problem is the free stream subtraction concept introduced by Pulliam and Steger (1980) whereby an exact analytical solution of the governing differential equation for uniform flow is subtracted from the right-hand-side of the numerical approximation. Unfortunately, this technique requires the knowledge of an exact analytical solution which may not always be known.

Other solutions for this problem involve the computing of metrics in special ways or the use of special discretization formulas at boundaries (Vinokur, 1986).

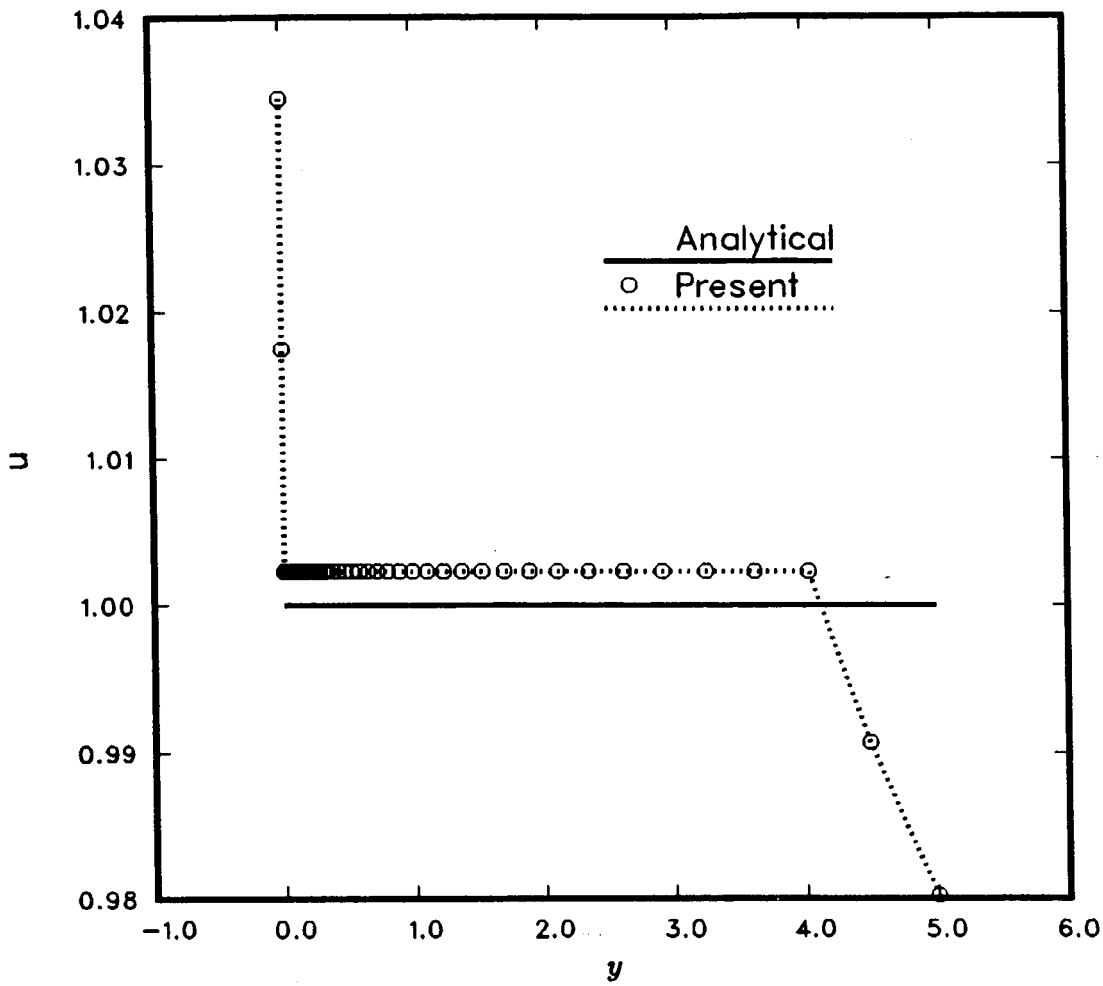

Figure A1. One-dimensional velocity profile for zero vorticity

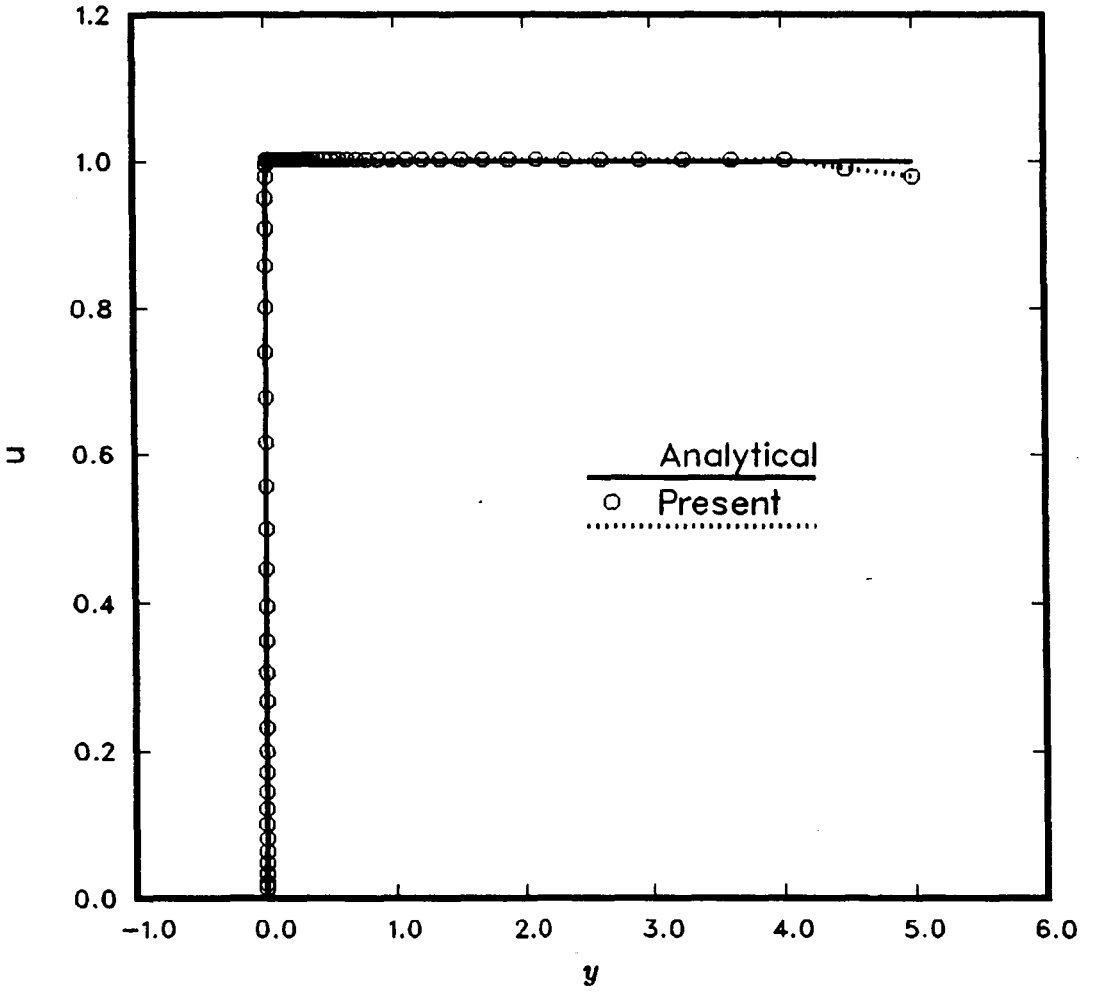

Figure A2. One-dimensional velocity profile for boundary-layer type vorticity

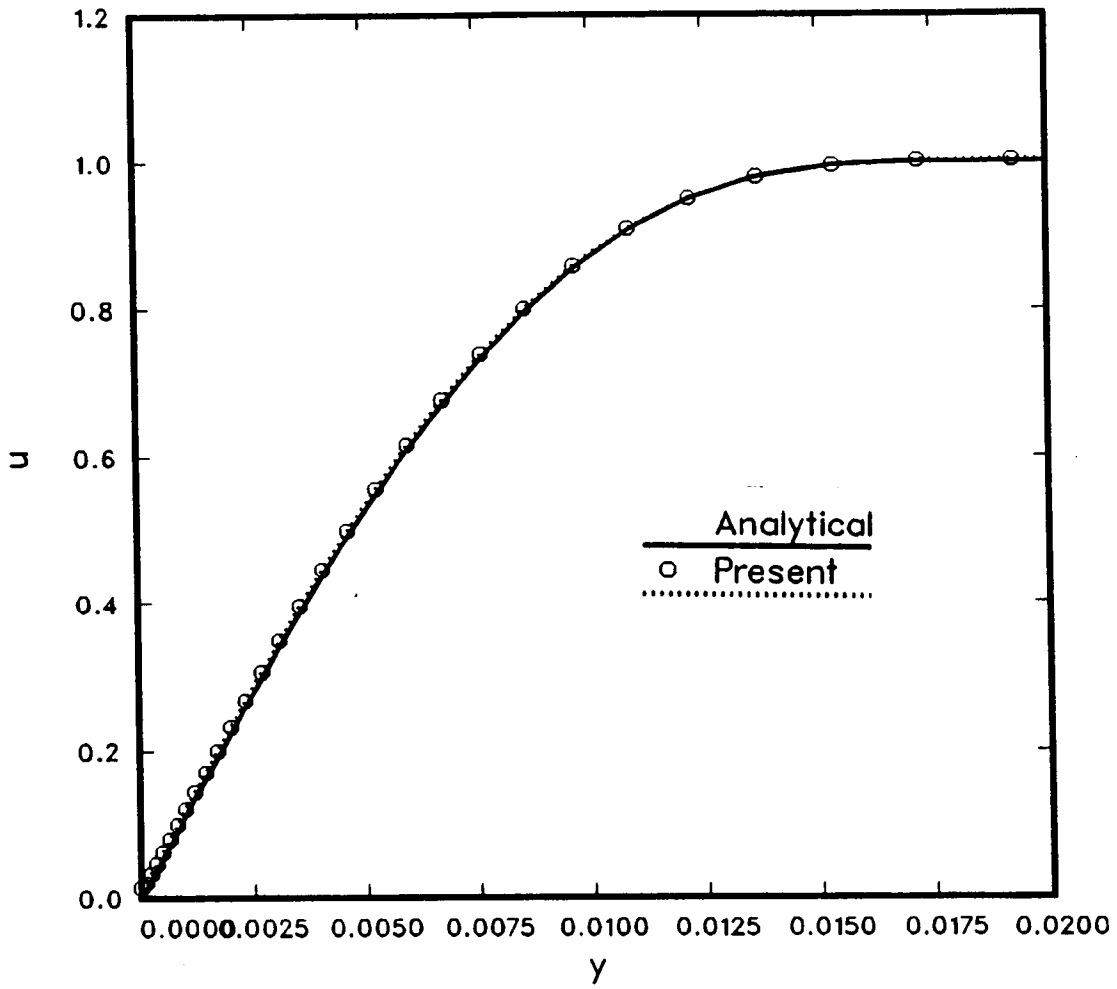

Figure A3. Detail of velocity profile for boundary-layer type vorticity

IX. APPENDIX B: TWO-DIMENSIONAL EQUATIONS

In this appendix, the governing equations, transformations and numerical algorithms for the two-dimensional incompressible dual potential and boundary-layer formulations which was used in §IV.C will be presented. The numerical algorithms are simplifications of the ones presented in Chapter III and hence some details may not be included here.

A. Dual Potential Form of Equations

1. Governing equations

For the dual potential decomposition given by

$$u = \phi_x - \chi_z; \quad w = \phi_z + \chi_x \tag{B.1}$$

the governing equations are given as

$$\phi_{xx} + \phi_{zz} = 0 \tag{B.2}$$

$$\chi_{xx} + \chi_{zz} = -\omega; \quad \omega = u_z - w_x \tag{B.3}$$

$$u\omega_x + w\omega_z = \frac{1}{Re}(\omega_{xx} + \omega_{zz}) \tag{B.4}$$

2. Transformation to general coordinates

Using a general coordinate transformation defined by

$$\xi = \xi(x, z), \quad \varsigma = \varsigma(x, z) \tag{B.5}$$

in terms of the independent variables ξ, ς, the Cartesian velocity components can be evaluated from the potential functions using the chain rule of partial differentiation

on equation (B.1) as

$$u = (\xi_x \phi_\xi + \varsigma_x \phi_\varsigma) - (\xi_z \chi_\xi + \varsigma_z \chi_\varsigma)$$
$$w = (\xi_z \phi_\xi + \varsigma_z \phi_\varsigma) + (\xi_x \chi_\xi + \varsigma_x \chi_\varsigma) \tag{B.6}$$

The metric quantities used in the above transformations are defined as

$$\xi_x = J z_\varsigma, \quad \xi_z = -J x_\varsigma$$
$$\varsigma_x = -J z_\xi, \quad \varsigma_z = J x_\xi \tag{B.7}$$

and J is the Jacobian of the transformation given by

$$J = \xi_x \varsigma_z - \xi_z \varsigma_x \tag{B.8}$$

Unscaled contravariant velocity components of the velocity vector $\vec{q}$ can be defined as

$$U = \xi_x u + \xi_z w$$
$$W = \varsigma_x u + \varsigma_z w \tag{B.9}$$

The contravariant velocity components are conveniently split between the scalar potential contribution and the vector potential contribution as

$$U = U^\phi + U^\chi$$
$$W = W^\phi + W^\chi \tag{B.10}$$

where

$$U^\phi = A^{\xi\xi} \phi_\xi + A^{\xi\varsigma} \phi_\varsigma$$
$$W^\phi = A^{\xi\varsigma} \phi_\xi + A^{\varsigma\varsigma} \phi_\varsigma$$
$$U^\chi = -J \chi_\varsigma$$
$$W^\chi = J \chi_\xi \tag{B.11}$$

and

$$A^{\xi\xi} = \nabla\xi \cdot \nabla\xi = \xi_x^2 + \xi_z^2$$
$$A^{\varsigma\varsigma} = \nabla\varsigma \cdot \nabla\varsigma = \varsigma_x^2 + \varsigma_z^2$$
$$A^{\xi\varsigma} = \nabla\xi \cdot \nabla\varsigma = \xi_x \varsigma_x + \xi_z \varsigma_z \tag{B.12}$$

3. Governing equations in transformed coordinates

The continuity equation can now be written in transformed coordinates as

$$\left[\frac{(A^{\xi\xi}\phi_\xi + A^{\xi\varsigma}\phi_\varsigma)}{J}\right]_\xi + \left[\frac{(A^{\xi\varsigma}\phi_\xi + A^{\varsigma\varsigma}\phi_\varsigma)}{J}\right]_\varsigma = 0 \qquad \text{(B.13)}$$

The Poisson equations for the stream function can be transformed similarly employing the same metric groupings and can be written as

$$\left[\frac{(A^{\xi\xi}\chi_\xi + A^{\xi\varsigma}\chi_\varsigma)}{J}\right]_\xi + \left[\frac{(A^{\xi\varsigma}\chi_\xi + A^{\varsigma\varsigma}\chi_\varsigma)}{J}\right]_\varsigma = -\frac{\omega}{J} \qquad \text{(B.14)}$$

while the vorticity transport equation (B.4) is written as

$$(U\omega_\xi + W\omega_\varsigma) = \frac{J}{Re}\left[\left(\frac{A^{\xi\xi}\omega_\xi + A^{\xi\varsigma}\omega_\varsigma}{J}\right)_\xi + \left(\frac{A^{\xi\varsigma}\omega_\xi + A^{\varsigma\varsigma}\omega_\varsigma}{J}\right)_\varsigma\right] \qquad \text{(B.15)}$$

4. Numerical algorithms

The continuity equation for ϕ, equation (B.2), is updated using an approximate factorization (ADI-type) algorithm in delta-form. The differencing scheme in AF form is given by

$$\begin{aligned}[I - h\bar{\delta}_\xi(\frac{A^{\xi\xi}}{J})^n\delta_\xi][I - h\bar{\delta}_\varsigma(\frac{A^{\varsigma\varsigma}}{J})^n\bar{\delta}_\varsigma](\phi^{n+1} - \phi^n) \\ = h\omega\left[\bar{\delta}_\xi(\frac{U^\phi}{J})^n + +\bar{\delta}_\varsigma(\frac{W^\phi}{J})^n - R_\infty\right]\end{aligned} \qquad \text{(B.16)}$$

The superscript n refers to the iteration level. The differencing of the contravariant velocity terms is illustrated by considering U^ϕ below

$$U^\phi_{j+\frac{1}{2}} = A^{\xi\xi}_{j+\frac{1}{2}}\Delta_\xi\phi_j + \frac{1}{2}\left(A^{\xi\varsigma}_{j+1}\delta_\varsigma\phi_{j+1} + A^{\xi\varsigma}_j\delta_\varsigma\phi_j\right) \qquad \text{(B.17)}$$

The free-stream subtraction term R_∞ appearing in the right-hand side of equation (B.16), accounts for incomplete metric cancellation and is given by

$$R_\infty = \bar{\delta}_\xi\left(\frac{U_\infty}{J}\right) + \bar{\delta}_\varsigma\left(\frac{W_\infty}{J}\right) \qquad \text{(B.18)}$$

An ADI algorithm is used to solve equation (B.16). Rewriting equation (B.16) in the form

$$L_\xi L_\varsigma(\phi^{n+1} - \phi^n) = R \tag{B.19}$$

the ADI algorithm is implemented in two steps as

$$\begin{aligned} L_\xi \Delta\phi^* &= R \\ L_\varsigma \Delta\phi^{n+1} &= \Delta\phi^* \\ \phi^{n+1} &= \phi^n + \Delta\phi^n \end{aligned} \tag{B.20}$$

The algorithm given by equation (B.19) requires only a series of scalar, tridiagonal inversions and is, therefore, solved efficiently.

The Poisson equations for the stream function is updated in a similar manner, which results in the AF form,

$$[I - h\bar{\delta}_\xi(\frac{A^{\xi\xi}}{J})^n\bar{\delta}_\xi][I - h\bar{\delta}_\varsigma(\frac{A^{\varsigma\varsigma}}{J})^n\bar{\delta}_\varsigma](\chi^{n+1} - \chi^n) = h\omega\left[\bar{\delta}_\xi(\frac{\chi^U}{J})^n + + \bar{\delta}_\varsigma(\frac{\chi^W}{J})^n + \frac{\omega}{J}\right] \tag{B.21}$$

where

$$\begin{aligned} \chi^U_{j+\frac{1}{2}} &= A^{\xi\xi}_{j+\frac{1}{2}}\Delta_\xi\chi_j + \frac{1}{2}\left(A^{\xi\varsigma}_{j+1}\delta_\varsigma\chi_{j+1} + A^{\xi\varsigma}_j\delta_\varsigma\chi_j\right) \\ \chi^W_{l+\frac{1}{2}} &= A^{\varsigma\varsigma}_{l+\frac{1}{2}}\Delta_\varsigma\chi_l + \frac{1}{2}\left(A^{\eta\varsigma}_{l+1}\delta_\eta\chi_{l+1} + A^{\eta\varsigma}_l\delta_\eta\chi_l\right) \end{aligned} \tag{B.22}$$

The scheme given by equation (B.21) is implemented by the same two-step ADI algorithm given by equation (B.19).

The differencing used with the vorticity transport equation is illustrated by considering equation (B.15):

$$(U\omega_\xi + W\omega_\varsigma) = \frac{J}{Re}\left[\left(\frac{A^{\xi\xi}\omega_\xi + A^{\xi\varsigma}\omega_\varsigma}{J}\right)_\xi + \left(\frac{A^{\xi\varsigma}\omega_\xi + A^{\varsigma\varsigma}\omega_\varsigma}{J}\right)_\varsigma\right] \tag{B.23}$$

Assuming U is generally larger than W, three-point, second-order-accurate central differencing is used in ζ, and three-point, second-order-accurate upwind differencing is used in ξ. Upwind differencing of Us_ξ is automatically achieved using

$$U\omega_\xi = U^+\delta_\xi^b\omega + U^-\delta_\xi^f\omega \tag{B.24}$$

where

$$U^+ = \frac{U+|U|}{2} \quad \text{and} \quad U^- = \frac{U-|U|}{2} \tag{B.25}$$

The convection equation is then solved using the AF relaxation algorithm

$$\begin{aligned}\left[I + hU^+\delta_\xi^b + hW\delta_\zeta - h\frac{J}{Re}\bar{\delta}_\zeta\left(\frac{A^{\zeta\zeta}}{J}\right)^n\bar{\delta}_\zeta\right]\left(I + hU^-\delta_\xi^f\right)\left(\omega^{n+1}-\omega^n\right)\\ = -h\left\{U^+\delta_\xi^b\omega^n + U^-\delta_\xi^f\omega^n + W\delta_\zeta\omega^n - \frac{J}{Re}\left[\bar{\delta}_\xi(\omega^U)^n + \bar{\delta}_\zeta(\omega^W)^n\right]\right\}\end{aligned} \tag{B.26}$$

where h is another relaxation parameter ($h > 0$) and ω^U and ω^W are defined as

$$\begin{aligned}\omega^U_{j+\frac{1}{2}} &= A^{\xi\xi}_{j+\frac{1}{2}}\Delta_\xi\omega_j + \frac{1}{2}\left(A^{\xi\zeta}_{j+1}\delta_\zeta\omega_{j+1} + A^{\xi\zeta}_j\delta_\zeta\omega_j\right)\\ \omega^W_{l+\frac{1}{2}} &= A^{\zeta\zeta}_{l+\frac{1}{2}}\Delta_\zeta\omega_l + \frac{1}{2}\left(A^{\eta\zeta}_{l+1}\delta_\eta\omega_{l+1} + A^{\eta\zeta}_l\delta_\eta\omega_l\right)\end{aligned} \tag{B.27}$$

Because central differencing is used in the ζ-direction, numerical dissipation is added to the differencing scheme as

$$\begin{aligned}\left[I + hU^+\delta_\xi^b + hW\delta_\zeta - h\frac{J}{Re}\bar{\delta}_\zeta\left(\frac{A^{\zeta\zeta}}{J}\right)^n\bar{\delta}_\zeta - 3h|W|\Delta\nabla|_\zeta\right]\left(I + hU^-\delta_\xi^f\right)\left(\omega^{n+1}-\omega^n\right)\\ = -h\left\{U^+\delta_\xi^b\omega^n + U^-\delta_\xi^f\omega^n + W\delta_\zeta\omega^n - \frac{J}{Re}\left[\bar{\delta}_\xi(\omega^U)^n + \bar{\delta}_\zeta(\omega^W)^n\right] + |W|(\Delta\nabla)^2|_\zeta\right\}\end{aligned} \tag{B.28}$$

At each ξ-plane, the algorithm requires a series of simple tridiagonal inversions in ζ.

Tangency or no-flow-through is imposed on a boundary surface by setting the appropriate contravariant velocity component to zero. On a ζ = constant plane, W is set to zero. Tangency is enforced through implicit boundary conditions on ϕ,

which are obtained by solving the continuity equation at the half-cells neighboring a solid boundary. The center of such a cell is located at $(j, l+\frac{1}{4})$. The finite-difference form of equation (B.13) can be written as

$$\left[\frac{(\frac{U}{J})_{j+\frac{1}{2},l+\frac{1}{4}} - (\frac{U}{J})_{j-\frac{1}{2},l+\frac{1}{4}}}{\Delta\xi}\right] + \left[\frac{(\frac{W}{J})_{j,l+\frac{1}{2}} - \cancel{(\frac{W}{J})^{0}_{j,l}}}{\Delta\zeta/2}\right] = 0 \qquad \text{(B.29)}$$

Evaluating variables at $l+\frac{1}{4}$ by weighted averaging between l and $l+1$ as, for example,

$$U_{j+\frac{1}{2},l+\frac{1}{4}} = \frac{3}{4}U_{j+\frac{1}{2},l} + \frac{1}{4}U_{j+\frac{1}{2},l+1} = (I + \frac{1}{4}\Delta_\zeta)U_{j+\frac{1}{2},l} \qquad \text{(B.30)}$$

where

$$U_{j+\frac{1}{2},l} = A^{\xi\xi}_{j+\frac{1}{2}}\Delta_\xi\phi_j + \frac{1}{2}(A^{\xi\zeta}_{j+1}\Delta_\zeta\phi_{j+1} + A^{\xi\zeta}_{j}\Delta_\zeta\phi_j) \qquad \text{(B.31)}$$

Equation (B.28) can be written as

$$(I + \frac{1}{4}\Delta_\zeta)(\frac{U}{J})_{j+\frac{1}{2}} - (I + \frac{1}{4}\Delta_\zeta)(\frac{U}{J})_{j-\frac{1}{2}} + 2(\frac{W}{J})_{l+\frac{1}{2}} = 0 \qquad \text{(B.32)}$$

To facilitate the application of approximate factorization, the cross-derivative terms are lagged in time in the usual way to obtain the relaxation algorithm

$$\begin{aligned}[I - h\bar{\delta}_\xi(\frac{A^{\xi\xi}}{J})^n\bar{\delta}_\xi][I - 2h(\frac{A^{\xi\zeta}}{J})^n_{l+\frac{1}{2}}\Delta_\zeta](\phi^{n+1} - \phi^n) \\ = h\omega\{\bar{\delta}_\xi(\frac{U}{J})^n + 2(\frac{W}{J})^n_{l+\frac{1}{2}} + \frac{1}{4}\Delta_\zeta[\bar{\delta}_\xi(\frac{U}{J})^n]\}\end{aligned} \qquad \text{(B.33)}$$

Equation (B.32) is of the same form as equation (B.16) and hence tangency can be enforced implicitly in the ADI algorithm given by equation (B.19) with the tridiagonal and right-hand-side terms modified appropriately.

B. Boundary Layer Equations

1. Governing equations

In two dimensions, the unsteady, incompressible laminar boundary-layer equations are

$$u_{\bar{x}} + \bar{w}_{\bar{z}} = 0 \tag{B.34}$$

$$\rho\bar{u}_t + \rho(\bar{u}\bar{u}_{\bar{x}} + \bar{w}\bar{u}_{\bar{z}}) = -\bar{p}_{\bar{x}} + \bar{u}_{\bar{z}\bar{z}} \tag{B.35}$$

In these equations, the normal coordinate $\bar{z}$ and the normal component of velocity $\bar{w}$ are scaled by the square root of the free stream Reynolds number $Re^{\frac{1}{2}}$.

Using a general coordinate transformation defined by

$$\xi = \xi(\bar{x}); \quad \zeta = \zeta(\bar{x}, \bar{z}) \tag{B.36}$$

the above equations are transformed as

$$\bar{u}_\xi \xi_{\bar{x}} + \bar{u}_\zeta \zeta_{\bar{x}} + \bar{w}_\zeta \zeta_{\bar{z}} = 0 \tag{B.37}$$

$$\rho\bar{u}_t + \rho(\bar{U}\bar{u}_\xi + \bar{W}\bar{u}_\zeta) = -\bar{p}_\xi \xi_{\bar{x}} + (\bar{u}_\zeta \zeta_{\bar{z}})_\zeta \zeta_{\bar{z}} \tag{B.38}$$

where U and $\bar{W}$ are unscaled contravariant velocities defined as

$$\begin{aligned} \bar{U} &= \xi_t + \xi_{\bar{x}}\bar{u} \\ \bar{W} &= \zeta_t + \zeta_{\bar{x}}\bar{u} + \zeta_{\bar{z}}\bar{w} \end{aligned} \tag{B.39}$$

2. Numerical algorithms

The boundary-layer equations are solved with a relaxation algorithm which can be run in either a time-accurate or an iterative mode. The relaxation algorithm was designed by Van Dalsem and Steger (1985) to yield convergence to a steady-state algorithm quickly. The continuity and momentum equations are solved in an

uncoupled manner at each time step. The momentum equation is used to update the streamwise velocity $\bar{u}$ using upwind differencing in the streamwise direction and central differencing in the normal direction. The continuity equation is used to update the normal velocity $\bar{w}$ using second-order-accurate central differencing in the ξ-direction. The trapezoidal rule is used to integrate the continuity equation in the ς-direction to obtain $\bar{w}$.

The algorithm was designed for three-dimensional unsteady compressible flows by Van Dalsem and Steger (1985). A simplified version for two-dimensional incompressible flows which was used in this study is presented below.

1) Update $\bar{u}$ at the new time step from the $\bar{x}$-momentum equation

$$\rho\nabla_t\bar{u}^{n+1} + \rho(\bar{U}^+\delta_\xi^b\bar{u}^{n+1} + \bar{U}^-\delta_\xi^f\bar{u}^n + \bar{W}\delta_\varsigma\bar{u}^{n+1}) = -\xi_{\bar{x}}\delta_\xi\bar{p} + \varsigma_{\bar{z}}\bar{\delta}_\varsigma(\varsigma_{\bar{z}}\bar{\delta}_\varsigma\bar{u}^{n+1}) \quad \text{(B.40)}$$

2) Integrate the continuity equation for $\bar{w}$ using updated values of $\bar{u}$

$$\nabla_\varsigma\bar{w}^{n+1} = -\frac{1+E_\varsigma^{-1}}{2}(\xi_{\bar{x}}\delta_\xi\bar{u} + \varsigma_{\bar{x}}\delta_\varsigma\bar{u})^{n+1} \quad \text{(B.41)}$$

3) Repeat steps (1)-(2) till convergence is obtained to the steady-state solution.